Technische Universität München
Physik-Department
E19a

Modellierung komplexer Phänomene in offenen, elektrochemischen Systemen

Mario Munir Salman

Vollständiger Abdruck der von der Fakultät für Physik der Technischen Universität München zur Erlangung des akademischen Grades eines Doktors der Naturwissenschaften genehmigten Dissertation.

Vorsitzende(r): Prof. Dr. Aliaksandr S. Bandarenka

Prüfende der Dissertation:

1. Prof. Dr. habil. Katharina Krischer
2. Prof. Dr. Michael Eikerling

Die Dissertation wurde am 8. Mai 2020 bei der Technischen Universität München eingereicht und durch die Fakultät für Physik am 22. Oktober 2020 angenommen.

Contents

I Introduction 1

II Modeling of Si Electro-Oxidation in HF Solution 7

II.1 Motivation 9

II.2 Review 13
II.2.1 Activity diagram 13
II.2.2 Current-voltage characteristics 19
II.2.3 Ionic transport 19
II.2.4 Photoluminescence and trap hopping 20
II.2.5 Oscillation shapes and patterns 20
II.2.6 At very high voltages 20
II.2.7 Electrochemical impedance 21
II.2.8 Limited illumination of n-type silicon 21
II.2.9 Model by Cattarin et al. 22
II.2.10 Model by Chazalviel et al. 25
II.2.11 Model by Hasegawa et al. 25
II.2.12 Model by Krischer et al. 26
II.2.13 Summary and Conclusion 27

II.3 Model definition 29
II.3.1 Concept 29
II.3.2 Kinetic description 30
II.3.3 Boundary conditions 33
II.3.4 Total electric current 34
II.3.5 Implementation 35
II.3.6 Discussion 35

II.4 Simulation results . . . 39
II.4.1 Current-voltage characteristics . . . 39
II.4.2 Oxide layer properties . . . 39
II.4.3 Dissolution valence . . . 41
II.4.4 Impedance spectra . . . 43
II.4.5 Origin of the negative differential resistance . . . 48

II.5 Summary and outlook . . . 51

III Modeling of CO Electrooxidation on Globally Coupled Pt Microelectrodes . . . 53

III.1 Motivation . . . 55

III.2 Review: Phase transitions . . . 61
III.2.1 Homogeneous . . . 61
III.2.2 Inhomogeneous . . . 62

III.3 General, linear analysis . . . 67
III.3.1 Individual components . . . 67
III.3.2 Ensemble . . . 71
III.3.3 Comparison with first-order phase-transitions . . . 72

III.4 Model . . . 83
III.4.1 Derivation of the model . . . 83
III.4.2 Model . . . 84

III.5 Non-linear cluster dynamics of the model . . . 91
III.5.1 Cluster subspaces . . . 92
III.5.2 Fully synchronized dynamics . . . 92
III.5.3 Two-cluster dynamics and bifurcations . . . 93
III.5.4 Three-cluster dynamics and bifurcations . . . 98

III.6 Summary and Outlook . . . 105

IV Conclusion . . . 107

Bibliography . . . 111

Acknowledgements

I would like to thank Prof. Dr. Katharina Krischer for exciting my interest in the field of non-equilibrium thermodynamics and for offering me the opportunity to do research in her group. Also, I thank her for believing in my abilities and giving me freedom to follow own ideas. I would like to offer my very special thanks to Maximilian Patzauer for conducting the measurements that support the model for silicon electrodissolution, for many discussions on non-linear dynamics and silicon electrochemistry, and for writing advice and critical reading. I am very grateful for the impedance measurements and analysis by Dominique Koster, and for the associated method of multifrequency analysis by Prof. Fabio La Mantia. Furthermore, I am particularly grateful for the assistance given by Dr. Felix Kemeth regarding python and the continuation of limit cycles with AUTO, for our discussions concerning non-linear dynamics, and for critical reading. The advice given by Dr. Christian Bick on cluster subspaces was greatly appreciated. I would also like to thank Sindre W. Haugland for providing me with a sense of style regarding scientific writing, for discussions about non-linear dynamics, and for critical reading. I greatly appreciated the extended discussions with Konrad Schönleber about silicon in hydrofluoric acid, thermodynamics, and energy science. Very special thanks go to Dr. Daniel Heger for his diligent IT-administrative care, which made it a lot easier for me as a successor. Thanks to Anton Tosolini for sharing with me his measured data for a conference poster. I am thankful to PD. Dr. Werner Schindler for his answers to my questions about semiconductor electrochemistry. My special thanks are extended to the entire group for their constructive feedback especially during group seminars, and for the enjoyable time. I would like to express my very deep gratitude to Leonie Schmid for her reliable support, especially during the final weeks before the submission. Finally, I wish to thank my parents for motivating me to pursue this path.

Part I

Introduction

The fascination of complex phenomena in open systems roots in a very old philosophical, almost spiritual question. What is the fundamental difference between a living thing, like a cat, and a non-living thing, like a stone? They both consist of many particles that should follow the same laws of nature in principle. Yet, there seems to be a distinction between them. Unlike a stone, a cat seems to move by the power of a will that is not obviously captured by the "simple" laws of physics, making it much more complex in a way. For a long time, this paradox has fascinated scientists and philosophers alike, and to a certain degree it still does so to this day. Until the first half of the last century, there was a rather clearcut distinction between living and non-living matter, even among some recognized scientists. Supporters of this view attributed living things to the existence of a life-giving substance called élan vital. As often, a pure description had turned into a fake explanation.

One well known person who did not adopt this view was Alan M. Turing. He rejected the idea of an ominous will or a vital force underlying the behavior and the emergence of living things. Instead, he believed that complex phenomena like thoughts and morphogenesis could emerge from very simple rules. In order to promote this view, he considered a toy model that basically describes the concentrations of only two chemicals in a petri dish. In this model, the concentrations change over time according to very simple chemical-reaction rules and diffusion [1]. It turns out that this is sufficient for complex labyrinth patterns to emerge in the petri dish and it has later been recognized that the very same mechanism is responsible for certain characteristic pigment patterns in fish skin. These Turing patterns became one of the prototypical examples for a self-organized complex phenomenon and they have opened a whole field of chemical complexity. Turing patterns might not explain life, but they certainly prove that something like a labyrinth pattern can paint itself without the intention of a hidden painter behind.

The question of what constitutes a physical system in which such complex phenomena can arise, and what a useful definition of a complex phenomenon is, has been addressed by Ilya Prigogine. Until the middle of the 20th century, many-particle systems were mostly considered at their thermodynamic equilibrium, so one could apply the powerful theory of thermodynamics. They did not bother that for the cat this would mean putting it in a box and waiting for convergence, because thermodynamics had been developed to build engines, not to study cats. However, the mindset of thermodynamic equilibria was somewhat over-established, such that when Boris P. Belousov found a chemical mixture that periodically changed its color and chemical concentrations, he was not believed at first. His findings were thought to contradict the second law of thermodynamics, by which the entropy, which is a function of the concentrations, cannot decrease, let alone oscillate periodically. Because of the second law, concentrations in a mixture had mostly been thought of as being at an equilibrium of maximum entropy. Anyhow, though indeed every closed many-particle system will at some point end up in an equilibrium, Prigogine

promoted the awareness that almost everything of interest actually happens before that equilibrium is reached. In the case of Belousov's paradoxical oscillations, later known as the Belousov-Zhabotinski reaction, the key is that some chemical species are slowly being depleted as the oscillation proceeds. As soon as there this not enough fuel left for the oscillation, it stops and the system eventually settles to a thermodynamic equilibrium. However, if you keep supplying the fuel in an open flow reactor, the oscillation can go on indefinitely long. Considering such open thermodynamic systems, which are artificially kept away from their equilibrium, Prigonine advanced the theoretical framework of non-equilibrium thermodynamics. He showed that in first-order proximity of a thermodynamic equilibrium, so called dissipative structures can form, which happen to minimize the entropy production by the open system, e.g. stationary Turing patterns and vortexes. The emergence of dissipative structures indeed decreases the entropy inside the open system, but this is made up for by an increase of the entropy of the surroundings. Even farther away from equilibrium, an open system can in principle be arbitrarily complex. This recognition restored the consistence between thermodynamics and all the phenomena that we see everywhere around us, and it connected the theory of thermodynamics with field of non-linear dynamics in the new field of far-from-equilibrium thermodynamics. Today, this is one of the main branches of physics and it studies the non-linear behavior of thermodynamic systems far from equilibrium. In this thesis we mainly consider two technologically relevant examples for open systems that are operated far from equilibrium: Silicon in hydrofluoric acid under positive bias and CO electrooxidation on platinum.

Due to the work of John Bardeen and William Shockley on transistors, Si has become the material that drove the third industrial revolution. When exposed to air, Si forms a patina of SiO_2 that is electrically insulating. To remove the SiO_2 layer from a waver of Si, it can be immersed in HF acid. Moreover, HF acid leaves the Si surface covered with Si-H bonds that passivate it against further oxidation. However, if the oxidation is driven by an anodic bias, Si can be etched away by HF acid. In the beginning, investigations of anodic Si in HF had been solely motivated by technological motives, but it turned out that this system is worth studying for another reason that lies in the context of far-from-equilibrium thermodynamics, i.e. the very unique dynamical behavior of the oxide layer at sufficiently anodic potential. Besides showing a variety of dynamical phenomena, anodic Si in HF is one of the few systems that exhibit a certain highly selforganized oscillatory state, in which one part of the Si electrode oscillates homogeneously while the rest is turbulent. This type of state has been coined "Chimera state", reflecting the unequal nature of the two domains. While there are other experimental systems in which such Chimera states occur, Si in HF is the only one so far in which there is no externally imposed coupling between the oscillation sites. The experimental investigation of Si in HF has sparked further theoretical understanding of how Chimera states can arise.

Thus, Si in HF is relevant not only from a material science and an electrochemisty point of view, but also for the understanding of general principles of non-linear dynamics. A main issue with this system is the lack of understanding of the physical processes behind the dynamics. This thesis contributes to this problem by proposing a physicochemical model in Part.II, which is reworked and highly extended version of an article that we published in The European Physics Journal [2].

Other instances of selforganization that have recently gained considerable attention were found in globally coupled systems of bistable components. Such systems seem to show certain characteristic behaviors, like the sequential switching of individual bistable components from one stable state to the other as a system-specific global quantity is ramped. One example for this are chargeable nanoparticles in Li-ion batteries that have a non-monotonous charge-voltage characteristics. Such nanoparticles are bistable in a certain voltage range, being either charged or discharged. As the total charge is increased over time by applying a constant current to the battery, the nanoparticles are charged one after the other or in small groups, as opposed to being charged simultaneously. Each time a group of nanoparticles is charged, the voltage increases and decreases. Another example for this sequential switching are Pt microelectrodes in a CO containing solution, which are technically relevant for catalysis in hydrogen fuels-cells if the H_2 came from steam reforming. The individual microelectrodes have a non-monotonous current-voltage characteristics. At very low voltages, the microelectrodes are covered with CO and conduct a negligible current. At very large voltages, they are CO depleted and contribute a large current. However, at intermediate voltages, they are bistable, being either in a low-current or a hight-current state. If one ramps the total current through several parallelly connected microelectrodes, they switch on individually, analogously to the Li nanoparticles when their total charge is ramped. The two systems follow the same dynamic principle. However, there is a behavior of the Pt microelectrodes that is not seen with the Li nanoparticles: A sustained periodic oscillations, without a parameter ramp. This phenomenon has been observed in experiments and reproduced in models, but it has not been clear why this happens and more importantly why it does not happen in other systems. This question is answered in Part III. Moreover, Part III addresses the individual switching and another so far undocumented kind of sustained collective oscillation, which has interesting stability properties, by which it could potentially occur in an actual fuel cell with arbitrarily many Pt nanoparticles.

Part II

Modeling of Si Electro-Oxidation in HF Solution

Chapter II.1

Motivation

Silicon is still most common working material in semiconductor devices and its physical properties are, thus, of supreme interest. It can be cleaned with HF acid and applying an anodic bias to a silicon electrode in HF acid can even polish or etch it, depending on the applied electric potential. Furthermore, this electrochemical setup is very interesting from a non-linear dynamics point of view: When a silicon electrode is electrochemically dissolved in HF acid, it is covered by a layer of oxidized silicon which can change its thickness in peculiar spatiotemporal patterns [3–10]. (For a comprehensive overview of the work until 2003 see Chapter 5 in [11].) These spatiotemporal patterns make silicon in hydrofluoric solution one of the most relevant electrochemical systems for basic studies of nonlinear dynamics. The most prominent example is the chimera state, in which one part of the electrode surface oscillates homogeneously, while the rest is turbulent [12–15]. An example for this is shown in Fig. II.1.1, which shows a spatially resolved ellipsometric-intensity measurement of a silicon electrode in a HF containing solution. The ellipsometric intensity is a qualitative measure of the oxide-layer thickness. On the left, we see a snapshot of the electrode surface. The area close to the borders of the frame does not belong to the electrode itself. The darker patch close to the center is the homogeneous domain of the Chimera state, the rest appears to be inhomogeneous. On the right, we see a time series of a one dimensional cut of the electrode (dashed orange line). The homogeneous domain oscillates perfectly periodically while the rest of the electrode exhibits spatiotemporal chaos. Although it is possible to find some attempts of modeling [16–18], not even the simplest, periodic, spatially homogeneous oscillations have so far been consistently and convincingly ascribed to a concrete physical mechanism.

When trying to model the system one has to consider the following processes. Applying a postive voltage to a silicon electrode in an aqueous electrolyte results in the formation of silicon dioxide [11]. As the oxidation reaction proceeds, the resulting layer of oxide eventually passivates the electrode, inhibiting further reaction. However, if the solution contains HF or HF_2^- species, the oxide layer is etched away [19, 20]. The oxide layer thickness may, thus, attain a steady state at which the rates by which the oxide layer grows into the silicon electrode and is

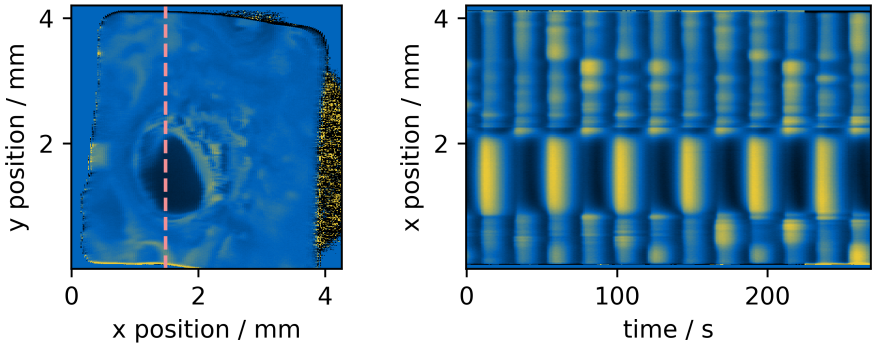

Figure II.1.1: Spatially resolved ellipsometric intensity in arbitrary units, measured on a weakly illuminated ⟨111⟩ n-silicon electrode of 5 to 25 Ω cm in a solution of 0.05 M NH_4F and 0.025 M H_2SO_4 (pH 2.3). The measurement has been conducted by Maximilian Patzauer.

dissolved by the fluoride containing solution balance exactly. The current-voltage characteristics of this equilibrium are very similar for a wide range of parameters as measured by Chazalviel et al. [21]. They measured cyclic voltammograms that were so slow that they were quasi-stationary. A typical curve is exemplarily depicted in the cyclic voltammogram in Figure II.1.2, which was measured in the course of this doctoral project. The curve has two current peaks. The first peak is very narrow and, in this example, it lies close to 0.3 V vs. SHE. It marks the transition from pore formation to electropolishing. The second peak is rather wide and its maximum lies close to 1.8 V vs. SHE. At electrode potentials higher than the maximum of the second peak, the driving force for the oxidation is so strong that an oxide layer of some nm is present, while at electrode potentials between the two peaks there is no layer. Thus, the second peak maximum marks the potential above which the steady flow equilibrium has a layer. [22, 23]. At even higher voltages, namely in the current plateau above 3 V vs. SHE in Fig. II.1.2, this equilibrium can become dynamically unstable at certain experimental parameter values, which then leads to spatiotemporal variations of the oxide-layer thickness. This plateau is referred to as the resonant regime due to the strange impedance that has been measured there [24].

Since complex dynamics tend to bifurcate from simple dynamics, the first step towards a comprehensive understanding must be to find out which physical processes lead to the equilibrium properties, for example the stationary current-voltage characteristics and the electrochemical impedance. So far there is a model for the current-voltage characteristics in the electropolishing regime at voltages below second the current peak in Figure II.1.2 [25]. There is also a more abstract model

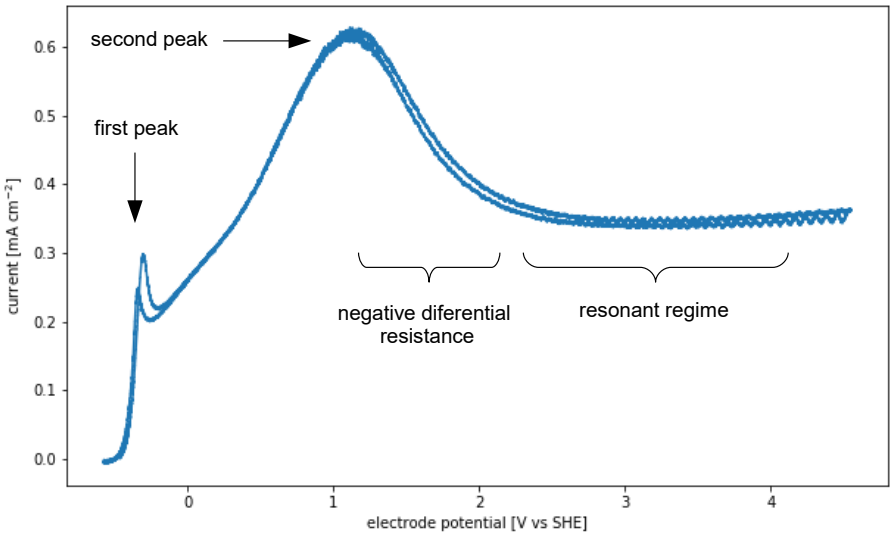

Figure II.1.2: 2 mV/s cyclic voltammogram of a ⟨111⟩ p-silicon electrode of 5 to 25 Ω cm in a solution of 0.05 M NH_4F and 0.025 M H_2SO_4 (pH 2.3), measured with help from Konrad Schönleber.

for the electrochemical impedance at the plateau at higher voltages in Figure II.1.2, which is known to show strange resonance [18]. In this part of the thesis, a physical model is presented, which explains both the current-voltage characteristics and the impedance spectrum in the regime of negative differential resistance. Moreover, the model reproduces the dependence of the oxide layer thickness and the dissolution valency on the applied potential.

The central idea of the model is that the oxide is etched with a rate that depends on its composition. This assumption was motivated by measurements of the dissolution valency and the current-voltage characteristics [7, 22, 23], and by the fact that the etching is likely to occur purely chemically, i.e. without charge transfer [22, 26, 27]. The latter means that the applied potential should not influence the etch rate of the oxide layer. However, the rates of the purely chemical etching and the voltage-dependent oxidation have to be the same at the steady state. Hence, there has to be an indirect dependence of the etch rate on the applied voltage. The model explains this indirect dependence by the change in oxide composition as the voltage is varied. This change could arise due to the accumulation/depletion of ions or defects moving through the oxide layer. The core of the silicon part of this thesis is a physical model that incorporates this idea.

Chapter II.2

Review

This section reviews selected properties that have been measured for silicon electrodes in fluoride-containing solutions. They form the basis of the model developed in Chap. II.3. For more details on silicon electrodissolution, see the text book contributed by Xiaoge Gregory Zhang in 2001, reviewing the properties of silicon and its oxides [11]. There is also a book from 2002 by Lehmann about the electrochemical dissolution of silicon [28].

II.2.1 Activity diagram

For any combination of pH and electrode potential, the equilibrium conditions dictate the activities of the chemical species in the electrolyte. These equilibrium activities can be visualized quantitatively in a diagram like the one in Figure II.2.1, where the equilibrium activities of several species are shown as gray-scale maps, with pH and electrode potential plotted as the horizontal and the vertical axis, respectively. Here, square brackets indicate activities. Such diagrams can be calculated given a set of reactions, like II.2.5 - II.2.11, and given the corresponding $\Delta G_\mathrm{f}^0(T)$ for each species, which is the standard Gibbs free energy of formation. The latter tells us by how much the Gibbs free energy $G(T, p, n_1, n_2, \ldots, n_N, \Phi_1, \Phi_2, \ldots, \Phi_N)$ changes if one mole of the respective species is added at 1 bar, temperature T, and activity $a_k = 1$. Let n_k be the number of moles of the k-th species, z_k the charge number of the k-th species, Φ_k the electrostatic potential in the domain of the k-th species, R the universal gas constant, and F the Faraday constant. For an arbitrary activity a_k of the k-th species, the change in $G(\ldots)$ per mole is given by the elctrochemical potential $\tilde{\mu}_k(T, p, n_1, n_2, \ldots, n_N, \Phi_1, \Phi_2, \ldots, \Phi_N)$:

$$\tilde{\mu}_k(\ldots) \equiv \frac{\partial G(T, p, n_1, n_2, \ldots, n_N, \Phi_1, \Phi_2, \ldots, \Phi_N)}{\partial n_k} \tag{II.2.1}$$

$$\overset{\text{if } p=1\text{bar}}{=} RT \cdot \ln(a_k) + z_k F \Phi_k + \left(\Delta G_\mathrm{f}^0\right)_k (T) \tag{II.2.2}$$

$$\overset{\text{if ideal mixture}}{=} RT \cdot \ln\left(\frac{n_k}{\sum_i n_i}\right) + z_k F \Phi_k + \left(\Delta G_\mathrm{f}^0\right)_k (T) \tag{II.2.3}$$

The sum in Eq. (II.2.3) goes over all species that have the same phase as the k-th species. At equilibrium, the Gibbs free energy is minimal, and thus, the electrochemical potentials obey Eq. (II.2.4), where $\nu_{ij} \in \mathbb{Z}$ is the stoichiometric coefficient of the j-th species in the i-th reaction.

$$\forall i : \sum_j \nu_{ij} \tilde{\mu}_j(T, p, n_1, n_2, \ldots, n_N, \Phi_1, \Phi_2, \ldots, \Phi_N) = 0 \tag{II.2.4}$$

Setting the activity fixed for some of the species, like H_2O or an electrode material, we obtain the remaining activities with Eq. (II.2.4). In doing this, we follow Osseo-Asare et al. very closely, who have plotted Pourbaix diagrams for this system [20]. Notice that the chosen reactions do not affect the equilibrium activities as long as there is a pathway to every species and as long as stoichiometry is fulfilled, because the solution of the equilibrium equation (Eq. (II.2.4)) stays the same.

Even though we only consider equilibrium conditions, the activities that we obtain this way tell us if a given reaction is thermodynamically allowed at the Si-HF interface. Let us first consider a Si electrode in H_2O, without fluoride (Fig. II.2.1). The involved species and reactions are given in Eq. (II.2.5) - (II.2.7) and Eq. (II.2.11).

$$2H_2O + 2e^- \rightleftharpoons H_2 + 2OH^- \tag{II.2.5}$$
$$2H_2O \rightleftharpoons O_2 + 4H^+ + 4e^- \tag{II.2.6}$$
$$O_2 + Si + 2H_2O \rightleftharpoons Si(OH)_4 \tag{II.2.7}$$
$$HF + F^- \rightleftharpoons HF_2^- \tag{II.2.8}$$
$$HF \rightleftharpoons F^- + H^+ \tag{II.2.9}$$
$$SiO_2 + 6HF \rightleftharpoons SiF_6^{2-} + 2H^+ + 2H_2O \tag{II.2.10}$$
$$Si + O_2 \rightleftharpoons SiO_2 \tag{II.2.11}$$

For this setup, we see that H_2 and O_2 evolution occurs at the usual parameters, so H_2O is thermodynamically stable only within a certain potential range that depends on the pH value. Analogously, Si is thermodynamically stable only for rather cathodic electrode potentials. At more anodic potentials, the Si electrode is oxidized to SiO_2 (solid) or $Si(OH)_4$ (in solution). Both are possible products from a thermodynamic point of view. In practice, once a passivating layer of SiO_2 is formed on top of a Si electrode, the surface is blocked for further oxidation.

Let us now consider what happens if the solution contains a small amount of fluoride (Fig. II.2.2). The equilibrium activities of H_2, O_2, SiO_2, and $Si(OH)_4$ stay unchanged because the equilibrium condition stay the same for the reactions involving these species, given a certain pH. This means that $Si(OH)_4$ is still a possible product. For the chosen total amount of fluoride, the fluoride can be present as either F^-, HF_2^- or HF, depending of the pH value. The most important part here is the species SiF_6^{2-} (in solution), which is present in a wide range of parameters.

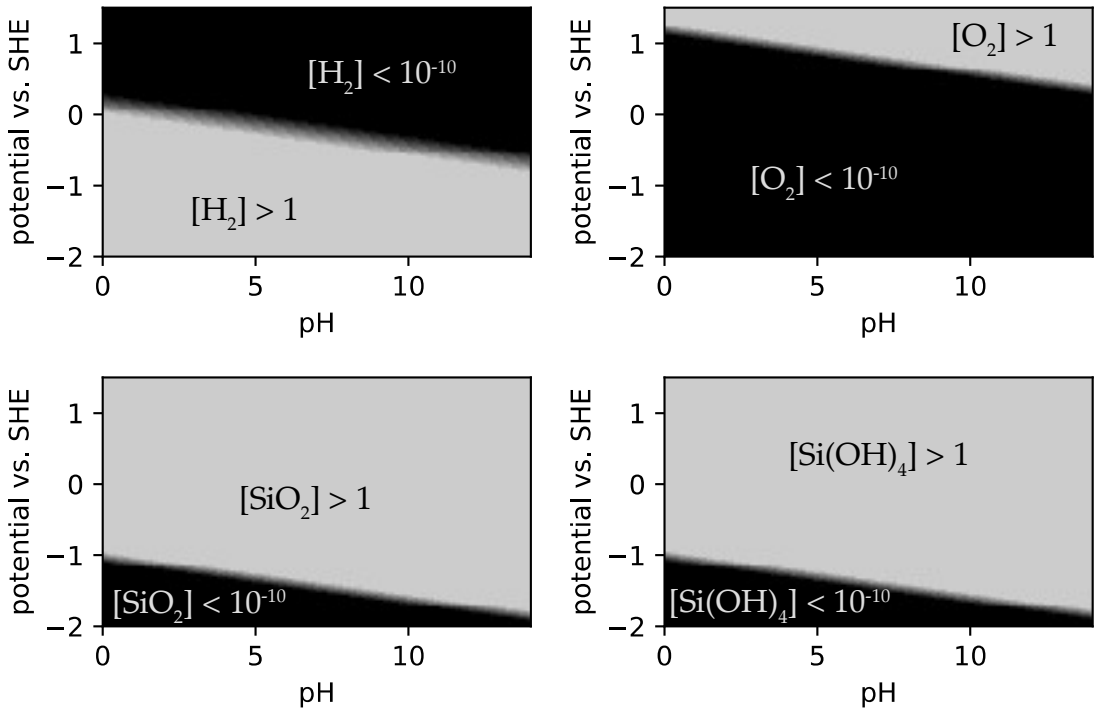

Figure II.2.1: Theoretical activities of some chemical species for Eq. (II.2.5) - (II.2.7) and (II.2.11), i.e. silicon in water without any fluoride. We assume the fixed activities $[H_2O] = [e^-] = [Si] = 1$. The necessary standard Gibbs free energies of formation are given in Tab. II.2.1. Every shade of gray corresponds to an order of magnitude.

Notice that the equilibrium activities of SiF_6^{2-} is greater than one even though we fix $[HF]+2[HF_2^-]+[F^-] = 0.02$. This only means that for these parameters there is a strong thermodynamic tendency to produce SiF_6^{2-}. It is just the same phenomenon that we see e.g. with H_2, even though we fix $[H_2O] = 1$. For these parameters, SiF_6^{2-} is thermodynamically favored over Si, and Si should therefore be dissolved. However, this plot does not tell us whether SiF_6^{2-} is also favored over SiO_2, which is very favorable too, as seen in Fig. II.2.2, and which therefore should form a layer on top of the Si.

In order to determine for which parameters the SiO_2 layer is actually capable of protecting the electrode, let us consider what would happen to a solid SiO_2 phase, i.e. with activity 1, in a fluoride containing solution (Fig. II.2.3). Looking at the equilibrium activity of SiF_6^{2-} Fig. II.2.3, we see that for the chosen total amount of fluoride there is a pH window in which SiF_6^{2-} is thermodynamically favorable over

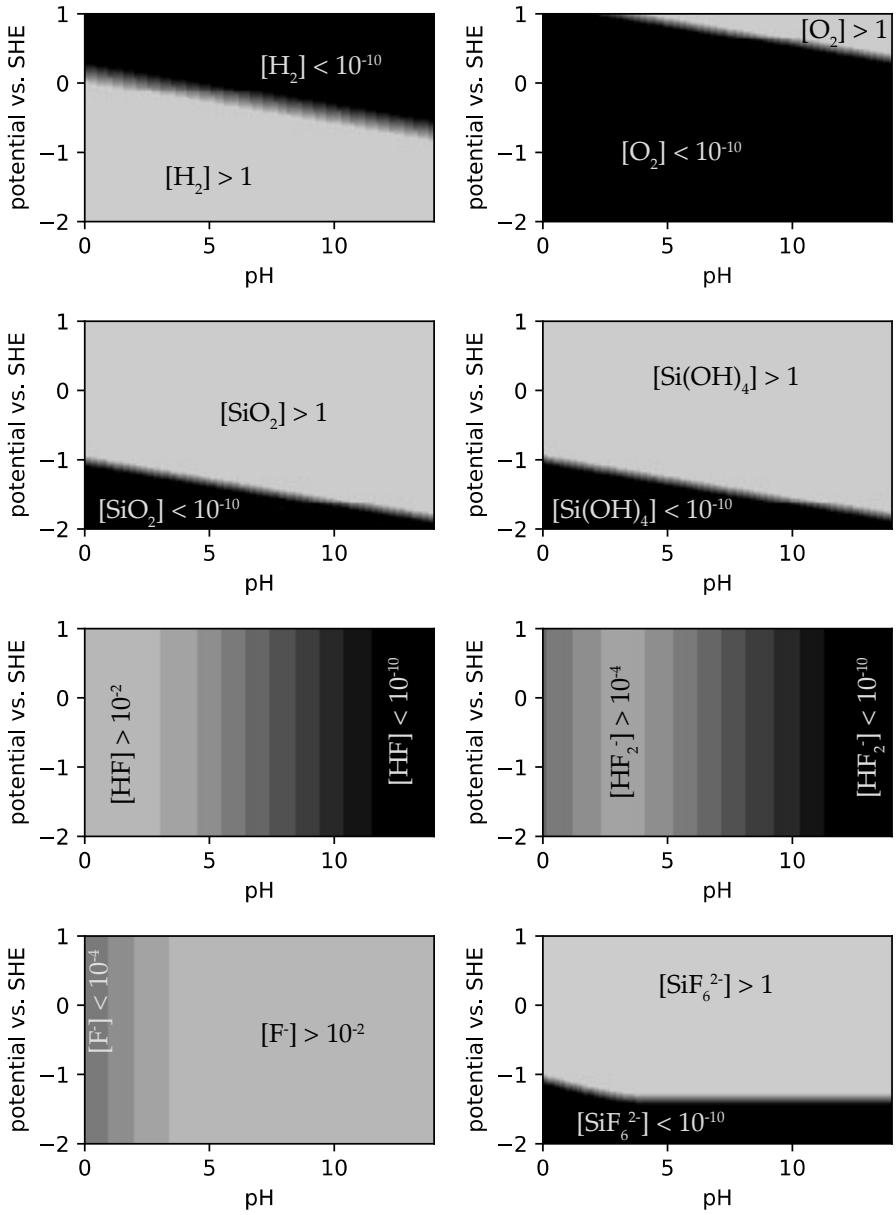

Figure II.2.2: Theoretical activities of some chemical species for Eq. (II.2.5) - (II.2.11), for Si in a F-containing solution. We assume the fixed activities $[H_2O] = [e^-] = [Si] = 1$, $[HF]+2[HF_2^-]+[F^-] = 0.02$. The necessary standard Gibbs free energies of formation are given in Tab. II.2.1. Every shade of gray corresponds to an order of magnitude.

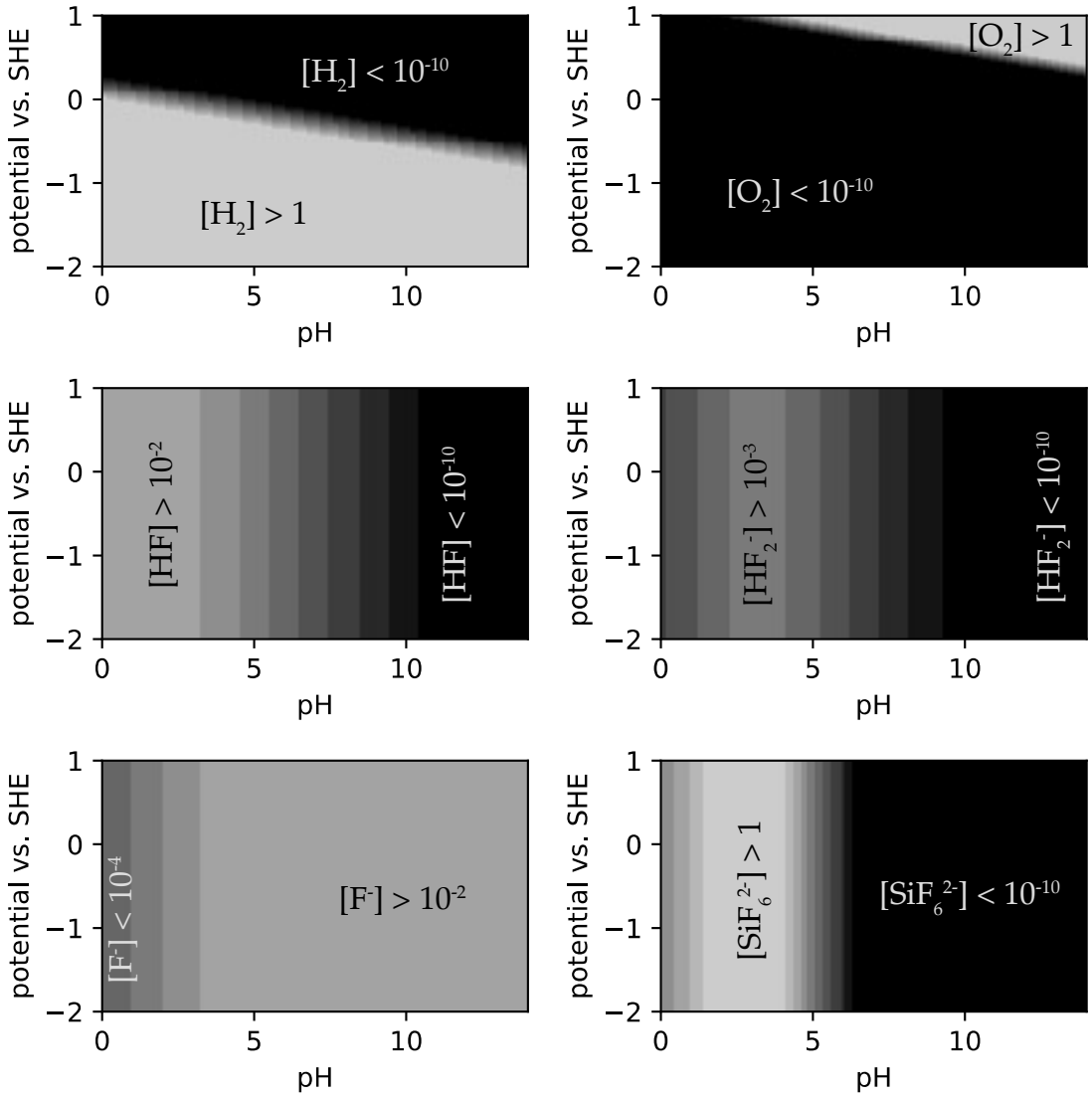

Figure II.2.3: Theoretical activities of some chemical species for Eq. (II.2.5),(II.2.6),(II.2.8),(II.2.9),(II.2.10), for SiO_2 in a F-containing solution. We assume the fixed activities $[H_2O] = [e^-] = [SiO_2] = 1$, $[HF]+2[HF_2^-]+[F^-] = 0.02$. The necessary standard Gibbs free energies of formation are given in Tab. II.2.1. Every shade of gray corresponds to an order of magnitude.

SiO_2. Thus, it is only within this pH window that a passivating SiO_2 layer could be dissolved. Notice that this window does not depend on the potential, so the dissolution does not involve a net charge transfer. All in all, this means that the Si electrode should be dissolved only within the intersection between the parameter regime in which SiO_2 can be produced from Si (Fig.II.2.2), and the parameter regime in which the produced SiO_2 can be dissolved as SiF_6^{2-} (Fig.II.2.3).

Notice that there is no parameter regime in which SiF_6^{2-} could be produced without SiO_2 too being much more favorable than Si. This could mean that the dissolution of Si always involves an electrochemical oxidation to SiO_2, followed by a purely chemical etching, i.e. SiO_2 reacts to SiF_6^{2-}. We incorporate this idea in the dynamic Si-dissolution model in Chap. II.3, by assuming that there is a thin layer of SiO_x present during the dissolution. In the model, SiO_x is considered instead of SiO_2, because we expect sub-stoichiometric oxide to play an important role for the shape of the current voltage characteristics, and because measurements of a dissolution valence smaller than 4, i.e. 4 charge carriers per Si atom, indicate sub-stoichiometric oxide [22]. Unlike for SiO_2, the data on sub-stoichiometric oxide is sparser, so it has not been considered in this section.

	ΔG_f^0(298 K)	ref.
H_2(g)	0	by def.
O_2(g)	0	by def.
H^+(aq)	0	by def. (SHE)
OH^-(aq)	157.2 kJ	[29]
H_2O(l)	-237.1 kJ	[29]
HF(g)	-275.4 kJ	[29]
HF(aq)	-296.82 kJ	[20]
HF_2^-(aq)	-579.08 kJ	[20]
F^-(aq)	-278.79 kJ	[20]
Si(s)	0	by def.
SiO_2(s)	-850.70 kJ	[20]
$Si(OH)_4$(aq)	-1316.6 kJ	[20]
SiF_6^{2-}(aq)	-2199.4 kJ	[20]
e^-	0	by def. (SHE)

Table II.2.1: Standard Gibbs free energy of formation ΔG_f^0 at 298 K for compounds in gaseous (g), liquid (l), or solid (s) phase, or dissolved in water (aq)

II.2.2 Current-voltage characteristics

A steady state current-voltage characteristics with two current peaks like the one in Fig. II.1.2 was measured by Eddowes in 1990 [22]. He also investigated how the hight of the two peaks changes with the fluoride concentration. The peak at lower voltage marks the voltage below which pores are formed, according to Lehmann [30]. He measured the height of the first peak, also known as the critical current, for various HF concentrations and temperatures. The resulting data points clearly followed Eq. II.2.12. It contains the weight fraction of HF c, the temperature T, the Boltzmann-constant k, and three fit parameters: The activation energy $E_a = 345\,\mathrm{meV}$, the exponent $\nu = 1.5$, and the coefficient $C = 3300\,\mathrm{A\,cm^{-2}} \cdot 100^{\nu}$.

$$J_{PS} = C c^{\nu} \exp\left(\frac{-E_a}{kT}\right) \tag{II.2.12}$$

However, the second peak, the one at higher voltages, is even more interesting in our context because it roughly marks the voltage above which we find the peculiar, resonant voltage regime. Interestingly, the latter peak pertains its width at arbitrarily slow voltage scan-rates and its shape cannot be explained by traditional models for surface adsorption or layer transport. A systematic study of the current-voltage curve including the second peak has been contributed by Chazalviel et al. They measured the current-voltage characteristics for various combinations of pH and F-concentrations [21]. Qualitatively, the curves look similar for a very wide range of parameters. The negative differential resistance part of the second peak is explained by the model we present Chap. II.3.

II.2.3 Ionic transport

From the measurements of the reaction products, one cannot conclude on the transport processes in the oxide layer. When the layer grows, do oxygen containing ions pass the oxide layer to oxidize more silicon or do silicon ions migrate towards the electrolyte? Experiments with silicon isotopes indicate that the oxide grows to the inside, not to the outside [31]. Once the ions have passed the oxide layer and arrive at the silicon, the oxidation reaction needs electron holes to proceed [32]. For n-doped silicon this means that an illumination above the silicon band gap is needed. Otherwise a huge voltage is needed to draw an electric current. The realization that ions migrate from the electrolyte through the oxide layer towards the unoxidized silicon is included in the model we present in Chap. II.3.

II.2.4 Photoluminescence and trap hopping

In 1988 a group at the Hokkaido University in Japan showed that under strong anodic bias anodically grown oxide as well as thermal oxide exhibit electroluminescence [32]. Voltages of about 10 V to 200 V were obtained under galvanostatic control depending on doping, current density and duration. The luminescence appeared in changing patterns that eventually became homogeneous. The authors did not pay much attention to the patterns, but they explained the luminescence with electron injection and trap hopping, as reviewed in the model-review chapter. The concept of electron trap-hopping is incorporated in the model in Chap. II.3, where we assume it to be the mechanism by which electrons move through the oxide layer when an oxidation reaction occurs inside the bulk of the oxide layer as opposed to the silicon | oxide-layer interface.

II.2.5 Oscillation shapes and patterns

Oscillations during silicon electrodissolution in fluoride containing solution have been known for a long time [33]. Without the fluoride the oscillations still appear transiently [10]. Over the last couple of years, these oscillations have been investigated in much more detail and more dynamical features have been reported. For instance, there are two types of oscillations that coexist for certain parameter ranges [7, 34]. In this, the coexisting oscillations are not always periodic, but can also be chaotic. The fact that two separate attractors exist could mean that there are two different oscillation mechanisms at work. Furthermore, the coexistence might be linked to spatio-temporal patterns that have been found in the system, including amplitude clusters and chimera states [8, 35]. All these dynamical features occur in a voltage regime where there is an oxide layer on top of the silicon. In Chap. II.3, we model this layer, reproducing many of its properties, but we could not reproduce these oscillations and patterns. This would be a topic for further improvement of the model.

II.2.6 At very high voltages

Ellipsometry allows an estimation of the oxide-layer thickness. For ethylene glycol ($(CH_2OH)_2$) electrolytes with dissolved potassium nitrate (KNO_3), ellipsometric measurements at high voltages ($\sim$100 V) strongly indicate that only a small fraction of the total current goes into oxide formation [32, 36, 37]. A little more recent measurements by Proost et al. yields the same if one compares their electrical current and ellipsometrically measured thickness [10]. They used acetic acid (CH_3CO_2H) in pure water as electrolyte and they also checked their oxide thickness by ex

situ transmission electron microscopy (TEM). The non-oxide-forming current is responsible for the current increase beyond the wide, resonant plateau in Fig. II.1.2. However, the model we present in Chap. II.3 only considers electric current that does lead to oxide formation, which dominates at not so high voltage. Thus, the simulated current voltage curve does not show the measured current increase beyond the plateau.

II.2.7 Electrochemical impedance

The electrochemical impedance of an electrode can often provide deep insight into the ongoing physical processes [38]. Chazalviel et al. measured the impedance of a silicon electrode in a fluoride containing solution [24]. They found that in the resonant voltage regime the impedance could not be explained by traditional impedance models which include resistors for surface reactions, Warburg elements for diffusion, and constant-phase elements for non-ideal surface structures. Instead, their interpretation is that the electrode behaves like an inhomogeneous array of randomly spiking elements [18], which is further described in the corresponding model-review section. However, this interpretation is unlikely, since the electrode surface appears to be perfectly homogeneous during most of the observed oscillations [16]. All in all, the impedance spectrum needs more understanding, especially in the resonant voltage regime, see Fig. II.1.2. The model we present in Chap. II.3 contributes to this by explaining the measured impedance at slightly lower voltages, i.e. in the voltage regime of negative differential resistance.

II.2.8 Limited illumination of n-type silicon

The electro-oxidation of silicon requires electron holes. For n-type silicon this means that it has to be illuminated for the oxidation reaction to proceed. Alternatively, one can apply a very high anodic bias and, thus, create an inversion layer, which provides the necessary holes. The number of holes in the inversion layer grows exponentially with the voltage drop across it, so it behaves like a current limiter in series that claims all the applied voltage down to a certain point, below which its differential resistance becomes small. This is sketched in Fig. II.2.4 for different current limits, i.e. for different illumination strengths. The voltage drawn by the limiter is simply added to the voltage drawn by the electrode, "dragging" the curve to the right. In this sketch, the strange resonant regime is represented by a limit cycle (pink dots) branching from a supercritical Hopf bifurcation, which is a simplification.

Notice that the current-voltage curve becomes Z-shaped when the illumination is limited, yielding three branches of which the middle one is unstable. In order to visualize this Z-shape, the cut-off in Fig. II.2.4 is sketched as much smoother

than it actually is in the experiments, where the top two branches are practically indistinguishable. The emergence of this Z-shape indicates a cusp bifurcation with one saddle-node bifurcation at each "angle" of the Z. As the illumination is lowered, one of the two saddle-node bifurcations moves along the current-voltage curve, the other saddle-node bifurcation quickly moves horizontally to the right and leaves the plot range of Fig. II.2.4 somewhere between the second and third sketched level of illumination (orange and green lines in Fig. II.2.4). In a two parameter plot, this leads to saddle-node bifurcation-curves as shown in Fig. II.2.5 (blue lines).

Fig. II.2.5 also shows a vertical and a horizontal Hopf-bifurcation line (orange). The vertical line follows from the assumption that there is a Hopf bifurcation at strong illumination. As long as the illumination is sufficiently strong and, thus, the current limit sufficiently high, the Hopf bifurcation will always occur a the same voltage, as it does for all the sketched limits in Fig. II.2.4. Hence, there is the vertical Hopf-bifurcation line in Fig. II.2.5.

The horizontal Hopf-bifurcation line (orange) and the other bifurcations (red and green) in Fig. II.2.5 are somewhat more speculative. The main question is: What kind of bifurcation makes the limit cycle oscillations disappear when the illumination is gradually lowered, e.g. going from (5, 1.1) to (5, -0.1) in Fig. II.2.5? It is rather likely that there is some sort of codimension-two point involved close to the point (2, 0.2) in Fig. II.2.5. If this codimension-two point were a Bogdanov-Takens bifurcation [39], it would mean that the limit cycle disappears in a homoclinic bifurcation as the illumination is lowered. Another possible codimension-two point would be a Fold-Hopf bifurcation [40], which has one zero and two purely imaginary, complex conjugate eigenvalues. A Fold-Hopf bifurcation can have various complicated unfoldings and even imply a local birth of chaos. One possible scenario is sketched in Fig. II.2.5, where the limit cycle is destabilized in a subcritical secondary Hopf-bifurcation

For the model that we develop in Chap. II.3, we take away that it is probably sufficient to cover p-silicon. Weakly illuminated n-silicon can then be represented with a current limiter that is connected in series.

II.2.9 Model by Cattarin et al.

The steady-state electric current through a silicon anode depends mainly on three parameters: The electrode potential, the fluoride concentration, and the pH value [21]. For the latter two parameters, Cattarin et al. proposed a model [27], in which they considered a rotating disk electrode with the corresponding flow field in front. They obtained ordinary differential equations (ODE) for the concentrations in the diffusion layer. The boundary conditions of this ODEs were 'constant concentration' on the bulk side and 'reaction-flow consistency' on the electrode-surface side. The

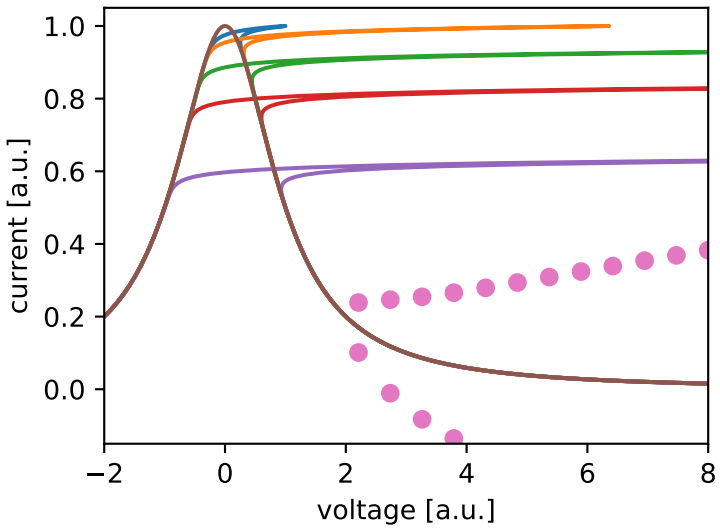

Figure II.2.4: A sketch of the current-voltage curve around the second current peak for different illumination strengths (current limits) for n-type silicon in HF solution. The pink dots represent a limit cycle oscillation.

values of the constant concentrations can be calculated from the pH and potential, but the reactions and rates for the reaction-flow consistency needed some creative work to be formulated: Knowing the reactants and products, Cattarin et al. proposed that SiO_2 can be dissolved in reaction II.2.13, II.2.14, or II.2.15.

$$6HF + SiO_2 \xrightarrow{k_1} SiF_6^{2-} + 2H_2O + 2H^+ \tag{II.2.13}$$

$$3HF_2^- + H^+ + SiO_2 \xrightarrow{k_2} SiF_6^{2-} + 2H_2O \tag{II.2.14}$$

$$2HF_2^- + 2HF + SiO_2 \xrightarrow{k_3} SiF_6^{2-} + 2H_2O \tag{II.2.15}$$

Their central idea now was about the rates of these reactions. They assumed that reaction II.2.13, II.2.14, and II.2.15 are linearly proportional to $[HF]^2$, $[HF_2^-]^2$, and $[HF][HF_2^-]$ respectively. With these rates, they were able to reproduce measured current-pH curves and current fluoride-concentration curves very well, at fluoride concentrations above $0.03\,\mathrm{mol{\cdot}l^{-1}}$ and at fixed electrode potential of 2.2 V vs saturated calomel electrode (SCE).

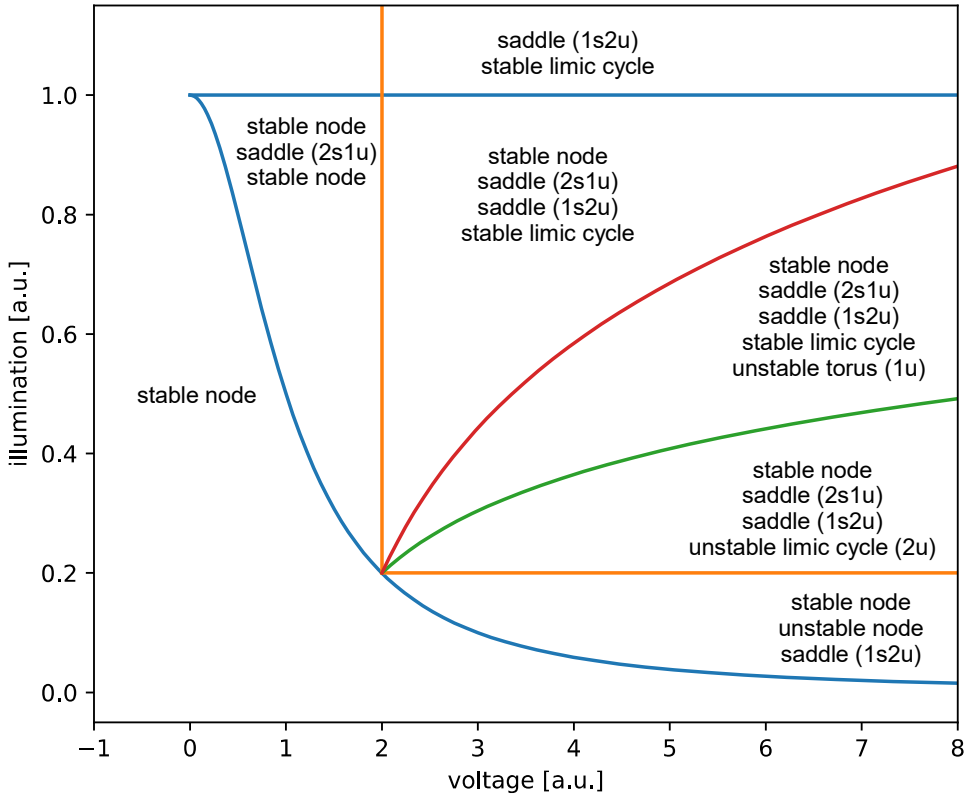

Figure II.2.5: Sketch of a possible bifurcation diagram for n-Si in HF solution: Saddle-node bifurcation (blue), Hopf bifurcation (orange), homoclinic bifurcation between a saddle and a torus (red), secondary Hopf-bifurcation (green). For ambiguous cases the number of stable and unstable directions is given in brackets. In this simple sketch, the illumination is basically just the current limit, since the two are proportional anyway.

II.2.10 Model by Chazalviel et al.

Some authors claim that differential equations are not suited to describe the system. In 1992, Chazalviel and Ozanam came up with the idea of self-oscillating micro-domains [18] to describe the complicated impedance spectra they obtained [24]. In their model, they postulate that the electrode is made up of microscopic, stochastic oscillators that randomly switch on that are coupled and can, thus, synchronize. The degree of synchronization determines the global current and voltage. This approach was adapted by Föll et al. in 1998 [41–43] and by Lewerenz et al. in 2000 [44, 45] who proposed different interpretations for the local oscillators. In the model by Lewerenz et al., cracks form in layers under compressive stress which seems like an unphysical assumption, because one would rather expect cracks to form under tensile or shear stress. In the model by Föll et al., the oscillation is assumed to occur due to a breakdown caused by the electric field, which at first seems more convincing from a physical point of view. However, this idea of a critical breakdown voltage has been refuted by Proost et al., who investigated transient oscillations in a fluorite-free electrolyte [10]: They used galvanostatic control and found that the magnitude of the electric field, at which their recurring voltage drops occurred, was significantly different for each period, becoming smaller and smaller as the equilibrium was approached. Moreover, ellipsometric measurements by our group showed that the micro-domains are rather unlikely, because the oxide happens to oscillate fully homogeneously, at least most of the time [16].

II.2.11 Model by Hasegawa et al.

In an organic, fluoride free electrolyte the voltage grows continuously under galvanostatic control and after some minutes the voltage takes a linear time dependence [32, 36]. This happens at voltages above 20 V. Hasegawa et al. proposed the following model to describe the oxide growth they observed in this linear regime for p-silicon:

$$\frac{\mathrm{d}}{\mathrm{d}t}x = AJ \tag{II.2.16}$$

$$J = B\exp(CU_\mathrm{p}/x) \tag{II.2.17}$$

where x is the oxide thickness, U_p and J are the cell voltage and current density respectively and A, B, C are constants. A depends on the molar density of the oxide and on the formation efficiency, i.e. the fraction of current that is associated with oxide formation. B and C describe the tunneling of electrons out of trapped states in the oxide. Thus it depends on the electric field ($\propto U_\mathrm{p}/x$) in the oxide.

Furthermore, they interpret the higher voltage U_n measured with n-silicon as the break-down voltage across the electron depleted space-charge layer in the silicon. They claim that a break down is necessary to achieve the given current because it creates the holes needed for oxide formation.

$$U_n = U_p + k_0(1 - k_1 / I_{photon})^n \tag{II.2.18}$$

Equation II.2.18 describes the break-down voltage depending on the illumination I_{photon} with k_0, k_1, n being constants.

The model qualitatively explains the two peaks they found in the luminescence spectrum. The first peak has a photon energy similar to the difference between the conduction band energies of Si and SiO_2. The second peak is close to the 2 eV traps found in thermal SiO_2 [11]. They found the same luminescence spectrum applying anodic bias to a silicon electrode with thermally grown oxide, instead of anodically grown oxide. Under cathodic bias the first peak disappeared while the second remained, which is consistent with their interpretation.

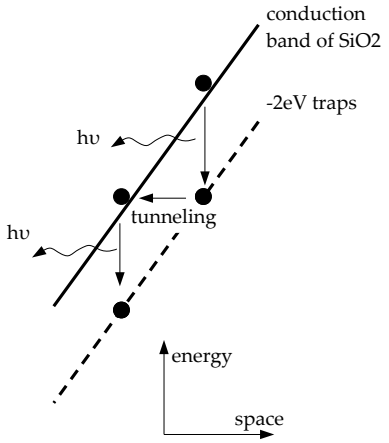

Figure II.2.6: Model by Hasegawa et al. for the electron transport in thermal and anodic oxide [32].

II.2.12 Model by Krischer et al.

P-type silicon anodes show very typical current-voltage curves [21], strange resonance [24] and oscillations [7], depending on the parametric conditions. This characteristic behavior of p-type silicon anodes is also seen with n-type silicon anodes if the missing holes are provided via photo illumination [19, 46]. Larger currents require more photons [23]. Under certain conditions, if the illumination is

chosen such that the current is illumination-limited during a certain phase range of an oscillation, very complex, spatiotemporal patterns emerge in the oxide layer thickness, which has been measured with ellipsometry [14].

Despite their complexity, the spatio-temporal patterns can be qualitatively reproduced by a remarkably simple partial differential equation, which represents a spatially extended medium at the onset of oscillation [13, 15]:

$$\partial_t W(x,t) = \overbrace{W(x,t)}^{\text{linear local dynamics}} \overbrace{+(1+ic_1)\nabla^2 W(x,t)}^{\text{linear local coupling}} \overbrace{-(1+ic_2)|W(x,t)|^2 W(x,t)}^{\text{first non-linear term of local dynamics}} \underbrace{-(1+i\nu)\langle W\rangle(t)}_{\text{linear global coupling}} \underbrace{+(1+ic_2)\langle |W|^2 W\rangle(t)}_{\text{non-linear global coupling}} \tag{II.2.19}$$

Equation II.2.19 is a modified version of the complex Ginzburg-Landau equation (MCGLE) [47].

II.2.13 Summary and Conclusion

Silicon is one of the mostly investigated materials and there are many models for the self-organization phenomena it shows in hydrofluoric solution. However, as you can see in Tab. II.2.2, we are still quite far from a model that captures all the complex behavior of the Si-HF system. Researchers that have been particularly active in modeling these complex phenomena were Lehmann at the Siemens AG in Munich, the Palaiseau group around Chazalviel and Ozanam, the Kiel group around Föll, the group in Berlin around Lewerenz, and our group in Munich around Krischer. Looking at our model in the last row of Tab. II.2.2, we see that it explains a wide range of phenomena with only a few reasonable assumptions and, thus, contributes to the overall understanding of the Si-HF system. The model is covered in Chap. II.3.

	oxide layer thickness	current-voltage curve	impedance spectrum	pores	oscillation	contribution of electrolyte	luminescence	dissolution valence	main assumptions
Oscillating micro domains by Chazalviel et al. [18]	–	–	looks complicated, like spectra in [24], but qualitatively different	–	postulated locally	–	–	–	stochastically oscillating domains
Current burst by Föll et al. [41–43]	–	–	–	2D simulation	transient and sustained, postulated locally	–	–	–	no e^--tunneling, stochastic bursts, synchronizing and desynchronizing mechanisms
Lehmann [30, 48]	–	–	–	dependence of macro-pore shape on voltage and doping	–	–	–	–	current is either of or off
Model about HF, HF_2^-, F^- by Cattarin et al. [27]	–	–	–	–	–	dependence of current on pH, C_F, rpm, at 2.2 V vs SCE	–	–	dissolution rates of second order in [HF] and $[HF_2^-]$
Monte Carlo pore growth by Erlenbacher et al. [49]	–	–	–	random growth of micro pores into bulk	–	–	–	–	random pore growth
Wet oxide model [25]	positive slope below second peak	positive slope below second peak	–	–	–	–	–	–	a wet and a dry oxide layer
Thick oxide growth by Hasengawa et al. [32]	temporal evolution	at very large voltage	–	–	–	–	relation between thickness and luminescence spectra	–	large voltage, thick oxide layer, luminescence patterns are negligible
MCGLE by Schmidt et. al [13, 15]	–	–	–	–	spatio-temporal patterns	–	–	–	oscillating medium
Capacitance mediated oscillator by Zensen et al. [17]	–	–	–	–	homogeneous oscillations	–	–	–	oscillating medium
This thesis and ref. [2]	voltage dependence of the layer thickness	negative differential resistance after second peak	two semi-circles match measurement	–	–	–	–	qualitative trend of its voltage dependence	substoichiometric oxide, composition dependent etch rate

Table II.2.2: Summary of several models, their assumptions, and of the features they reproduce

Chapter II.3

Model definition

In this Section, we model the oxide layer, SiO_x, that covers the Si anode in hydrofluoric solution. We aim to reproduce the negative-differential resistance, i.e. $\mathrm{d}I/\mathrm{d}\varphi_{\mathrm{WE}} < 0$, where I is the electric current and φ_{WE} is the potential of the working electrode.

II.3.1 Concept

In this model it is assumed that the electrodissolution of Si occurs in three steps, which are sketched in Figure II.3.1. The initial step is silicon oxidation at the interface between the silicon and the oxide layer. In this step, the oxide layer grows into the silicon electrode. The pure silicon is, thus, replaced by a partially oxidized silicon species, e.g. SiO.

The second step happens inside the layer volume and transforms the partially oxidized silicon, SiO, into the final oxidation state, SiO_2. In reality, the transformation from Si to SiO_2 is likely to involve several sub-steps and further intermediate oxidation states, correspondingly. These sub-steps are merged for simplicity in this model. In the third and final step the layer is etched away purely chemically. The etch rate is assumed to depend on the oxide composition and to be faster if the fraction of partial oxide is higher.

One possible way to realize the mechanism we stated above is given by the following set of reactions. Ions O^{2-} enter the oxide layer by a reaction like:

$$(H_2O)_{\mathrm{solution}} \rightleftharpoons 2(H^+)_{\mathrm{solution}} + (O^{2-})_{\mathrm{layer}} \tag{R0}$$

Under the present high electric fields ($\sim 1\,\mathrm{V/nm}$) the ions travel through the layer and oxidize the silicon in two steps

$$\mathrm{Si} + 2h^+ + O^{2-} \xrightarrow{k_1} \mathrm{SiO} \tag{R1}$$

$$\mathrm{SiO} + \alpha h^+ + O^{2-} \xrightarrow{k_2} SiO_2 + (2-\alpha)e^-, \quad \text{with } 0 < \alpha < 2 \tag{R2}$$

or in just a single step

$$\mathrm{Si} + 4\mathrm{h}^+ + 2\mathrm{O}^{2-} \xrightarrow{k_3} \mathrm{SiO_2} \tag{R3}$$

Reaction (R1), occurs at rate $r_1(t)$ at the boundary between silicon and a mixed layer of SiO and SiO_2. This mixture is referred to as SiO_x in the following. Inside the mixed oxide layer the SiO created in Reaction (R1) can be further oxidized to SiO_2 in Reaction (R2) at rate $r_2(x,t)$. Alternatively, Si can be directly oxidized to SiO_2 in Reaction (R3) at rate $r_3(t)$.

The last step is the etching of oxide at the boundary between oxide and solution with a rate $r_{\mathrm{etch}}(t)$ depending on the oxide composition right at the boundary. The corresponding reaction reads

$$\mathrm{SiO}_x + 6\mathrm{HF} \rightarrow \mathrm{SiF}_6^{2-} + x\,\mathrm{H_2O} + 2\mathrm{H}^+ + (2-x)\mathrm{H_2} \tag{R4}$$

with some x between 1 and 2. As detailed above, the dissolution of SiO_2 in hydrofluoric solution is well investigated [20, 27] and more complicated than Reaction (R4), but our simplification will serve the purpose.

II.3.2 Kinetic description

We transcribed the ideas from Section II.3.1, which are sketched in Figure II.3.1, to a set of coupled partial differential equations of time t and of one spatial dimension x which points perpendicularly away from the electrode surface. These partial differential equations describe the transport and the reactions inside the oxide layer and at its boundaries. As etching and reaction (R1) and (R3) proceed, the corresponding interfaces move. Let $x_{\mathrm{a}}(t)$ and $x_{\mathrm{b}}(t)$ be the time dependent position of the Si/SiO_x and SiO_x/solution interfaces, respectively. Assuming a constant molar oxide density n_{ox} for simplicity, the velocities can be written in terms of the respective reaction rates:

$$\partial_t x_{\mathrm{a}}(t) = -\frac{1}{n_{\mathrm{ox}}}(r_1(t) + r_3(t)) \tag{II.3.1}$$

$$\partial_t x_{\mathrm{b}}(t) = -\frac{1}{n_{\mathrm{ox}}} r_{\mathrm{etch}}(t) \tag{II.3.2}$$

where the rates per unit area $r_1(t)$, $r_3(t)$ and $r_{\mathrm{etch}}(t)$ are defined below in Equation (II.3.3), (II.3.4) and (II.3.5).

Since we exclusively consider situations where the silicon surface is covered with some (though possibly thin) oxide layer, the rates $r_1(t)$ and $r_3(t)$ are assumed to be limited solely by a lack of O^{2-} ions. Silicon and h^+, the other reactants involved, are present in high concentrations because we consider p-type silicon under anodic bias.

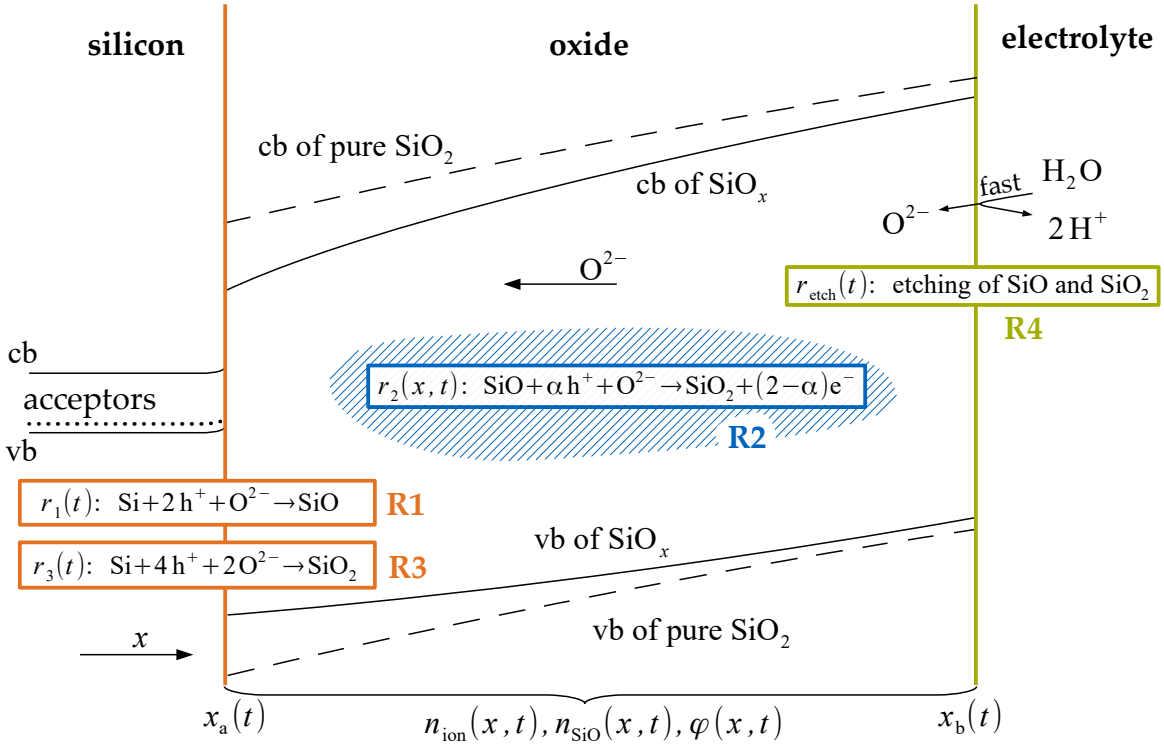

Figure II.3.1: A sketched band diagram of the model with all the variables that define a state: Interface positions $x_a(t)$ and $x_b(t)$, concentration of O^{2-} ions $n_{ion}(x,t)$, concentration of intermediate oxide $n_{SiO}(x,t)$ and electric potential $\varphi(x,t)$. The bandgap of SiO_x (solid black line) is smaller than that of pure SiO_2 (dashed black line) [50]. Furthermore, the reaction that allows O^{2-} to enter the oxide layer is assumed to be fast compared to the transport inside the layer, so that the chemical potential of O^{2-} at $x_b(t)$ is prescribed by the electrolyte.

The etch rate $r_{\text{etch}}(t)$ for a certain oxide mixture is linearly interpolated between the etch rate of pure SiO_2 and the etch rate of pure SiO with proportionality coefficients η_{SiO_2}, η_{SiO}:

$$r_1(t) = k_1 n_{\text{ion}}(x_a(t), t) \tag{II.3.3}$$
$$r_3(t) = k_3 [n_{\text{ion}}(x_a(t), t)]^2 \tag{II.3.4}$$
$$r_{\text{etch}}(t) = \eta_{SiO} n_{SiO}(x_b(t), t) + \eta_{SiO_2} [n_{ox} - n_{SiO}(x_b(t), t)] \tag{II.3.5}$$

where n_{ox} is the molar density of silicon in the oxide, and $n_{SiO}(x,t)$, $n_{\text{ion}}(x,t)$ are the molar densities of SiO and O^{2-} respectively. The concentration of SiO_2 is expressed as $n_{ox} - n_{SiO}(x,t)$. Hereby we assume SiO_2 to be the non-SiO fraction of the entire molar oxide density n_{ox}. The rate coefficients k_1 and k_3 depend on the potential drop across the space charge layer which is assumed to be constant in our model, because the differential capacity of the space charge layer is large. Thus, k_1 and k_3 are constant as well.

Unlike the reactions (R1) and (R3) which are interface reactions, reaction (R2) occurs inside the oxide volume. From the participating species we expect electrons/holes to leave/enter the oxide quickly via direct tunneling or trap hopping which has been observed in the electroluminescence spectra of electrically biased oxide films [32]. The remaining degrees of freedom in the oxide layer are then the concentrations of SiO and O^{2-}. The dynamics of these two species is dictated by their respective mass balance equations which contain transport and reaction terms:

$$\partial_t n_{\text{ion}}(x,t) = -\nabla J_{\text{ion}}(x,t) - r_2(x,t) \tag{II.3.6}$$
$$\partial_t n_{SiO}(x,t) = -\nabla J_{SiO}(x,t) - r_2(x,t) \tag{II.3.7}$$

where $J_{\text{ion}}(x,t)$ and $J_{SiO}(x,t)$ are the molar fluxes of O^{2-} and SiO respectively.

Let $\varphi(x,t)$ be the electrostatic potential. Since O^{2-} is the only charged species considered inside the oxide, the total charge density in the layer is $z_{\text{ion}} F n_{\text{ion}}(x,t)$, where z_{ion} is the number elementary charges per ion, i.e. -2, and F is the Faraday constant. Poisson's equation thus reads:

$$\nabla^2 \varphi(x,t) = -\frac{z_{\text{ion}} F}{\varepsilon_{ox}} n_{\text{ion}}(x,t) \tag{II.3.8}$$

Introducing the diffusion constants D_{ion}, D_{SiO} and the rate coefficient k_2, the transport and reaction terms in Equation (II.3.6) and (II.3.7) can be modeled as:

$$J_{\text{ion}}(x,t) = -D_{\text{ion}} \nabla n_{\text{ion}}(x,t) + \frac{D_{\text{ion}} z_{\text{ion}} F}{RT} n_{\text{ion}}(x,t) \nabla \varphi(x,t) \tag{II.3.9}$$
$$J_{SiO}(x,t) = -D_{SiO} \nabla n_{SiO}(x,t) \tag{II.3.10}$$
$$r_2(x,t) = k_2 n_{\text{ion}}(x,t) n_{SiO}(x,t) \tag{II.3.11}$$

where diffusive transport was assumed to be Fickian in Eq. (II.3.9), (II.3.10) and the Einstein-Smoluchowski relation was used to derive the ionic migration term in Equation (II.3.9). R and T are the gas constant and absolute temperature, respectively. The diffusion of SiO reflects the thermal restructuring of the solid oxide.

II.3.3 Boundary conditions

Continuity yields Equation (II.3.12) and (II.3.13) as boundary conditions for the Si/SiO_x interface at x_a:

$$J_{ion}(x_a(t),t) = -r_1(t) - 2r_3(t) + n_{ion}(x_a(t),t)\,\partial_t x_a(t) \quad \text{(II.3.12)}$$

$$J_{SiO}(x_a(t),t) = r_1(t) + n_{SiO}(x_a(t),t)\,\partial_t x_a(t) \quad \text{(II.3.13)}$$

For the SiO_x/solution interface at $x_b(t)$ we assume a certain fixed concentration n^0_{ion} of O^{2-} that is tantamount to assuming that Reaction (R0) is always in equilibrium. The oxide dissolution is accounted for by the movement of the SiO_x/solution interface in Equation (II.3.2). Thus, the flux of SiO at the boundary should be set to zero:

$$n_{ion}(x_b(t),t) = n^0_{ion} \quad \text{(II.3.14)}$$

$$J_{SiO}(x_b(t),t) = 0 \quad \text{(II.3.15)}$$

To come up with the boundary conditions for the electrostatic potential $\phi(x,t)$ we made the following simplifying assumption about the space-charge layer. The differential capacity of the space charge layer of p-type silicon under strong anodic bias is very large, like in the case of a metal-insulator-semiconductor capacitor [51]. The same is true for the Helmholtz layer which also has a large capacity. Therefore, any change in the total applied voltage will drop on the much smaller capacitor formed by the oxide layer. Thus, the oxide sees the externally applied voltage with a fixed offset, which is exemplary illustrated in Fig. II.3.2. In the example in Fig. II.3.2, the voltage drop across the space charge layer $\Delta\phi_1$ complies with

$$\Delta\phi_1 = \frac{2kT}{e}\ln\left(\frac{Q_{sc}}{(2\epsilon_0\epsilon_{Si}\,kT\,N_d)^{0.5}}\right), \quad \text{(II.3.16)}$$

where $N_d = 10^{21}\mathrm{m}^{-3}$ and $\epsilon_{Si} = 11.7$. Assume the oxide layer and the Helmholtz layer had constant capacities C_{ox}, C_h:

$$C_{ox} = \frac{\epsilon_{ox}\epsilon_0}{d_{ox}} = \frac{1\cdot 8.854\cdot 10^{-12}\mathrm{AsV}^{-1}\mathrm{m}^{-1}}{5\cdot 10^{-10}\mathrm{m}} = 4.07\,\mu\mathrm{F\,cm}^{-2} \quad \text{(II.3.17)}$$

$$C_h = \frac{\epsilon_{water}\epsilon_0}{d_h} = \frac{6\cdot 8.854\cdot 10^{-12}\mathrm{AsV}^{-1}\mathrm{m}^{-1}}{7.6\cdot 10^{-10}\mathrm{m}} = 6.99\,\mu\mathrm{F\,cm}^{-2} \quad \text{(II.3.18)}$$

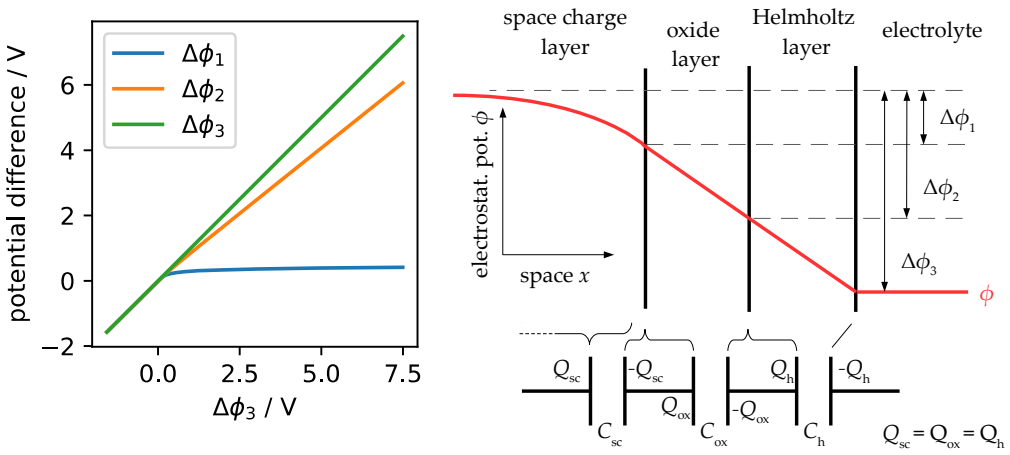

Figure II.3.2: This example illustrates that, under forward bias, the space charge layer almost acts as a constant voltage offset.

The resulting potential differences $\Delta\phi_1$, $\Delta\phi_2$, $\Delta\phi_3$ then indicate that the differential space-charge layer capacity is negligibly large within the voltage regime in question. Furthermore, the contribution of the Helmholtz layer appears to be small, even when the oxide-layer thickness d_{ox} is as small as $5 \cdot 10^{-10}$m.

Under the said assumptions, we end up with the following boundary conditions for the electrostatic potential:

$$\varphi(x_{\mathrm{a}}(t), t) = U(t) \tag{II.3.19}$$
$$\varphi(x_{\mathrm{b}}(t), t) = 0 \tag{II.3.20}$$

where $U(t)$ equals the externally applied voltage plus/minus a constant offset.

II.3.4 Total electric current

The total electric current $I(t)$ that flows into the working electrode is the sum of the reaction current $I_{\mathrm{reac}}(t)$ and capacitive charging current $I_{\mathrm{ch}}(t)$.

$$I(t) = I_{\mathrm{reac}}(t) + I_{\mathrm{ch}}(t) \tag{II.3.21}$$

The current $I(t)$ is used in Sec. II.4 to predict a cyclic voltammogram and an impedance spectrum and is compared to electrochemically measured data.

The reaction current $I_{\mathrm{reac}}(t)$ is calculated from the reaction rates $r_1(t)$, $r_3(t)$ and $r_2(x,t)$, where $r_1(t)$,$r_3(t)$ were defined as rates per surface area and $r_2(x,t)$ as a rate

per unit volume.

$$I_{\mathrm{reac}}(t) = 2F \left[r_1(t) + 2 \cdot r_3(t) + \int_{x_{\mathrm{a}}(t)}^{x_{\mathrm{b}}(t)} \mathrm{d}x\, r_2(x,t) \right] \tag{II.3.22}$$

Remember that we assumed that the electrons/holes created/consumed in the bulk at rate $r_2(x,t)$ leave/enter the oxide via trap hopping or direct tunneling, more or less immediately. Thus, the current resulting from $r_2(x,t)$ is contributing to $I_{\mathrm{reac}}(t)$ without any further delay.

The capacitive charging current $I_{\mathrm{ch}}(t)$ is calculated from the electric potential $\varphi(x,t)$ as

$$I_{\mathrm{ch}}(t) = -\varepsilon_{\mathrm{ox}}\, \partial_t \left[\lim_{h \searrow 0} \partial_x \varphi(x_{\mathrm{a}}(t) + h, t) \right] \tag{II.3.23}$$

which is simply the time derivative of the integrated space charge in the semiconductor. Equation (II.3.23) was obtained by integrating Poisson's equation from $-\infty$ to $x_{\mathrm{a}}(t) + h$ and differentiating both sides of the equation with respect to t.

II.3.5 Implementation

The numerical results in the next chapter were obtained with the proprietary finite element software COMSOL 5.2 [52]. We solved partial differential equations numerically on a one dimensional spatial domain perpendicularly to the electrode, which represents the oxide layer of finite thickness. From the available physics components in COMSOL, we used the 'General Form PDE' component for chemical species, the 'Poisson's Equation' component for the electrostatic potential, and the 'Moving Mesh' component to simulate the growth and dissolution of the oxide layer. The spatial domain was split into 2000 finite elements of the same length, which were adapted continuously as the boundaries moved. All simulations were run with the COMSOL-study 'Time Dependent' and all solver configurations were left at their default except for the 'Relative tolerance' which we reduced to 10^{-7} for the electric impedance calculations and to 10^{-5} in all other cases. All the parameters, variables and physical constants used in the simulations are listed in Tab. II.3.1, II.3.2, II.3.3.

II.3.6 Discussion

There are quite some tunable parameters in the model. The electrochemical potential of ions in equilibrium and the transport and reaction rates were chosen somewhat arbitrarily, but for the remaining parameters one can make an educated guess. For the molar density n_{ox} and the permittivity $\varepsilon_{\mathrm{ox}}$ one can approximately take known

Notation	Value	Meaning
n_{ox}	$4.381 \cdot 10^{-2}\,\mathrm{mol\,cm^{-3}}$	molar oxide density
n^0_{ion}	$9.36 \cdot 10^{-5}\,\mathrm{mol\,cm^{-3}}$	O^{2-} concentr. in equilib. with solution
D_{ion}	$1.1962 \cdot 10^{-13}\,\mathrm{cm^2\,s^{-1}}$	diffusion coefficient of O^{2-}
D_{SiO}	$3.2 \cdot 10^{-16}\,\mathrm{cm^2\,s^{-1}}$	diffusion coefficient of SiO
k_1	$1600\,\mathrm{cm\,s^{-1}}$	reac. coeff. of first oxidation step
k_2	$2.048 \cdot 10^{4}\,\mathrm{cm^3 mol^{-1}\,s^{-1}}$	reac. coeff. of second step
k_3	$3 \cdot 10^{15}\,\mathrm{cm^4 mol^{-1} s^{-1}}$	reac. coeff. of direct SiO_2 production
U	$2\,\mathrm{V}$	electrode voltage with offset
$\varepsilon_{\mathrm{ox}}$	$1 \cdot \varepsilon_0$	permittivity of mixed oxide
$\varepsilon_{\mathrm{Si}}$	$-$	permittivity of silicon
η_{SiO}	$6 \cdot \eta_{\mathrm{SiO_2}}$	etch velocity of pure SiO
$\eta_{\mathrm{SiO_2}}$	$2.09 \cdot 10^{-8}\,\mathrm{cm\,s^{-1}}$	etch velocity of pure SiO_2

Table II.3.1: Default parameters used if not stated otherwise

Notation	Unit	Meaning
$I(t)$	$[\mathrm{A\,m^{-2}}]$	externally measurable electric current
$I_{\mathrm{ch}}(t)$	$[\mathrm{A\,m^{-2}}]$	current connected to capacitive charging
$I_{\mathrm{reac}}(t)$	$[\mathrm{A\,m^{-2}}]$	current connected to reactions
$J_{\mathrm{ion}}(x,t)$	$[\mathrm{mol\,m^{-2}\,s^{-1}}]$	flux of O^{2-}
$J_{\mathrm{SiO}}(x,t)$	$[\mathrm{mol\,m^{-2}\,s^{-1}}]$	flux of SiO
$n_{\mathrm{ion}}(x,t)$	$[\mathrm{mol\,m^{-3}}]$	concentration of O^{2-}
$n_{\mathrm{SiO}}(x,t)$	$[\mathrm{mol\,m^{-3}}]$	concentration of SiO
$q(t)$	$[\mathrm{C\,m^{-2}}]$	Si space charge plus surface charge
$r_1(t)$	$[\mathrm{mol\,m^{-2}\,s^{-1}}]$	rate of the reaction in Eq. (R1)
$r_2(x,t)$	$[\mathrm{mol\,m^{-3}\,s^{-1}}]$	rate density of the reaction in Eq. (R2)
$r_3(t)$	$[\mathrm{mol\,m^{-2}\,s^{-1}}]$	rate of the reaction in Eq. (R3)
$r_{\mathrm{etch}}(t)$	$[\mathrm{mol\,m^{-2}\,s^{-1}}]$	rate of etching
t	$[\mathrm{s}]$	time coordinate
x	$[\mathrm{m}]$	spatial coordinate perpendicular to surface
$x_{\mathrm{a}}(t)$	$[\mathrm{m}]$	position of the Si/SiO_x interface
$x_{\mathrm{b}}(t)$	$[\mathrm{m}]$	position of the SiO_x/solution interface
$\nu(t)$	$[1]$	dissolution valence, i.e. e^- transferred per Si dissolved
$\varphi(x,t)$	$[V]$	electrostatic potential
$\Delta\varphi_{\mathrm{WE}}(t)$	$[V]$	voltage between working and reference electrode

Table II.3.2: Variables

Notation	Value	Meaning
F	$96.485\,\mathrm{C\,mol^{-1}}$	Faraday constant
T	$293\,\mathrm{K}$	assumed room temperature
z_{ion}	-2	elementary charges per O^{2-}
ε_0	$8.854 \cdot 10^{-12}\,\mathrm{F\,m^{-1}}$	vacuum permittivity

Table II.3.3: Physical constants

values of thermal oxide. The etch rates of partial and stoichiometric oxide η_{SiO}, $\eta_{\mathrm{SiO_2}}$ can be roughly estimated from the experimentally observed etch rates. The offset between the model voltage parameter U and the actual voltage across the interface can be estimated considering the dependence of the space charge layer's differential capacity on the voltage drop across it.

Although the reactions that we assumed above lead to good predictions, the mechanism could probably also be implemented with other reactions. One could for example consider OH^- ions and $Si(OH)_x$ instead of O^{2-} ions and SiO_x.

Chapter II.4

Simulation results

In this chapter we compare the model simulations to measured data. The the measurements have been performed by Maximilian Patzauer and Dominique Koster. The results are published in [2].

II.4.1 Current-voltage characteristics

The model is supposed to reproduce the negative slope in the current-voltage characteristics. In an electrochemical set up, this negative slope is measured between the maximum of the second current peak and the resonant current plateau in Figure II.1.2 if the applied voltage is cycled. We simulated such cyclic voltammetry by making the model parameter U a periodic triangular function of time, since U represents the potential difference between the silicon electrode and the electrolyte. The parameter U differs from the actual applied voltage by an offset due to the space charge layer and the Helmholtz layer, which are discussed in Section II.3.3, but are not quantified in this model. After an initial transient the resulting voltammogram is robust for a wide range of initial conditions. Figure II.4.1 shows a simulated voltammogram with a scan rate of $1\,\mathrm{mV\,s^{-1}}$ and the corresponding electrochemical measurement. In both curves the current decreases with higher electrode potential.

II.4.2 Oxide layer properties

The thickness of the oxide layer as obtained during the simulated cyclic voltammetry is plotted in Figure II.4.2, together with the corresponding electrochemical measurement which shows an in-situ ellipsometric signal. The ellipsometric signal is approximately proportional to the oxide layer thickness but also depends on the refractory index inside the layer and in front of it. It can be used as a qualitative estimation of the layer thickness [9]. In both plots the thickness increases with the applied voltage.

The main idea of the model is that the etch rate of the oxide depends on its composition. Thus, let us have a look at Fig. II.4.3 (Top) which shows the stationary

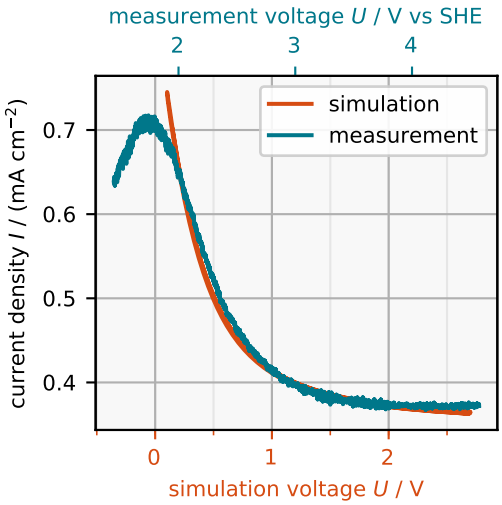

Figure II.4.1: Comparison of simulated and measured cyclic voltammograms. Orange: Cyclic voltammogram obtained from the model described in Chapter II.3 at a scan rate of 1 mV/s, using the parameters in Table II.3.1. Blue: Cyclic voltammogram at 1 mV/s of a (111) p-silicon electrode of 5 to 25 Ω cm in a solution of 0.05 M NH_4F and 0.025 M H_2SO_4 (pH 2.3)

oxide composition for some voltages U. With increasing voltage U the stationary layer thickness $x_b(t) - x_a(t)$ increases. Consider the four cases in Fig. II.4.3 (Top).The concentration of partial oxide $n_{SiO}(x,t)$ is the highest at the Si/SiO_x interface $x_a(t)$, where the partial oxide is created. Closer to the SiO_x/solution interface $x_b(t)$ the fraction of partial oxide becomes smaller as it is used up in Reaction (R2). The remaining fraction right at the SiO_x/solution interface $x_b(t)$ determines the etch rate by Equation (II.3.5). Note that this fraction of partial oxide is much smaller at the SiO_x/solution interface if the layer is thicker and U is larger. This comes from an increased volume that is available for the ions $n_{ion}(x,t)$ to participate in the bulk Reaction (R2), which consumes partial oxide. Consequently, if U is larger, the layer is etched more slowly, according to Equation (II.3.5).

The concentration of ions $n_{ion}(x,t)$ is the highest at the SiO_x/solution interface $x_b(t)$ where the electrochemical potential of O^{2-} in the oxide and the electrochemical potentials of protons and water in the electrolyte are assumed to be in equilibrium. With increasing distance from the SiO_x/solution interface $x_b(t)$, which corresponds to going left in Fig. II.4.3 (Top), the concentration of ions decreases. This is because the ions enter the oxide at the SiO_x/solution interface $x_b(t)$ and are then used up in the oxide volume by Reaction (R2) and at the Si/SiO_x interface $x_a(t)$ by

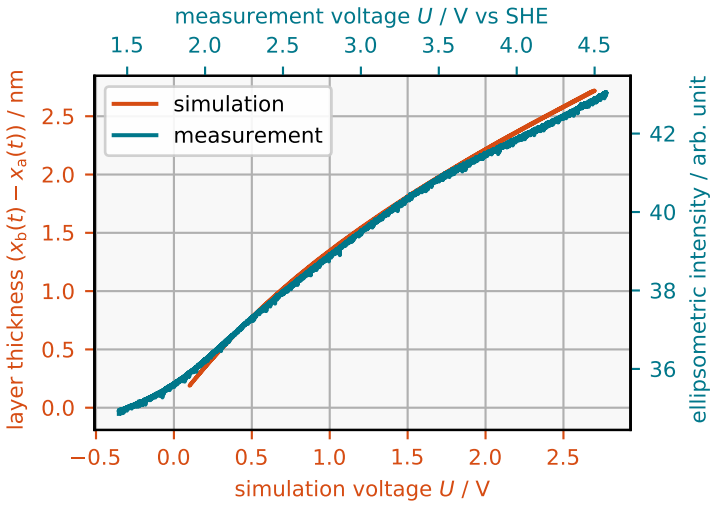

Figure II.4.2: Comparison of the simulated oxide layer thickness during a slow voltage scan and the corresponding experimental in-situ ellipsometric signal which is proportional to the layer thickness [9]. Orange: Oxide layer thickness vs. voltage U during simulated cyclic voltammetry using the model described in Chapter II.3 at a scan rate of 1 mV/s, with the parameters of table II.3.1. Blue: Ellipsometric intensity representing the oxide layer thickness during a 1 mV/s cyclic voltage scan of (111) p-silicon of 5 to 25 Ω cm in a solution of 0.05M NH_4F and 0.025M H_2SO_4 (pH2.3)

Reaction (R1) and (R3). The concentration of ions in the layer determines the curvature of the electrostatic potential $\varphi(x,t)$ in Fig. II.4.3 (Bottom) by Poisson's equation. Its derivative gives us the electric field $-\partial_x\varphi(x,t)$, which monotonically increases from about 0.2 V/nm at the SiO_x/electrolyte interface to 2-3 V/nm at the Si/SiO_x interface.

II.4.3 Dissolution valence

We calculated the reaction valence $\nu(t)$ in the presented model in terms of the reaction current $I_{\mathrm{reac}}(t)$, the Faraday constant F, the Si/SiO_x interface position $x_{\mathrm{a}}(t)$ and the molar density of Si-atoms in the SiO_x layer n_{ox} :

$$\nu(t) = \frac{I_{\mathrm{reac}}(t)}{F\,\partial_t x_{\mathrm{a}}(t)\,n_{\mathrm{ox}}}. \tag{II.4.1}$$

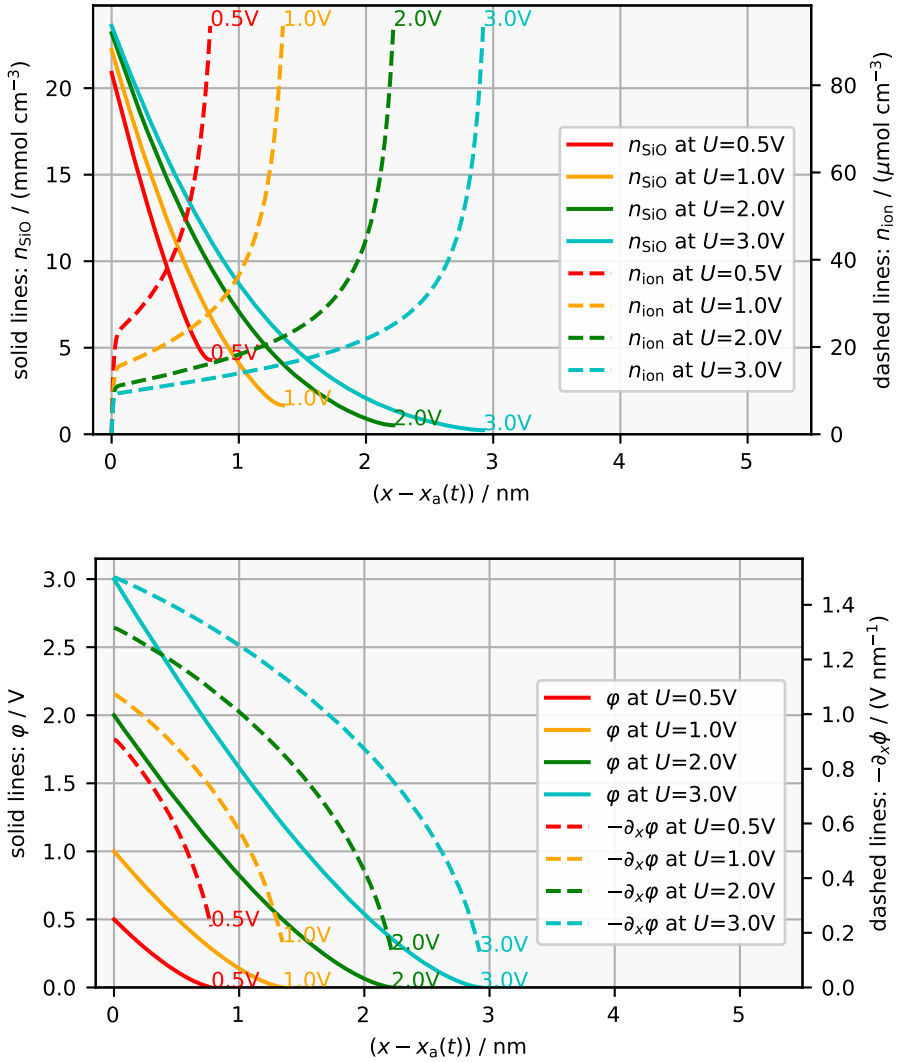

Figure II.4.3: Stationary distributions of several space-dependent quantities are shown at different voltages U. At each voltage U there is a different stationary layer thickness $x_b(t) - x_a(t)$ which is reflected by the respective domain of definition. Top: Stationary concentration of O^{2-} ions $n_{ion}(x,t)$ (dashed line) and of partially oxidized silicon $n_{SiO}(x,t)$ (solid line) for different applied voltages. Bottom: Stationary profile of the corresponding electric potential $\varphi(x,t)$ and the electric field $\partial_x\varphi(x,t)$.

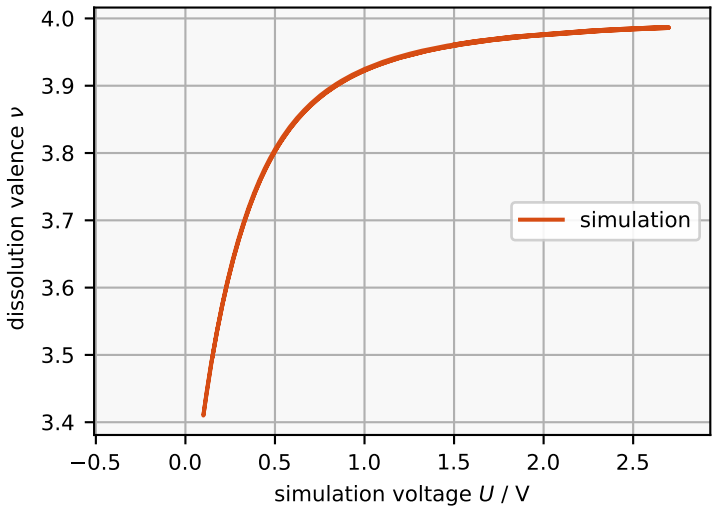

Figure II.4.4: Dissolution valency as defined by Equation (II.4.1) is plotted over the voltage $U(t)$ during simulated cyclic voltammetry using the model described in Chapter II.3 at a scan rate of 1 mV/s, with the parameters in Table II.3.1. As the voltage is increased the valency increases from 3.4 to 4, as reported in the literature [22, 23].

The calculated reaction valence during simulated cyclic voltammetry is shown in Figure II.4.4. Due to the slow scan rate there is no noticeable hysteresis, if there is one at all. The simulated valence increases monotonically with the voltage from a value of about 3.4 close to the current peak to 4 at the plateau where it saturates. The same behavior has been confirmed by gravimetric measurements [22] and by rotating ring disc measurements [7, 23] The exact value of the valence in the limit $U \to 0$ can be adjusted by changing the rate constant of Reaction (R3).

II.4.4 Impedance spectra

To obtain the impedance spectra for our model described in Chap. II.3 we set the parameter U to a different function for each investigated angular frequency ω, denoted by $U_\omega(t)$:

$$U_\omega(t) = 1\,\mathrm{mV} \cdot \sin(\omega\, t) + U_0 \tag{II.4.2}$$

The model Equations were solved for many periods of $U_\omega(t)$ such that the resulting electric current $I_\omega(t)$ converged and became sine-shaped. We calculated the corresponding analytical signals $\widetilde{U}_\omega(t)$ and $\widetilde{I}_\omega(t)$ with the Matlab R2017b function

hilbert(...) [53]. This means that $\widetilde{U}_\omega(t)$ and $\widetilde{I}_\omega(t)$ are obtained by removing from $U_\omega(t)$ and $I_\omega(t)$ by removing the negative and zero frequency components. The impedance $Z_\omega(t)$ is then calculated as

$$Z_\omega(t) = \frac{\widetilde{U}_\omega(t)}{\widetilde{I}_\omega(t)} \tag{II.4.3}$$

which would be constant in time if the current response was perfectly linear. However, even at the small perturbation amplitudes that we chose, the current response is not perfectly linear, so $Z_\omega(t)$ is not perfectly constant. Thus, we determined the value for the impedance Z_ω at a certain angular frequency ω by time-averaging $Z_\omega(t)$ over some periods. Alternatively one could have calculated the impedance from the values of the Fourier transformed signals at ω, which is equivalent for a linear response.

The impedance spectra obtained by the simulation are plotted in Fig. II.4.5 (Top) and Fig. II.4.6 (Top) and the corresponding electrochemically measured impedance spectra in Fig. II.4.5 (Bottom) and Fig. II.4.6 (Bottom). There is an offset in the voltage U which is qualitatively discussed in Chap. II.3, see also the different voltage axes in Fig. II.4.1. In the simulation both semi-circles grow as the voltage is increased, which is also the case in the measured spectra. The measured spectra have a 'kink' which is not found in the simulated spectra. The 'kink' becomes more prominent for larger voltages. The plots in Figure II.4.7 exemplarily compare one simulated impedance spectrum to one measured impedance spectrum. It can be seen that the simulated spectrum looks similar to the measured spectrum around 2 V vs SHE.

The model allows us to assign a physical meaning to some features of the measured impedance spectra which are illustrated in the equivalent circuit in Figure II.4.8. For example, when omitting the charging term $I_{\mathrm{ch}}(t)$ in the numerical calculation (see Equation (II.3.23)), the small semi-circle at high frequencies in the Nyquist plot disappears. Thus, it is clear that the small semi-circle emerges due to interfacial charging, which means that opposing charges accumulate at the $\mathrm{Si/SiO}_x$ interface and at the SiO_x/solution interface. Hence, any equivalent circuit would require a capacitor C_1, see Figure II.4.8.

At an intermediate frequency at which the small and the large semi-circle merge, the impedance is almost perfectly ohmic. This means that this frequency is sufficiently low for the layer capacity to be negligibly small but high enough so that the oxide thickness is not affected. Thus, the impedance at this frequency corresponds to the resistivity of the layer for a fixed thickness. This is represented in the equivalent circuit by a resistor R_1. Since the simulated impedance spectra at low frequencies resemble a semi-circle which ends at a real and negative value when $\omega \to 0$, we fit a capacitor $C_2 \ll C_1$ in parallel with a negative resistance R_2. This approximation seems to be valid for the electrochemically measured impedance spectra in Fig. II.4.5 (bottom) at $U \approx 2$ V vs SHE.

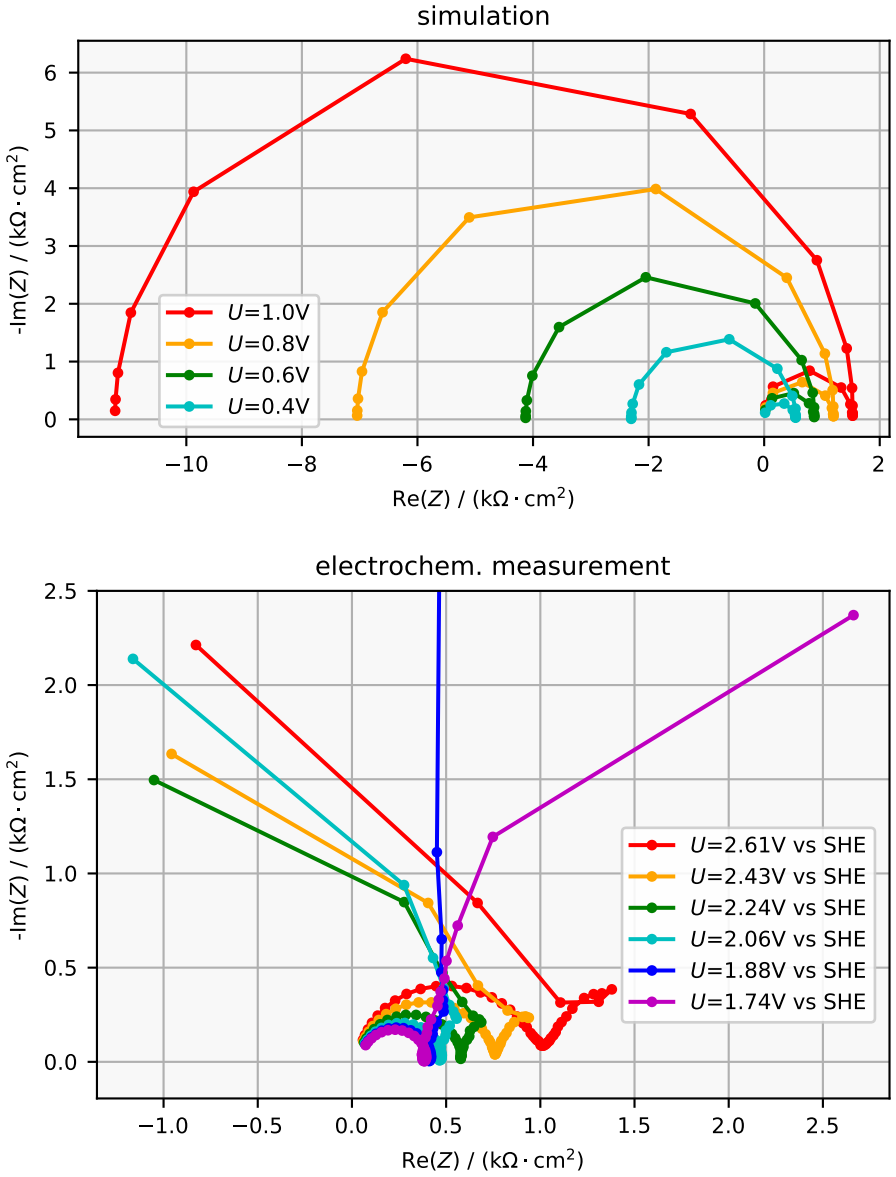

Figure II.4.5: A comparison of the Nyquist plots of simulated and electrochemically measured impedance spectra. (Top): Nyquist plot of impedance spectra from a simulation using the model described in Chapter II.3 with the parameters in Tab. II.3.1. (Bottom): This Nyquist plot of impedance spectra that were measured applying dynamic multi-frequency analysis [54] for (111) p-silicon of 5 to 25 Ω cm in a solution of 0.05 M NH_4F and 0.025 M H_2SO_4 (pH2.3).

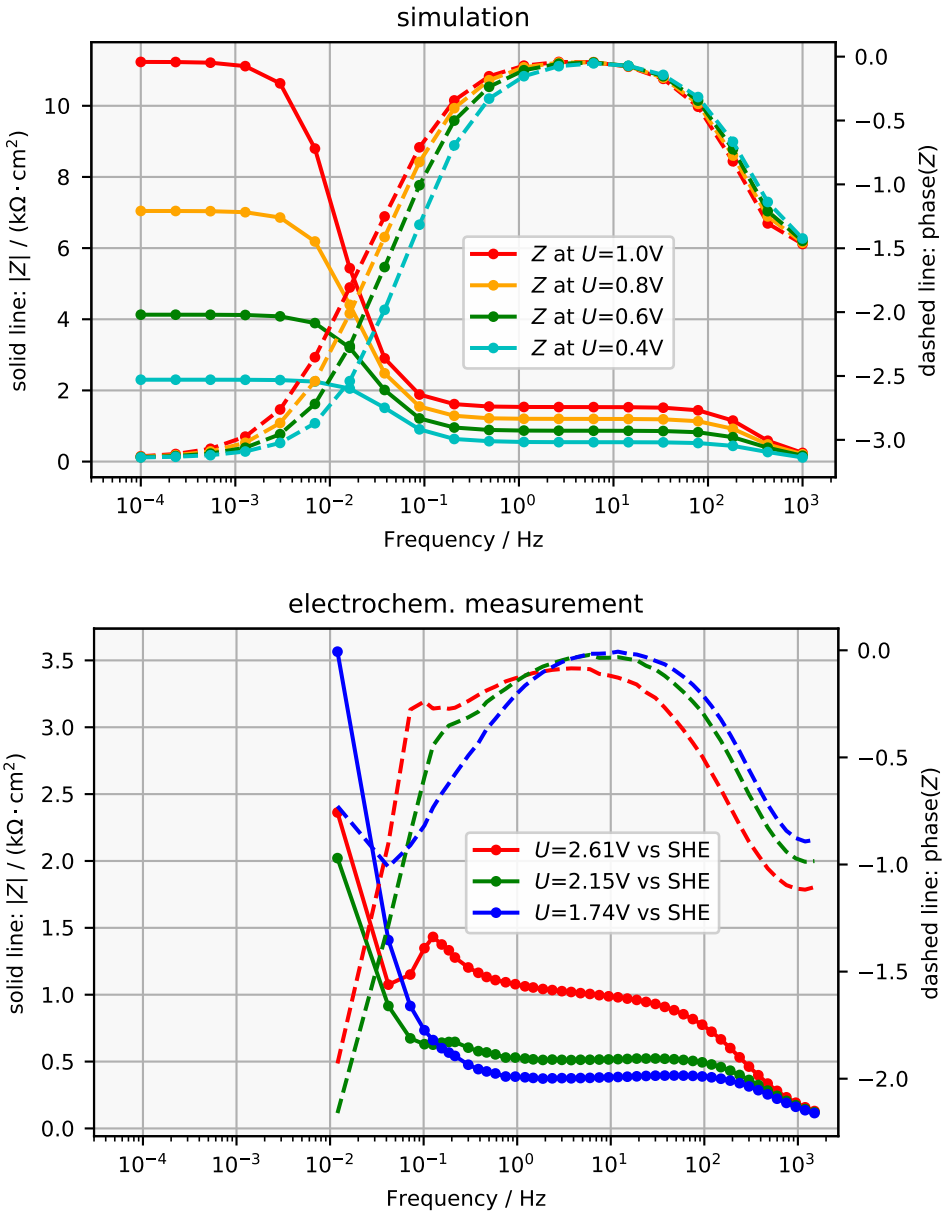

Figure II.4.6: Comparison of Bode plots of the same data as in Figure II.4.5. (Top): Bode plot of the simulated data from Fig. II.4.5. (Bottom): Bode plot of the measured data from Fig. II.4.5.

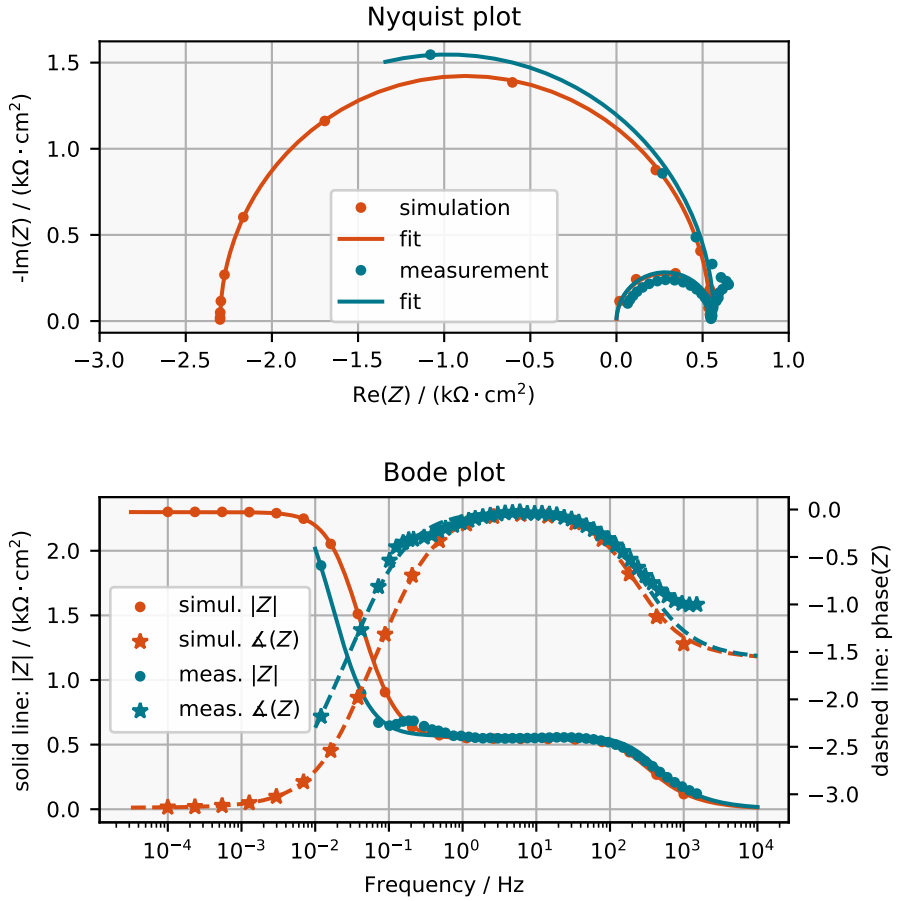

Figure II.4.7: One simulated impedance spectrum at voltage $U = 0.4$V and one measured impedance spectrum at voltage $U = 2.2$V vs SHE are exemplarily compared. Fits are represented by solid lines for the absolute value $|Z|$ and by dashed lines for the complex phase of Z. The equivalent circuit can be seen in Figure II.4.8. The circuits fit the simulated spectrum well but do not reflect all features of the measurement. These features become more dominant at higher voltage, as can be seen in Fig. II.4.5 (bottom).

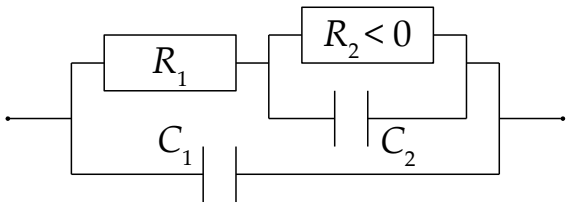

Figure II.4.8: Equivalent circuit fitted to the spectra in Figure II.4.7. It fits the simulated spectra quite well, but for the measured spectra it neglects the 'kink' at around 0.2Hz and it does not describe the complex phase at $\omega \to \infty$.

There are some measurable features that the model does not reproduce. It can be seen in the Bode plot in Fig. II.4.6 (bottom) that at high frequencies the measured spectra approach a phase that differs from $-\pi/2$, where $-\pi/2$ would correspond to an ideal capacitor. This is probably caused by an uncompensated resistance in series, which leads to a complex phase of zero at $\omega \to \infty$.

Another feature in the measured spectra, which is not reflected by the model, is the kink at frequencies between 0.1 Hz and 1 Hz. This kink becomes a loop that grows for higher voltage until at some voltage it possibly causes the resonance that is known to occur in the system [24], by touching the origin in the Nyquist plot. If the impedance becomes zero at a certain frequency, it corresponds to a Hopf-bifurcation [55], which could explain the emergence of oscillations that are observed in the system [7, 33]. However, the loop is not explained by the model and the scenario in the electrochemical set up is probably even more complicated, as can be guessed from earlier impedance measurements at other parameters [24]. Unfortunately, measuring the impedance of the steady state in the resonant regime appears to be challenging, also with dynamic multi-frequency analysis.

A third discrepant feature is measured at smaller anodic voltages. As the voltage is decreased in the electrochemical set up, one eventually passes the current peak and arrives at the electropolishing regime where the differential resistance is positive. Thus, the presumed contact point between the impedance curve and the real axis at zero frequency in the Nyquist plot moves from the left half plane to the right, as for the measured data in Figure **??**. The model, in contrast, is not valid for voltages this low, as there is no oxide layer of relevant thickness.

II.4.5 Origin of the negative differential resistance

From our model we can extract the necessary physical conditions leading to the negative differential resistance. First we note that in order to obtain the negative slope in the current voltage characteristics only the reactions (R0), (R1), (R2), and

(R4) are required. Reaction (R3), in contrast, was only introduced to adjust the valence to above 3 at very small layer thicknesses, where volume Reaction (R2) hardly occurs.

Let us assume that the system is in a steady state on the negative differential branch. An increase in the voltage U leads to an increase in the amount of O^{2-} ions pulled into the oxide layer by reaction (R0) which increases the rate of the first oxidation step (R1), as the latter requires O^{2-} ions. The resulting thickening of the oxide layer works against (R1) because the path that the O^{2-} ions have to travel in order to reach the Si/SiO_x interface becomes longer. Therefore, the thickening of the oxide layer partly compensates the rate increasing effect of the larger voltage U on the first oxidation step (R1). The second oxidation step (R2), however, which happens inside the layer volume, is supported by the thicker layer, or at least it is less suppressed compared to the first oxidation step (R1), which happens at the Si/SiO_x interface. Thus, the oxide layer now contains a higher fraction of fully oxidized silicon, SiO_2, as compared to a smaller applied voltage U. Consequently, the oxide layer is etched more slowly by Reaction (R4). This thickens the oxide layer even further such that the rate increasing effect of the larger voltage U on the first step (R1) is overcompensated.

Note that without considering reaction (R2), any increase in voltage is compensated by a thicker oxide layer in such a way that the electric field inside the oxide layer as well as the current remain constant, independently of the ratios or the absolute vales of the rate constants of SiO (R1) and SiO_2 (R3) formation.

In short, the negative differential resistance is the result of the interplay between the further oxidation of partially oxidized SiO_x inside the oxide layer and the dependence of the etch rate on the stoichiometry of the oxide.

Chapter II.5

Summary and outlook

Silicon in hydrofluoric solution under anodic bias is a system that is not only of technological relevance, but also of significant interest in regard of its capabilities to show a wide range of self-organization phenomena. In this part, we have presented a model for this, which is build on principles of non-equilibrium thermodynamics, solid state chemistry and semi-conductors physics. The model captures the behavior qualitatively and semi-quantitatively with minimal complexity. It was possible to reproduce a wide range of measurements, assuming that the reaction is mainly limited by the migration of ions in the oxide layer. Hence, we neglected the dependence of electrochemical reaction rates on the electrochemical potential. We also discussed that we can neglect temporal variations of the potential drops across the space charge layer and the Helmholtz layer because of their large capacities. In contrast, a very crucial element for reproducing the negative-differential resistance is the oxidation of SiO_x within the oxide layer, and the dependence of the etch rate on the oxide stoichiometry. Our simulations reproduced the current-voltage curve in the voltage regime of negative differential resistance below the resonant current-plateau, and the monotone dependence of the valency and the oxide-layer thickness on the applied voltage. Moreover, the simulations reproduce measured impedance spectra.

This presented model is a basis on which one can build to further uncover non-linear features of the Si electrodissolution dynamics, such as current oscillations or the patterns observed with n-type Si electrodes. For this, it is likely that some of the simplifying assumptions entering the model have to be relaxed.

Part III

Modeling of CO Electrooxidation on Globally Coupled Pt Microelectrodes

Chapter III.1

Motivation

In the Part II we considered a model for how silicon is electrochemically dissolved in hydrofluoric acid under anodic bias. Our motivation had been the interesting dynamical phenomena in the system. We presented a model that could reproduce a wide range of measurements, but its ability to capture the complex dynamics of the system was sill quite limited. In this part, we deal with a completely different situation, regarding not only the considered material, but also the state of the art in its modeling – the electrooxidation of CO on platinum. In particular, we want to investigate the dynamics of an array of several platinum microelectrodes that are short circuited. The physics of the CO electrooxidation on platinum is well known and its dynamics can be well reproduced by models. The motivation here is to explain the behavior of the models, and to carve out the general principles for the selforganization that we see, in particular, oscillations of globally coupled, bistable components.

Usually, collective oscillations are found in systems that consist coupled oscillators. The coupling between the oscillators can make them synchronize in phase and frequency [56]. This scenario is found in nearly any field of natural science. Notable examples range from mechanical clocks, over arrays of Josephson junctions, chemical and electrochemical systems to swarm behavior and pedestrian dynamics. Besides completely uniform oscillations, there is a variety of synchronization patterns that form spontaneously in many coupling topologies [57–60]. Among these are cluster patterns, which consist of multiple synchronized groups of oscillators [61–63]. In contrast to coupled oscillators, coupled bistable components are studied sparsely. Kouvaris and colleagues showed that networks of bistable, diffusively coupled elements with global feedback may form localized stationary patterns [64]. In this part, we explain how coupled bistable components can also exhibit collective cluster oscillations. More precisely, the coupled bistable components may spontaneously form two or three groups that exhibit synchronous oscillations although the basic component is neither oscillatory or resonant itself.

Bistability of stationary states is a very basic nonlinear behavior that non-linear dynamical systems can show. A technologically relevant example for globally coupled bistable components are catalyst particles on a common support where

the catalytic reaction exhibits bistable kinetics [65]. Another example is an array of micro-electrodes which are coupled through an external circuit and possess an N- or an S-shaped current voltage characteristic [66, 67]. In this case, even the dynamics of the individual components can be accessed experimentally. Furthermore, Li-ion batteries which composed of many individually chargeable nanoparticles embedded in a common matrix material fall into this category[68–71]. The chargeable nanoparticles in this case are bistable within a certain range of potential, being either in a Li-rich or in a Li-poor phase. A related, illustrative example are rubber balloons, each one being attached to one of many openings of a pipe and the entire system being 'charged' with air [69, 72, 73]. Note, however, that despite the mentioned strong similarities, the comparison between the latter two systems, which do not dissipate energy, and the dissipative systems considered here should be seen with caution.

The interesting behavior in ensembles of bistable components arises when they are operated under a global constraint. Without loss of generality, this can be exemplified with the CO electrooxidation on an array of microelectrodes. The microelectrodes are the components and we couple them by fixing the total electrical current through them. The dynamics of an individual component k depend on an inner state variable x_k that is bistable in some region of the applied voltage u (Fig. III.1.1a). The current y_k through the component depends on the inner state x_k such that the y_k-u curve inherits the bistability from x_k. We use the symbol y for the current instead of the more common symbol i throughout this part to avoid ambiguity with the imaginary unit. The poisition of the steady states in the y_k-u diagram does not depend on whether one controls the current y_k or the voltage u, but the stability does. While a single, individual component is monostable under y_k control, it is bistable under u control, the middle autocatalytic branch being unstable (Fig III.1.1a, b). An entire ensemble of bistable components corresponds to an equivalent circuit as in Fig. III.1.1c, where all the components are connected in parallel. While the components are effectively decoupled under u control, under y_{tot} control, i.e. a fixed the sum of the individual currents y_k in case of the Pt microelectrodes, the behavior is much more interesting and is the topic of this part of the thesis. Remember that Fig. III.1.1 can also represent non-electrical systems like the rubber balloons that are attached to a common pipe, in which case u would be the pressure in the pipe and y_k would be the air in the k-th rubber balloon. For the Li nanoparticles u is the voltage and y. Still we will continue to use the Pt microelectrodes as the main example.

One well known response of such a system upon a slow ramp of the total current y_{tot} (or total charge in the case of the Li-ion batteries or the rubber balloons) is the sequential activation of the individual components [66–69]. Starting from an initial condition where all elements are in the low-current state, one element after the other will switch to the high current branch, as shown in Fig. III.1.2. This sequential

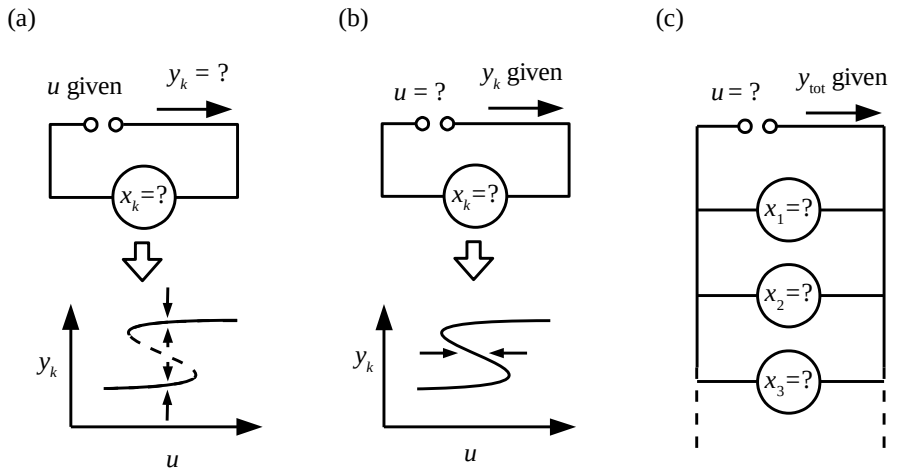

Figure III.1.1: A circuit representation of the system. (a): A single bistable component under u control, i.e. a fixed electrode potential in case of a Pt microelectrode. y_k and x_k adjust accordingly (b): A single bistable component under y_k control, i.e. a fixed electrode current in case of a Pt microelectrode. u and x_k adjust accordingly. (c): Globally coupled, bistable components.

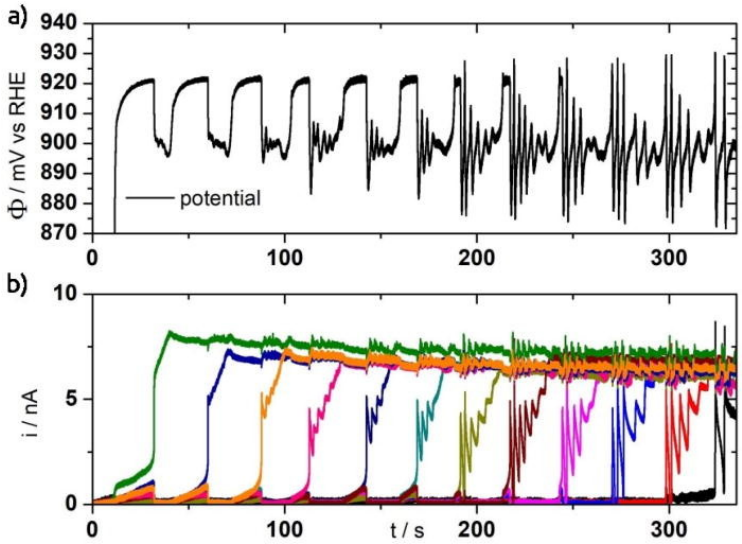

Figure III.1.2: Oscillations in an array of 12 parallelly connected Pt microelectrodes in CO saturated 0.5 mM sulfuric acid during a galvanodynamic scan of 203 pA s^{-1}, (a): Electric potential over time. (b): Individual currents over time. Reproduced from [74], with the permission of AIP Publishing.

activation was coined mosaic instability in the case of first-order phase transition systems [70, 75]. There is also another phenomenon that has been observed CO electrooxidation on an array of Pt micro-electrodes, which has not been observed in the other mentioned systems. The emergence of collective oscillations from the third activation on. These oscillations even persist if the total current y_{tot} is kept constant to the degree that the experimental parameters can be kept constant, as shown in Fig. III.1.3 [74]. Here, each oscillatory state is characterized by one electrode on the autocatalytic state, the other eleven electrodes being distributed on the high and low current states. The measured oscillations could be reproduced with a mathematical model capturing the electrochemical kinetics of the system. However, for large numbers of components, oscillatory solutions have not been reported. In this part of the thesis, we demonstrate that bistable multi-component systems can exhibit oscillations even for an arbitrarily large number of components.

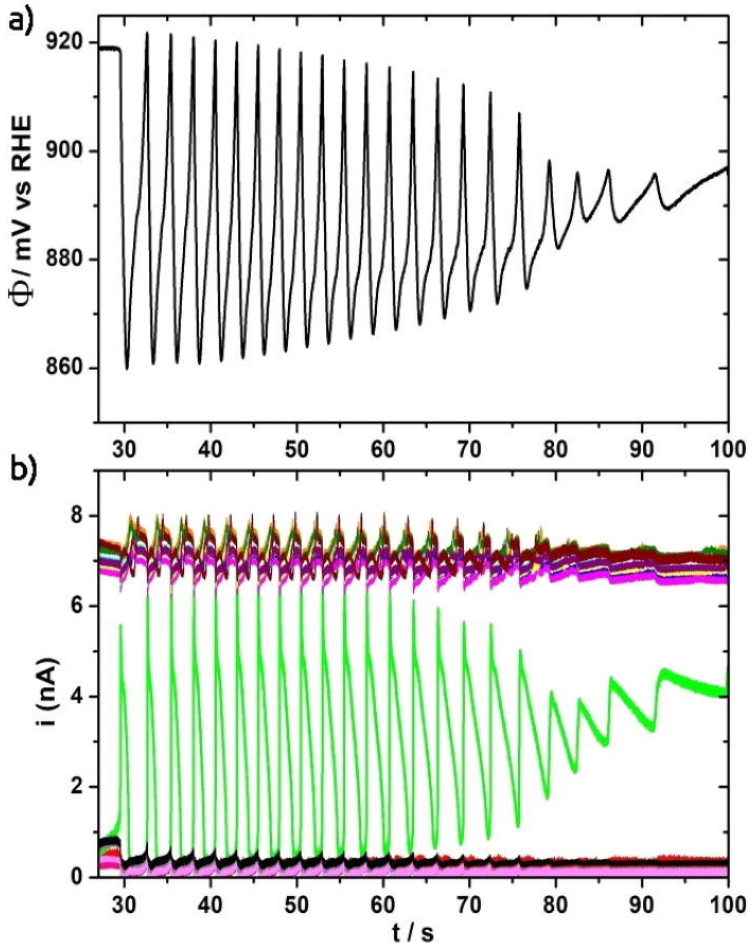

Figure III.1.3: Potential (a) and individual current (b) time series for a current of 60 nA applied to twelve short-circuited microelectrodes in CO saturated 0.5 mM sulfuric acid. Reproduced from [74], with the permission of AIP Publishing.

Chapter III.2

Review: Phase transitions

The bistable reaction kinetics on Pt microelectrodes described in this part of the thesis are very similar to systems that have a first-order phasetransition. In this chapter, we review phase transitions in a way that makes it easy to compare the two.

In order to treat phase transitions, it is not sufficient to describe a thermodynamic system only in terms of the common thermodynamic quantities S, T, V, p, N, μ. In particular, one needs to introduce an order parameter x that captures the particle structuring and can, thus, distinguish between e.g. a solid and a liquid phase.

III.2.1 Homogeneous

Let us start from the beginning and define the entropy S of a system in terms of the phase volume Γ, the total energy E, the volume V, the number of particles N, and the order parameter x and let us denote the Boltzmann constant by k_b.

$$S(x, E, V, N) = k_\mathrm{b} \ln(\Gamma(x, E, V, N)) \tag{III.2.1}$$

The first law of thermodynamics reads

$$\begin{aligned} \mathrm{d}E = &\left(\frac{\partial S}{\partial E}\right)^{-1} \frac{\partial S}{\partial x}\,\mathrm{d}x \; - \left(\frac{\partial S}{\partial E}\right)^{-1} \mathrm{d}S \; + \left(\frac{\partial S}{\partial E}\right)^{-1} \frac{\partial S}{\partial V}\,\mathrm{d}V \; + \left(\frac{\partial S}{\partial E}\right)^{-1} \frac{\partial S}{\partial N}\,\mathrm{d}N \\ =: &\; \xi(x, E, V, N)\mathrm{d}x \; + T(x, E, V, N)\mathrm{d}S \; - p(x, E, V, N)\mathrm{d}V \; + \mu(x, E, V, N)\mathrm{d}N \end{aligned} \tag{III.2.2}$$

in which T, p, μ are the temperature, the pressure, and the chemical potential, respectively. The function ξ does not have a specific name but we can think of it as a "order-parameter potential" that describes the change in energy per change in order parameter, analogously to the chemical potential, which describes the change in energy per change in particle count. For our purposes we can keep V and N constant, so the system reduces to:

$$S(x, E) = k_\mathrm{b} \ln(\Gamma(x, E)) \tag{III.2.3}$$

$$\mathrm{d}E = \xi(x, E)\mathrm{d}x + T(x, E)\mathrm{d}S \tag{III.2.4}$$

For an isolated system, in which E is kept constant, order parameter might evolve according to:

$$\frac{\mathrm{d}}{\mathrm{d}t}x(t) = \tilde{f}(x(t), E) \tag{III.2.5}$$

$$T = \tilde{g}(x(t), E) \tag{III.2.6}$$

in which t is the time, $\tilde{g}(x(t), E) = -\left(\partial S(x(t), E)/\partial E\right)^{-1}$, and $\tilde{f}$ is a function that fulfills a strong formulation of the second law of thermodynamics, i.e. $\forall E \forall x : \left(\partial S(x, E)/\partial x\right) \tilde{f}(x, E) \geq 0$. The $\tilde{f}$-$\tilde{g}$ notation is used to make it easier to see the link between the phase transitions we consider here and bistable systems like Pt microelectrodes, which are the main topic of interest in this part of the thesis.

If instead of isolating the system we keep its temperature T fixed using a thermal reservoir, the dynamics change to:

$$\frac{\mathrm{d}}{\mathrm{d}t}x(t) = f(x(t), T) \tag{III.2.7}$$

$$E = g(x(t), T) \tag{III.2.8}$$

Here, f is a function that, just as $\tilde{f}$ above, fulfills a strong formulation of the second law of thermodynamics. Since we fix T, V, N, this means $\forall T \forall x : \left(\partial F(x, T)/\partial x\right) f(x, T) \leq 0$, where $F = E - TS$ is the Helmholtz free energy. Minimizing F maximizes the total entropy of the system and the thermal reservoir. For g it was assumed that $\tilde{g}(x(t), E)$ is invertible in E and that $\forall E \forall x : E = g(x, \tilde{g}(x, E))$. This is not guaranteed since there can be multiple values of E pointing to the same function value of $\tilde{g}(x, E) \equiv T(x(t), E)$. However, such ambiguities can be resolved by introducing more order parameters.

Now we have almost everything we need to describe a phase transitions that occurs under T variation. A phase transition occurs when there there is a bifurcation in Eq.(III.2.7). For a first-order phase-transition it is a saddle node bifurcation, or rather a pair of saddle node bifurcations surrounding a bistable region like in Fig.III.2.1. The two stable equilibria in the bistable region correspond to two phases of a substance, e.g. solid and liquid. For a second-order phase-transition it would be a pitch-fork bifurcation.

III.2.2 Inhomogeneous

In a less idealized scenario, the system is spatially extended and the transition occurs inhomogeneously. One can again chose to isolate the system to keep the total energy constant, or immerse it in a thermal reservoir to keep the temperature constant. With

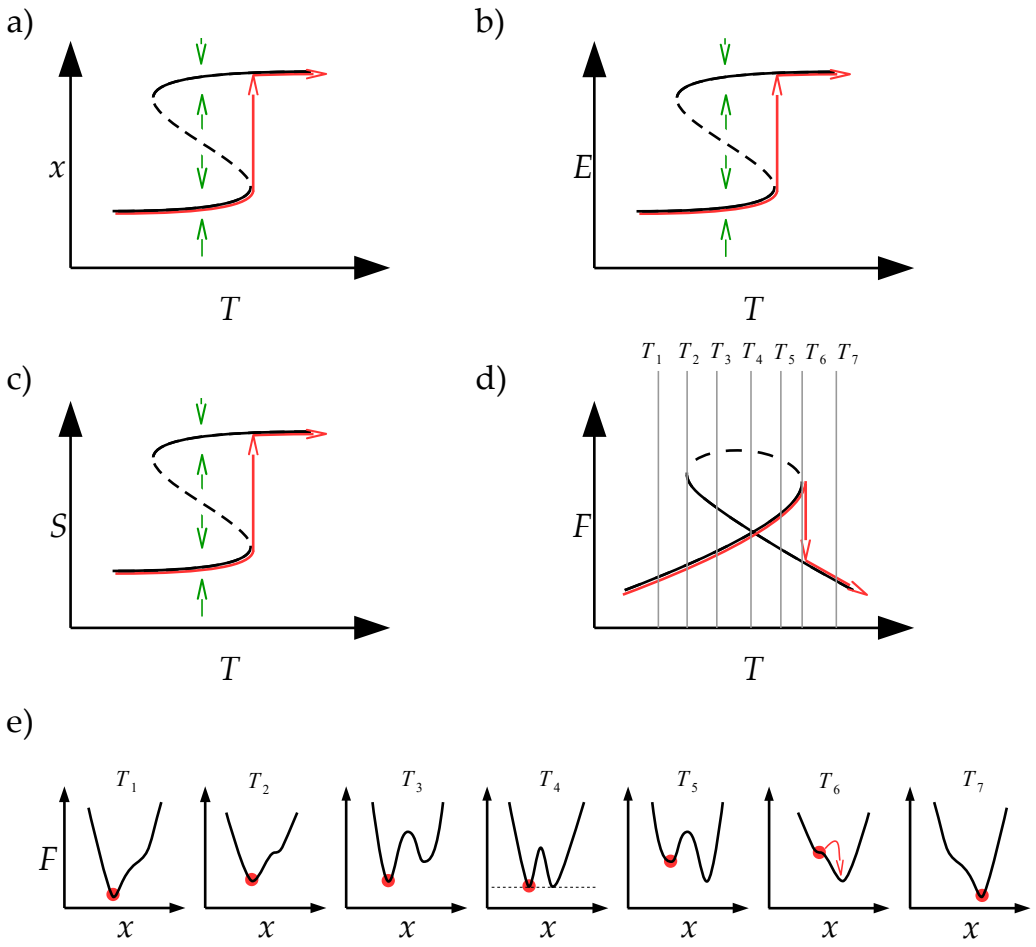

Figure III.2.1: Qualitative sketches of various quantities during an overly idealized first-order phase-transition in a homogeneous system during a slow temperature ramp. (solid black line): Stable equilibrium. (dashed black line): Unstable equilibrium. (red line): System state. (green arrows): flow field (a): Order parameter over temperature. (b): Energy over temperature. (c): Entropy over temperature. (d): Helmholtz free energy over temperature. (e): Helmholtz free energy over order parameter for various temperatures. The red dot indicates the system state.

the temperature as the constant control parameter one obtains an equation like

$$\frac{\mathrm{d}}{\mathrm{d}t}x(r,t) = f(r,t,T) \tag{III.2.9}$$

$$E_{\mathrm{tot}} = \int \mathrm{d}r\; g(x(r,t),T) = \int \mathrm{d}r\; E_{\mathrm{loc}}(r,t) \tag{III.2.10}$$

in which r parameterizes space, E_{tot} is the total energy of the system, E_{loc} is the local energy density. $f(r,t,T)$ ensures that the total free energy F_{tot}, given as a functional of x, decreases with time (second law), i.e.

$$\forall T \forall t : \int \mathrm{d}r\; \frac{\delta F_{\mathrm{tot}}[\lambda r'.x(r',t),T]}{\delta x(r,t)} f(r,t,T) \leq 0. \tag{III.2.11}$$

The λ here is used in the sense of lambda calculus, i.e. $(\lambda r'.x(r',t)) : r \to x(r,t)$. The energy E_{tot} is now an integral over the local energy density $E_{\mathrm{loc}}(r,t)$, but one could also model it as a functional. When defined as an integral, it is more similar to the bistable Pt microelectrodes, because then E_{tot} takes the role that the total current plays for the Pt microelectrodes that are connected in parallel. This is explained in more detail in Chap. III.3. The main difference is the continuity in r instead of discrete components. Analogously, T takes the role that the electrode potential plays for the microelectrodes.

An simple illustrative choice of F_{tot}, f, and g that produces a first-order phase-transition would be

$$F_{\mathrm{tot}}[\lambda r'.x(r',t),T] := \int \mathrm{d}r' \left(\underbrace{-(T-T_0)x(r',t) - \frac{1}{2}x(r',t)^2 + \frac{1}{4}x(r',t)^4}_{F_{\mathrm{loc}}} + \frac{1}{2}(\nabla_{r'}x(r',t))^2 \right) \tag{III.2.12}$$

$$f(r,t,T) := -\frac{\delta F_{\mathrm{tot}}[\lambda r'.x(r',t),T]}{\delta x(r,t)} \tag{III.2.13}$$

$$g(x(r,t),T) := x(r,t) \tag{III.2.14}$$

With this choice Eq.(III.2.11) is fulfilled. So the dynamical system would be:

$$\frac{\mathrm{d}}{\mathrm{d}t}x(r,t) = T - T_0 + x(r,t) - x(r,t)^3 + \nabla_r^2 x(r,t) \tag{III.2.15}$$

$$E_{\mathrm{tot}} = \int \mathrm{d}r'\; x(r',t) \tag{III.2.16}$$

This is an Allen-Cahn-like equation [76] that makes a phase transition at $T = T_0$. For $T = T_0$ the system has two domains, the size of which determines the total energy

E_{tot} (and analogously the total entropy S_{tot}). The energy regime in which a stable equilibrium with such two distinct domains exists is the binodal regime. The part of the binodal regime in which there is no stable homogeneous state is the spinodal regime. Notice that even if derivatives of x with respect to r were to be included in g and in the integral for E_{tot}, their contribution would be small if the total domain size is large (analogously for S_{tot}). The resulting equilibria of Eq.(III.2.15),(III.2.16) and of similar systems are sketched in Fig. III.2.2. Notice that for inhomogeneous systems the transition occurs at a different temperature than in the homogeneous case, namely where the two minima of the local term of F_{loc} have the same value. However, the equilibria of the homogeneous system still exist but are metastable.

In the next chapters, we consider globally coupled bistable components, which are very similar to systems that have a first order phase transition. One individual component behaves analogous to the homogeneous phase transition, but when many of them are globally coupled we see qualitatively different phenomena. The key property that distinguishes the globally coupled bistable components from an inhomogeneous phase transition, which we have just discussed, is the lack of a local coupling between the components. As a result these systems can have much more complicated equilibrium lines and show various interesting dynamical phenomena.

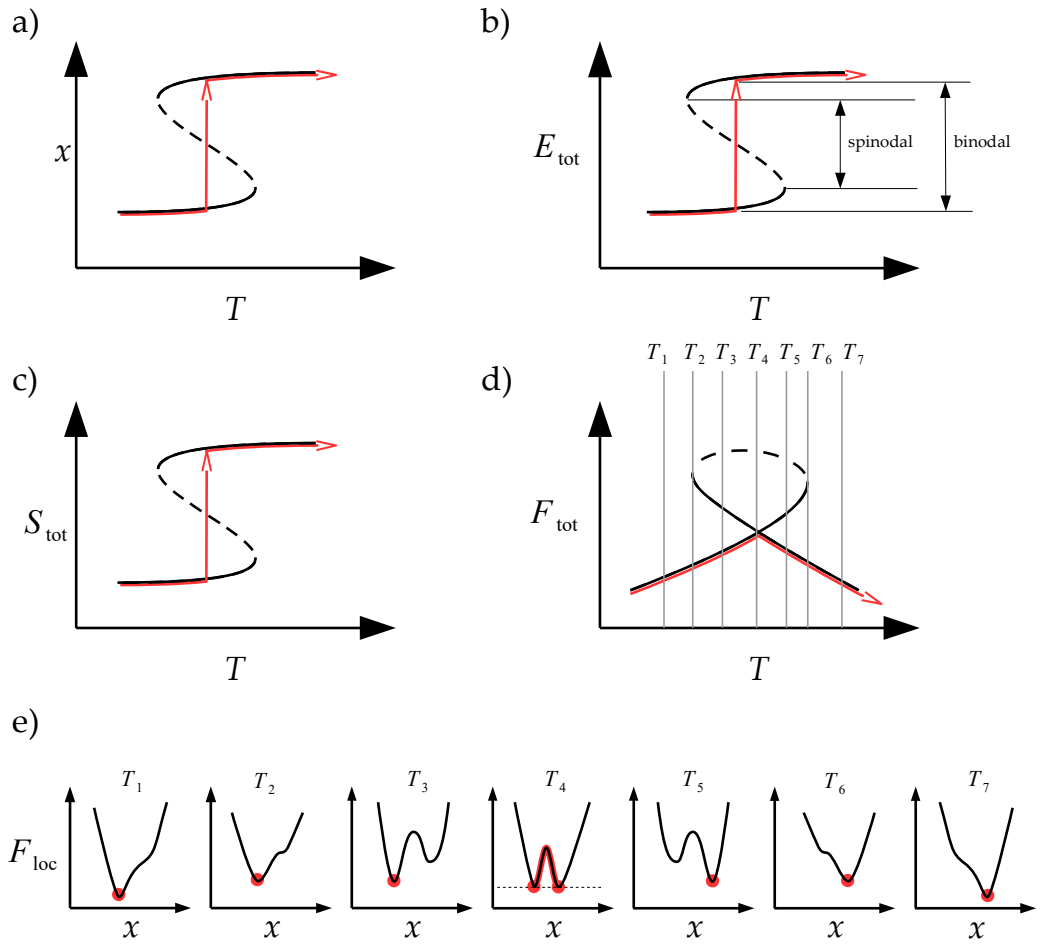

Figure III.2.2: Qualitative sketches of various quantities during an idealized first-order phase-transition in a inhomogeneous system during a slow temperature ramp. (black line): equilibrium. (red line): System state. (a): Order parameter over temperature. (b): Energy over temperature. (c): Entropy over temperature. (d): Helmholtz free energy over temperature. (e): Helmholtz free energy over order parameter for various temperatures. The red dot indicates the system state.

Chapter III.3

General, linear analysis

This chapter deals with the sequential activation and with the voltage oscillations, which both have been observed with arrays of Pt micro-electrodes in CO containing solutions [74]. To explain these phenomena it is sufficient to assume a qualitative S-shape of the current-voltage characteristics, which is an equilibrium curve, and consider the linear regime close to it. Therefore, no dynamical equations are specified in this chapter. For this reason, the statements in this chapter are very general and apply to an entire class of systems, including Pt micro-electrodes under total-current control, rubber balloons under total-air control, or Li_xFePO_4 nano-particles under total-charge control. Despite its generality, the following analysis has been done with mainly Pt microelectrodes in mind, which influenced certain decisions regarding the notation.

III.3.1 Individual components

Let us first consider the individual components that make up the ensemble in Sec. III.3.2. One component represents, for example, an individual Pt micro-electrode, a rubber balloon, or a Li_xFePO_4 nano-particle.

III.3.1.1 System Definition

We assume that we have been given an ordinary differential equation for a bistable, individual component. We further assume that the equation can be written in the following state-space form:

$$\frac{\mathrm{d}}{\mathrm{d}t}x(t) = f(x(t), u) \tag{III.3.1}$$

$$y(t) = g(x(t), u) \tag{III.3.2}$$

We think of $u \in \mathbb{R}$ and $y \in \mathbb{R}$ as voltage and current respectively and of the entries of $x \in \mathbb{R}^n$ as concentrations of n chemical species. Other interpretations could be for example (u: temperature, y: energy, x: order parameter), (u: force, y: momentum, x:

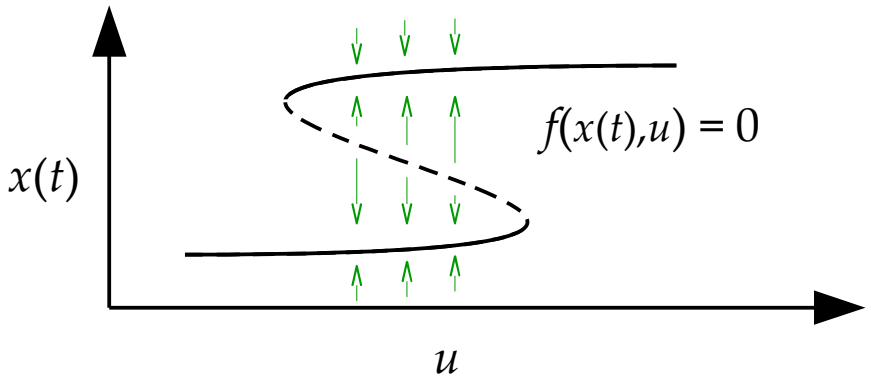

Figure III.3.1: Sketched nullcline of f

velocity/position) or (u: voltage, y: charge, x: extent of reaction). u is the control or input variable and y is the output variable.

We assume that $f : (\mathbb{R}^n, \mathbb{R}) \to \mathbb{R}^n$ is a parameterized flow field of the form depicted in Fig. III.3.1, i.e. for any u Eq. (III.3.1) is bistable or monostable and its nullcline forms an S in the x-u plot. We chose this restriction, so we can later use a simpler notation for the individual branches of the S, but the results can be easily generalized to more complicated shapes of f as well. Let the fixed points of the flow field f be hyperbolic for almost any u. Further, we assume that $g : (\mathbb{R}^n, \mathbb{R}) \to \mathbb{R}$ is strictly monotone in its second argument, so we can define an inverse function $\tilde{g} : (\mathbb{R}^n, \mathbb{R}) \to \mathbb{R}$ and a function $\tilde{f} : (\mathbb{R}^n, \mathbb{R}) \to \mathbb{R}^n$ such that

$$\forall x, u : \qquad \tilde{g}(x, g(x, u)) := u \tag{III.3.3}$$

$$\forall x, y : \qquad \tilde{f}(x, y) := f(x, \tilde{g}(x, y)) \tag{III.3.4}$$

This gives us a conjugated version of the system in which input and output are exchanged:

$$\frac{\mathrm{d}}{\mathrm{d}t} x(t) = \tilde{f}(x(t), y) \tag{III.3.5}$$

$$u(t) = \tilde{g}(x(t), y) \tag{III.3.6}$$

The equilibrium line of a single component is the set $\boldsymbol{E}$:

$$\boldsymbol{E} := \{\ (u, y, x) \mid 0 = f(x, u)\ \wedge\ y = g(x, u)\ \} \tag{III.3.7}$$

The conjugate system yields the same set:

$$\boldsymbol{E} = \{\ (u, y, x) \mid 0 = \tilde{f}(x, y)\ \wedge\ u = \tilde{g}(x, y)\ \} \tag{III.3.8}$$

III.3.1.2 Linearization

Let $(u^{\text{eq}}, y^{\text{eq}}, x^{\text{eq}}) \in \boldsymbol{E}$ be an equilibrium and let the small deviations from that equilibrium be denoted by a circumflex (also known as 'hat'):

$$(\hat{u}(t), \hat{y}(t), \hat{x}(t)) := (u(t) - u^{\text{eq}}, y(t) - y^{\text{eq}}, x(t) - x^{\text{eq}}) \tag{III.3.9}$$

Notice that we now also allow small fluctuations in the parameter u. Equation (III.3.1) and (III.3.2) can then be linearized to

$$\frac{\mathrm{d}}{\mathrm{d}t}\hat{x}(t) = A\hat{x}(t) + B\hat{u}(t) \tag{III.3.10}$$

$$\hat{y}(t) = C\hat{x}(t) + D\hat{u}(t), \tag{III.3.11}$$

with A, B, C, D defined as:

$$A := \left.\frac{\partial f(x,u)}{\partial x}\right|_{\substack{x=x^{\text{eq}} \\ u=u^{\text{eq}}}} \in \mathbb{R}^{n\times n} \tag{III.3.12}$$

$$B := \left.\frac{\partial f(x,u)}{\partial u}\right|_{\substack{x=x^{\text{eq}} \\ u=u^{\text{eq}}}} \in \mathbb{R}^{n\times 1} \tag{III.3.13}$$

$$C := \left.\frac{\partial g(x,u)}{\partial x}\right|_{\substack{x=x^{\text{eq}} \\ u=u^{\text{eq}}}} \in \mathbb{R}^{1\times n} \tag{III.3.14}$$

$$D := \left.\frac{\partial g(x,u)}{\partial u}\right|_{\substack{x=x^{\text{eq}} \\ u=u^{\text{eq}}}} \in \mathbb{R}^{1\times 1} \tag{III.3.15}$$

Analogously,

$$\tilde{A} := \left.\frac{\partial \tilde{f}(x,y)}{\partial x}\right|_{\substack{x=x^{\text{eq}} \\ y=y^{\text{eq}}}} \in \mathbb{R}^{n\times n} \tag{III.3.16}$$

$$\tilde{B} := \left.\frac{\partial \tilde{f}(x,y)}{\partial y}\right|_{\substack{x=x^{\text{eq}} \\ y=y^{\text{eq}}}} \in \mathbb{R}^{n\times 1} \tag{III.3.17}$$

$$\tilde{C} := \left.\frac{\partial \tilde{g}(x,y)}{\partial x}\right|_{\substack{x=x^{\text{eq}} \\ y=y^{\text{eq}}}} \in \mathbb{R}^{1\times n} \tag{III.3.18}$$

$$\tilde{D} := \left.\frac{\partial \tilde{g}(x,y)}{\partial y}\right|_{\substack{x=x^{\text{eq}} \\ y=y^{\text{eq}}}} \in \mathbb{R}^{1\times 1} \tag{III.3.19}$$

yields

$$\frac{\mathrm{d}}{\mathrm{d}t}\hat{x}(t) = \tilde{A}\hat{x}(t) + \tilde{B}\hat{y}(t) \quad = (A - BD^{-1}C)\hat{x}(t) + BD^{-1}\hat{y}(t) \tag{III.3.20}$$

$$\hat{u}(t) = \tilde{C}\hat{x}(t) + \tilde{D}\hat{y}(t) \quad = -D^{-1}C\hat{x}(t) + D^{-1}\hat{y}(t) \tag{III.3.21}$$

To derive the latter, solve Eq. (III.3.11) for $\hat{u}(t)$ to get Eq. (III.3.21) and then eliminate $\hat{u}(t)$ in eq. III.3.10 to get eq. III.3.20. Notice that the Jacobians A and $\tilde{A}$ at $(u^{\text{eq}}, y^{\text{eq}}, x^{\text{eq}})$ differ, describing the voltage controlled case and the current controlled case, respectively.

III.3.1.3 Saddle-node bifurcation of a *voltage*-controlled component

Assume that at some $(u^{\text{sn}}, y^{\text{sn}}, x^{\text{sn}}) \in \boldsymbol{E}$ the voltage-controlled system III.3.1, III.3.2 has a saddle-node bifurcation [77], which is the "least degenerate" critical point. This means that one single eigenvalue of the Jacobian $A = \left.\frac{\partial f(x,u)}{\partial x}\right|_{\substack{x=x^{\text{sn}} \\ u=u^{\text{sn}}}} \in \mathbb{R}^{n\times n}$ equals zero. Let $v \in \mathbb{R}^{n\times 1}$ be the corresponding eigenvector, so $Av = 0$, and let $w \in \mathbb{R}^{1\times n}$ be the adjoint null-vector, so $wA = 0$ and $wv = 1$. Furthermore, the following non-degeneracy conditions are assumed:

$$\left.\frac{\mathrm{d}^2}{\mathrm{d}\xi^2} w f(\xi v + x^{\text{sn}}, u^{\text{sn}})\right|_{\xi=0} := 2\alpha \neq 0 \tag{III.3.22}$$

$$\left.\frac{\mathrm{d}}{\mathrm{d}\hat{u}} f(x^{\text{sn}}, \hat{u} + u^{\text{sn}})\right|_{\hat{u}=0} := \beta \neq 0 \tag{III.3.23}$$

$$\left.\frac{\mathrm{d}}{\mathrm{d}\xi} g(\xi v + x^{\text{sn}}, u^{\text{sn}})\right|_{\xi=0} := \gamma \neq 0 \tag{III.3.24}$$

$$\tag{III.3.25}$$

Close to $(u^{\text{sn}}, y^{\text{sn}}, x^{\text{sn}})$, we can reduce our $\hat{x}(t) \equiv x(t) - x^{\text{sn}}$ to a projection of $\hat{x}(t)$ into the one-dimensional center-space. Let us call it $\hat{\xi}(t)$. We then get Eqs. (III.3.26), (III.3.27). (If α, β or γ actually happened to be equal to zero we suggest to investigate an "arbitrarily similar" system, in which this it not the case).

$$\frac{\mathrm{d}}{\mathrm{d}t}\hat{\xi}(t) = \alpha\,\hat{\xi}^2(t) + \beta\,\hat{u}(t) \tag{III.3.26}$$

$$\hat{y}(t) = \gamma\,\hat{\xi}(t) + D\,\hat{u}(t) \tag{III.3.27}$$

Setting $\frac{\mathrm{d}}{\mathrm{d}t}\hat{\xi}(t) = 0$ and eliminating $\hat{\xi}(t)$ we get the steady state line in the vicinity of $(u^{\text{sn}}, y^{\text{sn}}, x^{\text{sn}})$:

$$\hat{y}^{\text{eq}} = \pm\gamma\sqrt{-\frac{\beta\hat{u}^{\text{eq}}}{\alpha}} + D\hat{u}^{\text{eq}} \tag{III.3.28}$$

$(\hat{u}^{\text{eq}}, \hat{y}^{\text{eq}}, \hat{x}^{\text{eq}})$ denotes equilibria of $(\hat{u}(t), \hat{y}(t), \hat{x}(t)) := (u(t) - u^{\text{sn}}, y(t) - y^{\text{sn}}, x(t) - x^{\text{sn}})$. Notice that Eq. (III.3.28) describes a turning point in the steady-state line, with two solutions for $\hat{u}^{\text{eq}} < 0$ and none for $\hat{u}^{\text{eq}} > 0$ or vice versa, depending on the signs of α and β.

For any u^{eq} there are by definition at most three equilibria. We name these three groups by the letters "a", "m", "p". "a" stands for the "active" equilibrium where the current is the largest, "m" for the "middle" equilibrium which is unstable under voltage control, and "p" for "passive", where the current is the lowest. The current in the "passive" state of the original experiment [74] is close to zero, thus the name "passive".

The points at which the "a"- and the "m"-branch or the "m"-and the "p"-branch meet are just the turning points we just described in Eq. (III.3.28).

III.3.2 Ensemble

III.3.2.1 Ensemble definition

Instead of one single component following Eq. (III.3.1) and (III.3.2), we now assume N identical components. So $\forall i \in \{1, \ldots, N\}$:

$$\frac{\mathrm{d}}{\mathrm{d}t} x_i(t) = f(x_i(t), u_i(t)) \tag{III.3.29}$$

$$y_i(t) = g(x_i(t), u_i(t)) \tag{III.3.30}$$

To couple the components, we introduce the total curent $y_{\mathrm{tot}}(t)$ and the common voltage $u(t)$, as sketched in Fig. III.1.1c :

$$\sum_{i=1}^{N} y_i(t) = y_{\mathrm{tot}} \tag{III.3.31}$$

$$\forall i \in \{1, \ldots, N\} : u_i(t) = u(t) \tag{III.3.32}$$

The total current y_{tot} acts as a control-parameter, which is prescribed by an experimenter, while $u(t)$ adjusts itself in a consistent way. For the (u: voltage, y: current, x: concentrations)-interpretation, our global coupling corresponds to a parallel connection of the individual components. However, a global coupling like in Eq. (III.3.31), (III.3.32) occurs in other physical contexts, too: In the (u: temperature, y: energy, x: order parameters)-interpretation the components are thermally coupled to each other (Eq. (III.3.32)), but isolated from the environment (Eq. (III.3.31)). In the (u: displacement, y: momentum, x: velocity/position)-interpretation it can be an ensemble of pendulums on a floating raft.

The equilibrium line of an ensemble of N components can be plotted as the set $\boldsymbol{E}_N$:

$$\mathbf{E}_N := \left\{ \left(u, y_{\mathrm{tot}}, \begin{pmatrix} x_1 \\ \vdots \\ x_N \end{pmatrix} \right) \;\middle|\; [\forall i \in \{1, \ldots, N\} : 0 = f(x_i, u)] \;\wedge\; y_{\mathrm{tot}} = \sum_{i=1}^{N} g(x_i, u) \right\}, \tag{III.3.33}$$

which is the same as

$$\mathbf{E}_N := \left\{ \left(u, y_{\text{tot}}, \begin{pmatrix} x_1 \\ \vdots \\ x_N \end{pmatrix} \right) \;\middle|\; \left[\forall i \in \{1,\ldots,N\} : 0 = \tilde{f}(x_i, \underbrace{g(x_i,u)}_{y_i}) \right] \wedge y_{\text{tot}} = \sum_{i=1}^{N} \underbrace{g(x_i,u)}_{y_i} \right\} \tag{III.3.34}$$

Notice that in an ensemble equilibrium all the individual components are in individual equilibria, i.e.:

$$\left(u, y_{\text{tot}}, \begin{pmatrix} x_1 \\ \vdots \\ x_N \end{pmatrix} \right) \in \mathbf{E}_N \quad \Rightarrow \quad \forall i \in \{1,\ldots,N\} : \left(\underbrace{u}_{u_i}, \underbrace{g(x_i,u)}_{y_i}, x_i \right) \in \mathbf{E} \tag{III.3.35}$$

III.3.3 Comparison with first-order phase-transitions

Let us compare Eqs.(III.3.29), (III.3.30), (III.3.31) (III.3.32) with Eqs. (III.2.9), (III.2.10), which describe a first order phase transition. We see, that the two systems are very similar because both have a control parameter u or T in the flow-field function f for a state variable x, and an output variable y_{tot} or E_{tot}, which is obtained by summing or integrating over a function g of x. For both systems, f is a bistable flow field in case of homogeneous x. However, even for large numbers of components the equilibria of the two systems are quite distinct. This is because for phase transitions there is a local coupling (diffusion in the example) which is not present for the microelectrodes. Thus, for phase transitions, the equilibria lie on the Maxwell line (see Fig.III.2.2) while for the globally coupled microelectrodes the equilibria are much more complicated. If instead of microelectrodes we looked at a single macroscopic Pt electrode with CO surface-diffusion, the mathematical description would be identical to that of a first order phase transition. I this case, the two concepts have converged.

III.3.3.1 Linearization

Let group "a", i.e. the group on branch "a", contain $N_{\text{a}} \in \mathbb{N}_0$ of the members of all the N components and let $\hat{X}_{\text{a}}(t) \in \mathbb{R}^{N_{\text{a}}n\times 1}$ be the column-vector that is obtained by stacking all the $\hat{x}_i(t) \in \mathbb{R}^{n\times 1}$, for i indexing the members of group "a". Furthermore, let $A \equiv \frac{\partial f}{\partial x}, B \equiv \frac{\partial f}{\partial u}, C \equiv \frac{\partial g}{\partial x}, D \equiv \frac{\partial g}{\partial u}$ at the equilibrium of group "a" be denoted by $A_{\text{a}} \in \mathbb{R}^{n\times n}, B_{\text{a}} \in \mathbb{R}^{n\times 1}, C_{\text{a}} \in \mathbb{R}^{1\times n}, D_{\text{a}} \in \mathbb{R}^{1\times 1}$, respectively. Let quantities with subscripts "m" and "p" be defined analogously. Let $\mathbb{I}_k \in \mathbb{R}^{k\times k}$ be the identity matrix, let $\mathbf{0}^{j\times k}, \mathbf{1}^{j\times k} \in \mathbb{R}^{j\times k}$ be matrices of only zeros and only ones, respectively, and let $\otimes : (\mathbb{R}^{a\times b}, \mathbb{R}^{c\times d}) \to \mathbb{R}^{ac\times bd}$ denote the Kronecker product. Then, using the

abbreviations $\hat{\mathbf{X}}(t)$, $\mathbf{A}$, $\mathbf{B}$, $\mathbf{C}$, $\mathbf{D}$ defined below, the linearization of the entire ensemble around its equilibrium takes the form:

$$\frac{\mathrm{d}}{\mathrm{d}t}\hat{\mathbf{X}}(t) = \mathbf{A}\hat{\mathbf{X}}(t) + \mathbf{B}\hat{u}(t) \tag{III.3.36}$$

$$\hat{y}_{\mathrm{tot}}(t) = \mathbf{C}\hat{\mathbf{X}}(t) + \mathbf{D}\hat{u}(t) \tag{III.3.37}$$

with

$$\hat{\mathbf{X}}(t) := \begin{pmatrix} \hat{X}_{\mathrm{a}}(t) \\ \hat{X}_{\mathrm{m}}(t) \\ \hat{X}_{\mathrm{p}}(t) \end{pmatrix} \in \mathbb{R}^{(N_{\mathrm{a}}+N_{\mathrm{m}}+N_{\mathrm{p}})n\times 1} \tag{III.3.38}$$

$$\mathbf{A} := \begin{pmatrix} \mathbb{I}_{N_{\mathrm{a}}} \otimes A_{\mathrm{a}} & & \\ & \mathbb{I}_{N_{\mathrm{m}}} \otimes A_{\mathrm{m}} & \\ & & \mathbb{I}_{N_{\mathrm{p}}} \otimes A_{\mathrm{p}} \end{pmatrix} \in \mathbb{R}^{Nn\times Nn} \tag{III.3.39}$$

$$\mathbf{B} := \begin{pmatrix} \mathbf{1}^{N_{\mathrm{a}}\times 1} \otimes B_{\mathrm{a}} \\ \mathbf{1}^{N_{\mathrm{m}}\times 1} \otimes B_{\mathrm{m}} \\ \mathbf{1}^{N_{\mathrm{p}}\times 1} \otimes B_{\mathrm{p}} \end{pmatrix} \in \mathbb{R}^{Nn\times 1} \tag{III.3.40}$$

$$\begin{aligned} \mathbf{C} &:= \underbrace{\mathbf{1}^{1\times N}}_{\text{sum in Eq. (III.3.31)}} \underbrace{\begin{pmatrix} \mathbb{I}_{N_{\mathrm{a}}} \otimes C_{\mathrm{a}} & & \\ & \mathbb{I}_{N_{\mathrm{m}}} \otimes C_{\mathrm{m}} & \\ & & \mathbb{I}_{N_{\mathrm{p}}} \otimes C_{\mathrm{p}} \end{pmatrix}}_{\in \mathbb{R}^{N\times Nn}} \\ &= (\mathbf{1}^{1\times N_{\mathrm{a}}} \otimes C_{\mathrm{a}},\ \mathbf{1}^{1\times N_{\mathrm{m}}} \otimes C_{\mathrm{m}},\ \mathbf{1}^{1\times N_{\mathrm{p}}} \otimes C_{\mathrm{p}}) \\ &\in \mathbb{R}^{1\times Nn} \end{aligned} \tag{III.3.41}$$

$$\begin{aligned} \mathbf{D} &:= \underbrace{\mathbf{1}^{1\times N}}_{\text{sum in Eq. (III.3.31)}} \begin{pmatrix} \mathbf{1}^{N_{\mathrm{a}}\times 1} \otimes D_{\mathrm{a}} \\ \mathbf{1}^{N_{\mathrm{m}}\times 1} \otimes D_{\mathrm{m}} \\ \mathbf{1}^{N_{\mathrm{p}}\times 1} \otimes D_{\mathrm{p}} \end{pmatrix} \\ &= N_{\mathrm{a}}D_{\mathrm{a}} + N_{\mathrm{m}}D_{\mathrm{m}} + N_{\mathrm{p}}D_{\mathrm{p}} \\ &\in \mathbb{R}^{1\times 1} \end{aligned} \tag{III.3.42}$$

Analogously to Eq. (III.3.20) and (III.3.21), the following conjugated system with the current $y_{\mathrm{tot}}(t)$ as the control parameter is obtained by solving Eq. (III.3.37) for $\hat{u}(t)$ and eliminating it in Eq. (III.3.36):

$$\frac{\mathrm{d}}{\mathrm{d}t}\hat{\mathbf{X}}(t) = \tilde{\mathbf{A}}\hat{\mathbf{X}}(t) + \tilde{\mathbf{B}}\hat{y}_{\mathrm{tot}}(t) \quad = (\mathbf{A} - \mathbf{B}\mathbf{D}^{-1}\mathbf{C})\hat{\mathbf{X}}(t) + \mathbf{B}\mathbf{D}^{-1}\hat{y}_{\mathrm{tot}}(t) \tag{III.3.43}$$

$$\hat{u}(t) = \tilde{\mathbf{C}}\hat{\mathbf{X}}(t) + \tilde{\mathbf{D}}\hat{y}_{\mathrm{tot}}(t) \quad = -\mathbf{D}^{-1}\mathbf{C}\hat{\mathbf{X}}(t) + \mathbf{D}^{-1}\hat{y}_{\mathrm{tot}}(t) \tag{III.3.44}$$

Consider A_{a}, A_{m}, A_{p} for some fixed $u(t) = u_{\mathrm{eq}}$, i.e. the Jacobian of the active, middle, passive branch of an individual component under constant-*voltage* control.

What can we infer about the stability of the ensemble under constant-global-*current* control? This question means asking what we can conclude about $\tilde{\mathbf{A}}$ at that voltage u_{eq}, the Jacobian of the ensemble under current control. This question is treated in the next subsections.

III.3.3.2 Stability analysis of the Jacobian $\tilde{\mathbf{A}}$

The eigenvectors of $\tilde{\mathbf{A}}$ can be separated into two categories. The eigenvectors of the first category each affect only members within a single group, so we call them intra-group perturbations. The eigenvectors of the second category, let us call them inter-group perturbations, affect two or more groups, but they move each group as a whole, not perturbing the individual members of a group against each other.

III.3.3.3 Intra-group perturbation

Let v_{a}, v_{m}, $v_{\mathrm{p}} \in \mathbb{R}^{n\times 1}$ be eigenvectors of A_{a}, A_{m}, A_{p} and let $\lambda_{\mathrm{a}}, \lambda_{\mathrm{m}}, \lambda_{\mathrm{p}}$ be the corresponding eigenvalues:

$$\forall s \in \{\mathrm{a},\mathrm{m},\mathrm{p}\} : \ (A_s - \lambda_s \mathbb{I}_{N_s}) v_s = 0 \tag{III.3.45}$$

Let $V_{N_s} \in \mathbb{R}^{N_s\times 1}$, $\forall s \in \{\mathrm{a},\mathrm{m},\mathrm{p}\}$ be arbitrary vectors of zero 1-norm, i.e.

$$\forall s \in \{\mathrm{a},\mathrm{m},\mathrm{p}\} : \ \mathbf{1}^{1\times N_s} V_{N_s} = 0 \tag{III.3.46}$$

Then the following $\mathbf{V}_{\mathrm{a}}, \mathbf{V}_{\mathrm{m}}, \mathbf{V}_{\mathrm{p}}$ are eigenvectors of $\tilde{\mathbf{A}}$:

$$(\tilde{\mathbf{A}} - \lambda_{\mathrm{a}} \mathbb{I}_{Nn}) \underbrace{\begin{pmatrix} V_{N_{\mathrm{a}}} \otimes v_{\mathrm{a}} \\ \mathbf{0}^{N_{\mathrm{m}} n\times 1} \\ \mathbf{0}^{N_{\mathrm{p}} n\times 1} \end{pmatrix}}_{=:\mathbf{V}_{\mathrm{a}}} = 0 \tag{III.3.47}$$

$$(\tilde{\mathbf{A}} - \lambda_{\mathrm{m}} \mathbb{I}_{Nn}) \underbrace{\begin{pmatrix} \mathbf{0}^{N_{\mathrm{a}}\times 1} \\ V_{N_{\mathrm{m}}} \otimes v_{\mathrm{m}} \\ \mathbf{0}^{N_{\mathrm{p}} n\times 1} \end{pmatrix}}_{=:\mathbf{V}_{\mathrm{m}}} = 0 \tag{III.3.48}$$

$$(\tilde{\mathbf{A}} - \lambda_{\mathrm{p}} \mathbb{I}_{Nn}) \underbrace{\begin{pmatrix} \mathbf{0}^{N_{\mathrm{a}} n\times 1} \\ \mathbf{0}^{N_{\mathrm{m}} n\times 1} \\ V_{N_{\mathrm{p}}} \otimes v_{\mathrm{p}} \end{pmatrix}}_{=:\mathbf{V}_{\mathrm{p}}} = 0 \tag{III.3.49}$$

Checking (III.3.47), exemplarily:

$$
\begin{aligned}
(\tilde{\mathbf{A}} - \lambda_\mathrm{a}\mathbb{I}_{Nn})\mathbf{V}_\mathrm{a} &\overset{\text{(III.3.43)}}{=} \mathbf{A}\mathbf{V}_\mathrm{a} - \mathbf{B}\mathbf{D}^{-1}\mathbf{C}\mathbf{V}_\mathrm{a} - \lambda_\mathrm{a}\mathbb{I}_{Nn}\mathbf{V}_\mathrm{a} \\
&\overset{\text{(III.3.39),(III.3.41)}}{=} \begin{pmatrix} (\mathbb{I}_{N_\mathrm{a}} \otimes A_\mathrm{a})(V_{N_\mathrm{a}} \otimes v_\mathrm{a}) \\ \mathbf{0}^{(N_\mathrm{m}+N_\mathrm{p})n\times 1} \end{pmatrix} - \mathbf{B}\mathbf{D}^{-1} \begin{pmatrix} (\mathbf{1}^{1\times N_\mathrm{a}} \otimes C_\mathrm{a})(V_{N_\mathrm{a}} \otimes v_\mathrm{a}) \\ \mathbf{0}^{(N_\mathrm{m}+N_\mathrm{p})n\times 1} \end{pmatrix} - \lambda_\mathrm{a}\mathbf{V}_\mathrm{a} \\
&= \begin{pmatrix} \mathbb{I}_{N_\mathrm{a}}\, V_{N_\mathrm{a}} \otimes A_\mathrm{a}\, v_\mathrm{a} \\ \mathbf{0}^{(N_\mathrm{m}+N_\mathrm{p})n\times 1} \end{pmatrix} - \mathbf{B}\mathbf{D}^{-1} \underbrace{\begin{pmatrix} \mathbf{1}^{1\times N_\mathrm{a}}\, V_{N_\mathrm{a}} \otimes C_\mathrm{a}\, v_\mathrm{a} \\ \mathbf{0}^{(N_\mathrm{m}+N_\mathrm{p})n\times 1} \end{pmatrix}}_{\overset{\text{(III.3.46)}}{=}\mathbf{0}^{(N_\mathrm{a}+N_\mathrm{m}+N_\mathrm{p})n\times 1}} - \lambda_\mathrm{a}\mathbf{V}_\mathrm{a} \\
&\overset{\text{(III.3.45)}}{=} \begin{pmatrix} V_{N_\mathrm{a}} \otimes \lambda_\mathrm{a} v_\mathrm{a} \\ \mathbf{0}^{(N_\mathrm{m}+N_\mathrm{p})n\times 1} \end{pmatrix} - \lambda_\mathrm{a}\mathbf{V}_\mathrm{a} \\
&= \lambda_\mathrm{a}\mathbf{V}_\mathrm{a} - \lambda_\mathrm{a}\mathbf{V}_\mathrm{a} \\
&= 0
\end{aligned}
\tag{III.3.50}
$$

Equation (III.3.47), (III.3.48) and (III.3.49) yield $n(N_\mathrm{a}-1)$, $n(N_\mathrm{m}-1)$, $n(N_\mathrm{p}-1)$ independent eigenvectors of $\tilde{\mathbf{A}}$, if $N_\mathrm{a}, N_\mathrm{p}, N_\mathrm{m} \neq 0$, respectively, otherwise none. This is because there are n dimensions to choose $v_\mathrm{a}, v_\mathrm{m}, v_\mathrm{p}$ from and $N_\mathrm{a}-1, N_\mathrm{m}-1, N_\mathrm{p}-1$ dimensions for $V_{N_\mathrm{a}}, V_{N_\mathrm{m}}, V_{N_\mathrm{p}}$.

Notice that the eigenvectors in Eq (III.3.47), (III.3.48) and (III.3.49) each have non-zero entries only in one of the groups. Thus, they describe intra-group perturbations. They leave the voltage $\hat{u}(t)$ unchanged, since $\tilde{\mathbf{C}}\mathbf{V}_s = 0$, $\forall s \in \{\mathrm{a}, \mathrm{m}, \mathrm{p}\}$. Furthermore, the stability/instability of the ensemble equilibrium with respect to intra-group perturbations can be directly inferred from the stability/instability of the individual components. This means for instance that if $N_\mathrm{m} > 1$, then a positive eigenvalue λ_m of an individual, *voltage*-control Jacobian A_m directly implies instability of the *current*-controlled ensemble with Jacobian $\tilde{\mathbf{A}}$. This is why any stable ensemble-equilibrium can have at most one single component in the "m"-state.

III.3.3.4 Inter-group perturbations

Previously, we described eigenvectors $\mathbf{V}_\mathrm{a}, \mathbf{V}_\mathrm{m}, \mathbf{V}_\mathrm{p}$ corresponding to perturbations within single groups. In contrast, the following eigenvectors $\mathbf{V}$ each perturb more than one group, but leave the components within each group synchronous to each other. We claim that the following Eq. (III.3.51) describes the remaining $3n$ (or less if a group is empty) eigenvectors $\mathbf{V}$ of the current-control Jacobian $\tilde{\mathbf{A}}$ to the eigenvalues λ:

$$
(\tilde{\mathbf{A}} - \lambda\,\mathbb{I}_{Nn})\,\underbrace{(\mathbf{A} - \lambda\,\mathbb{I}_{Nn})^{-1}\mathbf{B}}_{=:\mathbf{V}} = 0 \tag{III.3.51}
$$

However, such an eigenvector $\mathbf{V}$ only exists, if $(\mathbf{A} - \lambda\,\mathbb{I}_{Nn})$ is invertible. $(\mathbf{A} - \lambda\,\mathbb{I}_{Nn})$ is invertible, if and only if we assume $\lambda \neq \lambda_\mathrm{a}, \lambda_\mathrm{m}, \lambda_\mathrm{p}$. This is because if $\lambda \neq$

$\lambda_\mathrm{a}, \lambda_\mathrm{m}, \lambda_\mathrm{p}$, then and only then λ is not an eigenvalue of $\mathbf{A}$, which are N_s-times $\lambda_s, \forall s \in \{\mathrm{a}, \mathrm{m}, \mathrm{p}\}$, see the definition of $\mathbf{A}$ in Eq. (III.3.39). But if λ is not an eigenvalue of $\mathbf{A}$, then and only then $\det(\mathbf{A} - \lambda \mathbb{I}_{Nn}) \neq 0$, i.e. $(\mathbf{A} - \lambda \mathbb{I}_{Nn})$ is invertible. (The case $\lambda = \lambda_\mathrm{a}, \lambda_\mathrm{m}, \lambda_\mathrm{p}$ is treated in the next subsection.)

We further claim that the corresponding eigenvalues λ are obtained by solving Eq. (III.3.52), which might be difficult in general:

$$0 = -\mathbf{C} \underbrace{(\mathbf{A} - \lambda \mathbb{I}_{Nn})^{-1}\mathbf{B}}_{\equiv \mathbf{V}} + \mathbf{D} \tag{III.3.52}$$

$$\overset{\substack{\text{(III.3.36),}\\ \text{(III.3.37)}}}{\equiv} \frac{\mathcal{L}\{\hat{y}_\mathrm{tot}\}(\lambda)}{\mathcal{L}\{\hat{u}\}(\lambda)} := Y_\mathrm{tot}(\lambda) \tag{III.3.53}$$

$\mathcal{L}$ denotes the Laplace transformation and in Eq. (III.3.52) we used $\mathcal{L}\{\frac{\mathrm{d}}{\mathrm{d}t}\hat{\mathbf{X}}\}(\lambda) = \lambda\mathcal{L}\{\hat{\mathbf{X}}\}(\lambda)$. Eq. (III.3.51) and (III.3.52) say that, at the eigenvalues λ of $\tilde{\mathbf{A}}$, the total admittance $Y_\mathrm{tot}(\lambda)$ vanishes. Notice that $Y_\mathrm{tot}(\lambda)$ is only defined, if λ is not an eigenvalue of $\mathbf{A}$. Analogously, the total impedance $Z_\mathrm{tot}(\lambda) := Y_\mathrm{tot}^{-1}(\lambda)$ is only defined if λ is not an eigenvalue of $\tilde{\mathbf{A}}$. Let us confirm Eq. (III.3.51):

$$\begin{aligned}
(\tilde{\mathbf{A}} - \lambda\mathbb{I}_{Nn})\mathbf{V} &\overset{\text{(III.3.43)}}{=} (\mathbf{A} - \mathbf{B}\mathbf{D}^{-1}\mathbf{C} - \lambda\mathbb{I}_{Nn})\mathbf{V} \\
&= (\mathbf{A} - \lambda\mathbb{I}_{Nn})\mathbf{V} - \mathbf{B}\mathbf{D}^{-1}\underbrace{\mathbf{C}\mathbf{V}}_{\overset{III.3.52}{=}\mathbf{D}} \\
&\overset{\text{(III.3.51)}}{=} (\mathbf{A} - \lambda\mathbb{I}_{Nn})(\mathbf{A} - \lambda\mathbb{I}_{Nn})^{-1}\mathbf{B} - \mathbf{B}\mathbf{D}^{-1}\mathbf{D} \\
&= \mathbf{B} - \mathbf{B} \\
&= 0
\end{aligned} \tag{III.3.54}$$

Eq. (III.3.52) can be hard to solve. However, if we only care about whether the ensemble can oscillate or not, we only need to look for a Hopf-bifurcation, at which a complex-conjugate pair of eigenvalues λ, λ^* of the Jacobian $\tilde{\mathbf{A}}$ passes the imaginary axis in the complex plane under parameter variation [78]. The frequency of the resulting oscillation is $\omega/(2\pi)$ and obeys $i\omega = \lambda = -\lambda^*$, in which i is the imaginary unit.

If we insert $i\omega$ for λ, each of the three groups has an admittance

$$Y_s(i\omega) = Y_s(-i\omega)^* = -C_s(A_s - i\omega\mathbb{I}_{N_s n})^{-1}B_s + D_s, \ \forall s \in \{\mathrm{a}, \mathrm{m}, \mathrm{p}\} \tag{III.3.55}$$

and the total admittance is the sum of them

$$Y_\mathrm{tot}(i\omega) = \sum_{s\in\{\mathrm{a},\mathrm{m},\mathrm{p}\}} Y_s(i\omega) \tag{III.3.56}$$

If we limit ourselves to components of dimension $n = 1$, the impedance of each of the groups can be represented as one of the two circuits in Fig. III.3.2 a,b, in which

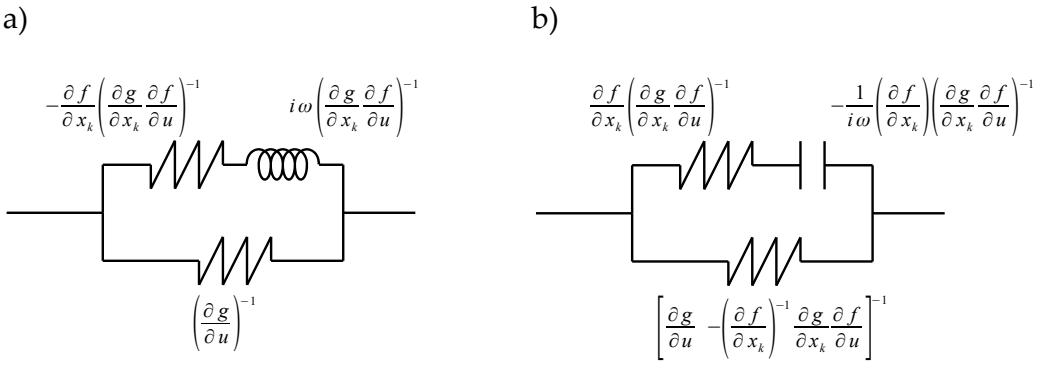

Figure III.3.2: Circuit representations of Eq. (III.3.1), (III.3.2) for a scalar x_k

the choice between the inductive version (Fig. III.3.2a) and the capacitive version (Fig. III.3.2b) depends on the sign of the product $CB = \partial g/\partial x_k \, \partial f/\partial u$. For an LC-circuit we need both, inductance and capacitance, and in fact this requirement for a Hopf bifurcation is also found when looking at the imaginary part of Eq. (III.3.52), in which Y_{tot} is written as the sum of the impedances of the three groups:

$$\begin{aligned} 0 &= \operatorname{Im}(Y_{\text{tot}}(i\omega)) \\ &= \sum_{s\in\{\text{a,m,p}\}} \underbrace{-i\omega N_s C_s (A_s + i\omega)^{-1}(A_s - i\omega)^{-1} B_s}_{\operatorname{Im}(Y_s(i\omega))} \\ &\overset{n=1}{=} \sum_{s\in\{\text{a,m,p}\}} -i\omega N_s C_s B_s |A_s + i\omega|^{-2} \end{aligned} \tag{III.3.57}$$

This equation needs to hold at a Hopf-bifurcation. For $n = 1$, this criterion can only be fulfilled if we have both, a group s_1 with $C_{s_1} B_{s_1} < 0$ and a group s_2 with $C_{s_2} B_{s_2} > 0$ such that the total sum is zero. (All summands may also be zero, but this is a degenerate case.) This means that the product CB has to change its sign along the equilibrium curve of the individual components, as illustrated in the next chapter with an example (Fig.III.4.1). Thus, the necessary condition for a Hopf bifurcation in the considered class of system, a core result of this part of the thesis, is given by:

$$\begin{aligned} \exists u : \exists x_1, x_2 : \quad & f(x_1, u) = f(x_2, u) = 0 \\ & \wedge \ \partial g/\partial x_k|_{x_1,u} \, \partial f/\partial u|_{x_1,u} < 0 \\ & \wedge \ \partial g/\partial x_k|_{x_2,u} \, \partial f/\partial u|_{x_2,u} > 0 \end{aligned} \tag{III.3.58}$$

This criterion specifies that there is a voltage u for which at least one branch behaves capacitively and at least one branch that behaves inductively, which both is

necessary to form an LC circuit and, thus, voltage oscillations. However, even if a certain given ensemble equilibrium fulfills this, the oscillations could still be damped or overdamped, which depends on the values of the resistors in the equivalent circuit in Fig. III.3.2. On the other hand, damped voltage-oscillations also require an LC circuit, i.e. the criterion (III.3.58) needs to be fulfilled. In the Chap.III.4, we introduce an exemplary model.

III.3.3.5 Circuit representation

Let us check that the circuit representations in Fig. III.3.2 are actually valid. The component equation

$$\frac{\mathrm{d}}{\mathrm{d}t}x(t) = f(x(t), u(t)) \tag{III.3.59}$$

$$y(t) = g(x(t), u(t)) \tag{III.3.60}$$

can be linearized

$$\frac{\mathrm{d}}{\mathrm{d}t}\hat{x}(t) = f_x\hat{x}(t) + f_u\hat{u}(t) \tag{III.3.61}$$

$$\hat{y}(t) = g_x\hat{x}(t) + g_u\hat{u}(t) \tag{III.3.62}$$

and Laplace transformed:

$$i\omega\mathcal{L}[\hat{x}](i\omega) = f_x\mathcal{L}[\hat{x}](i\omega) + f_u\mathcal{L}[\hat{u}(t)](i\omega) \tag{III.3.63}$$

$$\mathcal{L}[\hat{y}](i\omega) = g_x\mathcal{L}[\hat{x}](i\omega) + g_u\mathcal{L}[\hat{u}(t)](i\omega) \tag{III.3.64}$$

Eliminating $\mathcal{L}[\hat{x}](i\omega)$ we get the admittance $Y(i\omega)$:

$$\mathcal{L}[\hat{y}](i\omega) = \underbrace{\left[g_x(i\omega - f_x)^{-1}f_u + g_u\right]}_{Y(i\omega)}\mathcal{L}[\hat{u}(t)](i\omega) \tag{III.3.65}$$

In comparison, the circuit in Fig. III.3.2a yields the same, identifying R_1, R_2, L with the respective values of the three electrical components.

$$Y(i\omega) = (i\omega L + R_2)^{-1} + R_1^{-1} \tag{III.3.66}$$

$$= \left[i\omega(g_xf_u)^{-1} - f_x(g_xf_u)^{-1}\right]^{-1} + g_u \tag{III.3.67}$$

$$= g_x\left[i\omega - f_x\right]^{-1}f_u + g_u \tag{III.3.68}$$

Analogously, the same is true for the circuit in Fig. III.3.2b, with R_1, R_2, C.

$$Y(i\omega) = [(i\omega C)^{-1} + R_2]^{-1} + R_1^{-1} \tag{III.3.69}$$

$$= \left[-(i\omega)^{-1} f_x^2 (g_x f_u)^{-1} + f_x (g_x f_u)^{-1}\right]^{-1} + (g_u - f_x^{-1} g_x f_u) \tag{III.3.70}$$

$$= g_x \left[\frac{1}{-(i\omega)^{-1} f_x^2 + f_x} - \frac{1}{f_x}\right] f_u + g_u \tag{III.3.71}$$

$$= g_x \left[\frac{-i\omega}{f_x^2 - i\omega f_x} - \frac{f_x - i\omega}{f_x^2 - i\omega f_x}\right] f_u + g_u \tag{III.3.72}$$

$$= g_x \left[\frac{-f_x}{f_x^2 - i\omega f_x}\right] f_u + g_u \tag{III.3.73}$$

$$= g_x \left[i\omega - f_x\right]^{-1} f_u + g_u \tag{III.3.74}$$

III.3.3.6 Zero eigenvalues

Consider a turning point of an individual component as described in Eq (III.3.28). What does it mean for the eigenvalues of $\tilde{\mathbf{A}}$, the Jacobian of the current-controlled ensemble, if two branches of an individual component meet, for instance "a" and "m"? It means that two of the three groups fuse, their members becoming indistinguishable. So there is an eigenvalue λ_a of A_a and an eigenvalue λ_m of A_m with $\lambda_\mathrm{a} = \lambda_\mathrm{m} = 0$ or, analogously, $\lambda_\mathrm{m} = \lambda_\mathrm{p} = 0$. Furthermore, it means that instead of an inter-group eigenvalue λ as in the subsection before, which solves Eq (III.3.52), we get, for instance, an eigenvalue $\lambda = \lambda_\mathrm{a} = \lambda_\mathrm{m} = 0$. The eigenvector $\mathbf{V}$ of $\tilde{\mathbf{A}}$ to the eigenvalue λ can then again be written in terms of v_a and v_m, the eigenvectors of A_a and A_m to the eigenvalues λ_a and λ_m:

$$(\tilde{\mathbf{A}} - \lambda \mathbb{I}_N) \underbrace{\begin{pmatrix} \frac{1}{N_\mathrm{a}} (\mathbf{1}^{N_\mathrm{a} \times 1} \otimes v_\mathrm{a}) \\ -\frac{1}{N_\mathrm{m}} (\mathbf{1}^{N_\mathrm{m} \times 1} \otimes v_\mathrm{m}) \\ \mathbf{0}^{N_\mathrm{p} n \times 1} \end{pmatrix}}_{\mathbf{V}} = 0 \tag{III.3.75}$$

Here, individual components can arbitrarily switch between "a" and "m", since the two groups are now indistinguishable. Analogously, if $\lambda = \lambda_\mathrm{m} = \lambda_\mathrm{p}$:

$$(\tilde{\mathbf{A}} - \lambda \mathbb{I}_N) \underbrace{\begin{pmatrix} \mathbf{0}^{N_\mathrm{a} n \times 1} \\ \frac{1}{N_\mathrm{m}} (\mathbf{1}^{N_\mathrm{m} \times 1} \otimes v_\mathrm{m}) \\ -\frac{1}{N_\mathrm{p}} (\mathbf{1}^{N_\mathrm{p} \times 1} \otimes v_\mathrm{p}) \end{pmatrix}}_{\mathbf{V}} = 0 \tag{III.3.76}$$

III.3.3.7 Saddle-node bifurcation of the *voltage*-controlled ensemble, i.e. Z=0

In a voltage-controlled ensemble the individual components are decoupled. So if the individual components, which are identical, have a saddle-node bifurcation at some $(u^{\mathrm{sn}}, y^{\mathrm{sn}}, x^{\mathrm{sn}}) \in \mathbf{E}$, under *voltage*-control, then the entire ensemble has many saddle-node bifurcations at that u^{sn}. However, because of symmetry, some of these saddle-node bifurcations lie on the same points in phase space, such that we actually have several multi-branch bifurcations that are equivariant with respect to some index permutations.

Let us look at these equivariant bifurcations in more quantitative detail. Close to such a bifurcation point $(u^{\mathrm{sn}}, y^{\mathrm{sn}}, x^{\mathrm{sn}})$, the i-th component has the equilibria $(u_i^{\mathrm{eq}}, y_i^{\mathrm{eq}}, x_i^{\mathrm{eq}})$:

$$(y_i^{\mathrm{eq}} - y^{\mathrm{sn}}) = \pm\gamma\sqrt{-\frac{\beta(u_i^{\mathrm{eq}} - u^{\mathrm{sn}})}{\alpha}} + D(u_i^{\mathrm{eq}} - u^{\mathrm{sn}}), \tag{III.3.77}$$

The two branches meet at $(u^{\mathrm{sn}}, y^{\mathrm{sn}}, x^{\mathrm{sn}})$. Without loss of generality (wlog), let us assume that it is the "a"- and "m"-branch that meet, with the $\pm$ in Eq. (III.3.77) assigning the branch for each component in question. Wlog, assume "+" goes to "a" and "-" goes to "m". The members of the remaining "p"-group sit at $(u^{\mathrm{sn}}, y_{\mathrm{p}}^{\mathrm{sn}}, x_{\mathrm{p}}^{\mathrm{sn}})$ during the bifurcation and their Jacobian A_{p} is still invertible. If u is close to u^{sn}, they reside close to the following current-voltage line:

$$(y_i^{\mathrm{eq}} - y_{\mathrm{p}}^{\mathrm{sn}}) = \left(C_{\mathrm{p}} A_{\mathrm{p}}^{-1} B_{\mathrm{p}} + D_{\mathrm{p}}\right)(u_i^{\mathrm{eq}} - u^{\mathrm{sn}}) \tag{III.3.78}$$

Defining $y_{\mathrm{tot}}^{\mathrm{eq}} := \sum_{i=1}^{N} y_i^{\mathrm{eq}}$ and $u^{\mathrm{eq}} := u_i^{\mathrm{eq}}$, $\forall i \in \{1, \ldots, N\}$, and summing up Eq. (III.3.77) and (III.3.78), respectively, for all the N components, we get Eq. (III.3.79) for the current-voltage curve of the ensemble:

$$\begin{aligned} y_{\mathrm{tot}}^{\mathrm{eq}} - (N_{\mathrm{a}} + N_{\mathrm{m}}) y^{\mathrm{sn}} - N_{\mathrm{p}} y_{\mathrm{p}}^{\mathrm{sn}} \; &= (N_{\mathrm{a}} - N_{\mathrm{m}})\gamma\sqrt{-\frac{\beta(u^{\mathrm{eq}} - u^{\mathrm{sn}})}{\alpha}} + D_{\mathrm{m}}(u^{\mathrm{eq}} - u^{\mathrm{sn}}) \\ &\quad + N_{\mathrm{p}}\left(C_{\mathrm{p}} A_{\mathrm{p}}^{-1} B_{\mathrm{p}} + D_{\mathrm{p}}\right)(u^{\mathrm{eq}} - u^{\mathrm{sn}}) \end{aligned} \tag{III.3.79}$$

Notice that $D_{\mathrm{m}} \equiv D_{\mathrm{a}}$ at the bifurcation. There are $N - N_{\mathrm{p}} + 1$ combinations to choose the tuple $(N_{\mathrm{a}}, N_{\mathrm{m}})$ from, so there are $N - N_{\mathrm{p}} + 1$ different branches emerging from $(u^{\mathrm{sn}}, y^{\mathrm{sn}})$ in a $y_{\mathrm{tot}}^{\mathrm{eq}}$-$u^{\mathrm{eq}}$ plot. The number of branches is larger if you distinguish components. Notice that at voltage u^{sn} we get not just one, but N such special branching points, each at a different current $y_{\mathrm{tot}} = (N_{\mathrm{a}} + N_{\mathrm{m}}) y^{\mathrm{sn}} + N_{\mathrm{p}} y_p^{\mathrm{sn}}$. The current at the k-th branching point is $[(N-k)y^{\mathrm{sn}} + k y_{\mathrm{p}}^{\mathrm{sn}}]$ and the number of its branches is $(N-k)+1$.

Since the position of the equilibria does not depend on whether u or y_{tot} is controlled, we have also learned something about the y_{tot}-controlled ensemble, even though there it is not just an ensemble of uncoupled components. This will be discussed in Chap. III.5 with the help of an example model.

Chapter III.4

Model

Before, we have discussed various general concepts of coupled bistable systems, regarding equilibria and their linear stability. In this chapter, we apply these ideas to a simplified model for parallelly connected Pt microelectrodes in a CO containing solution. This model is capable of reproducing two interesting experimental observations. Moreover, it makes it easy to illustrate the mechanisms behind. The first observation is the individual switching of the microelectrodes as the total current is gradually increased. The second observation is the oscillation of the electrode potential for a fixed current.

III.4.1 Derivation of the model

We derived our model from the following, more detailed model for the CO adsorption on a platinum micro-electrode [66, 67, 74].

$$\frac{\mathrm{d}}{\mathrm{d}t}C_i = \frac{2D}{\delta^2}(C_\mathrm{b} - C_i) - \frac{S_\mathrm{tot}}{\delta}(k_\mathrm{ads}C_i(1-\theta_i) - k_\mathrm{des}\theta_i) \tag{III.4.1}$$

$$\frac{\mathrm{d}}{\mathrm{d}t}\theta_i = k_\mathrm{ads}C_i(1-\theta_i) - k_\mathrm{des}\theta_i - k_\mathrm{reac}\theta_i(1-\theta_i)\exp(\alpha f \phi_i) \tag{III.4.2}$$

$$J_i = 2FS_\mathrm{tot}k_\mathrm{reac}\theta_i(1-\theta_i)\exp(\alpha f \phi_i) \tag{III.4.3}$$

This model is already able to reproduce the individual switching and the potential oscillations, but it makes it very hard to understand why the oscillations occur, so we need to simplify it. Our simplified model captures the steady states of Eq. (III.4.1) and (III.4.2). Its impedance is not exactly the same as in the original model, but it still provides oscillations as an ensemble.

To obtain our simplified version, we set $\mathrm{d}C_i/\mathrm{d}t$ to zero to eliminate C_i, so Eq. (III.4.2) becomes Eq. (III.4.4).

$$\frac{\mathrm{d}}{\mathrm{d}t}\theta_i = \frac{DC_\mathrm{b}k_\mathrm{ads} - (DC_\mathrm{b}k_\mathrm{ads} + Dk_\mathrm{des})\theta_i}{D + k_\mathrm{ads}\delta S_\mathrm{tot} - k_\mathrm{ads}\delta S_\mathrm{tot}\theta_i} - k_\mathrm{reac}\theta_i(1-\theta_i)\exp(\alpha f \phi_i) \tag{III.4.4}$$

$$J_i = 2FS_\mathrm{tot}k_\mathrm{reac}\theta_i(1-\theta_i)\exp(\alpha f \phi_i) \tag{III.4.5}$$

Then, defining

$$\tau := \frac{DC_\mathrm{b}}{\delta S_\mathrm{tot}} \tag{III.4.6}$$

$$u_i := \frac{\delta S_\mathrm{tot}}{DC_\mathrm{b}} k_\mathrm{reac} \exp(\alpha f \phi_i) \tag{III.4.7}$$

$$y_i := J_i \frac{\delta}{2FDC_\mathrm{b}} \tag{III.4.8}$$

$$a := \frac{D}{k_\mathrm{ads} \delta S_\mathrm{tot}} \tag{III.4.9}$$

$$b := \frac{k_\mathrm{des} \delta S_\mathrm{tot}}{DC_\mathrm{b}}. \tag{III.4.10}$$

we are left with

$$\frac{\mathrm{d}}{\mathrm{d}\tau}\theta_i = \frac{1-(1+ab)\theta_i}{1+a-\theta_i} - \theta_i(1-\theta_i)u_i \tag{III.4.11}$$

$$y_i = \theta_i(1-\theta_i)u_i \tag{III.4.12}$$

in which a and b are small, positive constants. We rename τ to t and θ_i to x_i and changed the values of a and b to make the system less stiff, but we kept them much smaller than one.

III.4.2 Model

The following first order ordinary differential equation (ODE) describes a single electrode, where the surface coverage $x(t)$ is defined on the unit interval [0,1]:

$$\frac{\mathrm{d}}{\mathrm{d}t}x(t) = \frac{1-(1+ab)x(t)}{1+a-x(t)} - u[1-x(t)]x(t) \tag{III.4.13}$$

The square brackets in this are used in place of regular round brackets for a better readability. Now, we take N instances of Eq. (III.4.13) and couple them globally as in Eq. (III.4.14) and (III.4.15). The setup is sketched in Fig. III.1.1.

$$\frac{\mathrm{d}}{\mathrm{d}t}x_i(t) = \frac{1-(1+ab)x_i(t)}{1+a-x_i(t)} - u(t)[1-x_i(t)]x_i(t) \tag{III.4.14}$$

$$y_\mathrm{tot} = \sum_{i=1}^{N} u(t)[1-x_i(t)]x_i(t) \tag{III.4.15}$$

Eq. (III.4.13) can have up to three equilibria, two of which are stable with an unstable equilibrium in between. For Eq. (III.4.14) it is up to 3^N equilibria for each u, but

there are at most $\binom{3+N-1}{N}$ equilibria that are distinct under index permutations. The term $\binom{3+N-1}{N}$ describes the number of possibilities to distribute N indistinguishable components to 3 distinguishable branches. As we saw before, the admittance of the ensemble is the sum of the admittances of the individual components. Thus, looking at the admittance of Eq. (III.4.13) allows us to draw conclusions on Eq. (III.4.14), (III.4.15). Fig. III.4.1 exemplary illustrates the equilibria and admittance of Eq. (III.4.13) and those of Eq. (III.4.14), (III.4.15) for $N = 3$. The two equilibria at $u = u_1 = 4.418$ and $u = u_2 = 5.295$ both have more than one component on the negative-slope branch, three and two respectively. As we showed, this means that these two equilibria are intra-group unstable with a positive real eigenvalue. Moreover, you can instantly rule out the possibility of resonance at $u = u_1 = 4.418$, because all three components act inductively (orange branch). In other words, the ensemble-impedance lacks a capacitive component (blue branches) to form an LC-circuit. In contrast, the equilibrium like the one at $u = u_3 = 8.368$ can give rise to sustained periodic oscillations, if it becomes inter-group unstable, because it is intra-group stable. In fact, the equilibrium at $y_{\text{tot}} = N \cdot 0.833$ is unstable, and there is a limit cycle oscillation which branches from it at lower y_{tot}. The oscillation is shown in Fig. III.4.2 (top).

Another way of looking at the equilibria of Eq. (III.4.14), (III.4.15) is plotting y_{tot} over u, as in Fig III.4.3. From all possible equilibria for an arbitrary number of components N, Fig III.4.3 shows the ones in which the components are clustered in two groups, where the group size ration is 1:4. Furthermore, the figure indicates the stability of the equilibria with respect to inter-group perturbations (by color) and with respect to intra-group perturbations (by solid/dashed line). The continuation of the two-cluster equilibria was done with Auto [79]. To obtain this two-cluster continuation, we considered a four component version of the system, in which each of the four-components represented one of four groups with sizes N_1, N_2, N_3, N_4 with $N_1 + N_2 + N_3 + N_4 = N$. We considered four groups because this allowed us to divide each of the two groups into two subgroups. In this way, we were able to obtain the respective *intra*-group stability. To account for the group sizes, we modified Eq. (III.3.2) to $y_\ell = (N_\ell/N)g(x_\ell, u)$. We fixed $(N_1 + N_2)/N = 0.8$ (size of the first cluster) and $(N_3 + N_4)/N = 0.2$ (size of the second cluster), and $N_2/N = 0.16$ and $N_4/N = 0.04$. Note that with $y_\ell = (N_\ell/N)g(x_\ell, u)$, the model depends only on the relative sizes of the groups and not on the total ensemble size N.

Apart from the equilibria, we found another very interesting feature in Fig III.4.3. Consider the supercritical Hopf bifurcation at about $y_{\text{tot}}/N = 0.785$. In this bifurcation, an inter-group-stable, intra-group-unstable equilibrium is turned into an inter-group-unstable, intra-group-unstable equilibrium and an inter-group-stable, inter-group-unstable limit cycle. These three limit sets all correspond to states that

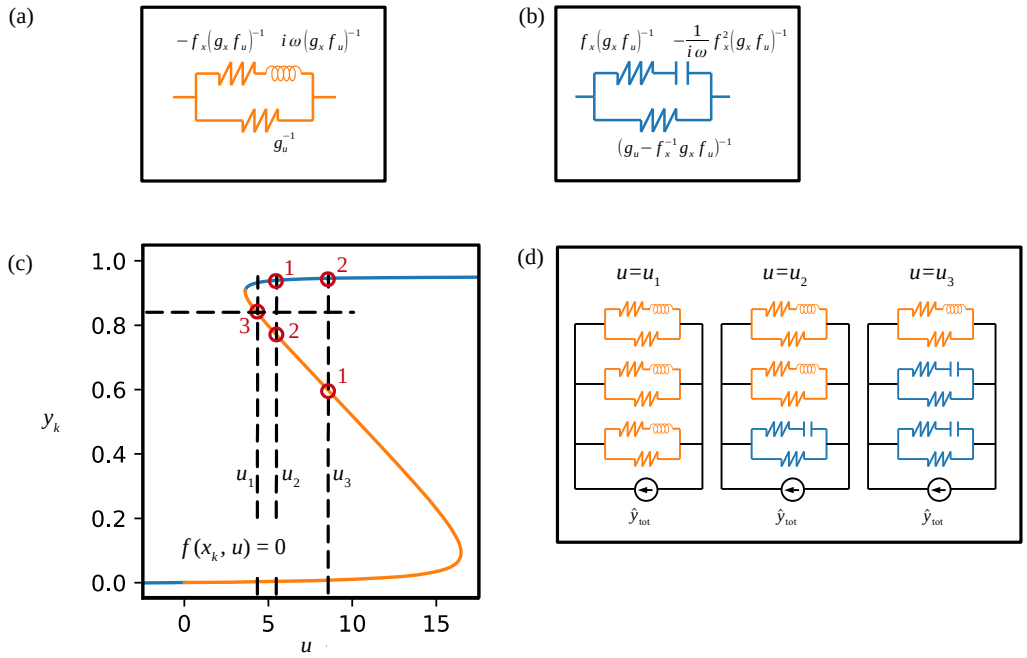

Figure III.4.1: Exemplary illustration of the three equilibria of Eq. (III.4.14), (III.4.15) for $N = 3$, $a = 0.05$, $b = 0.01$ at $y_{\text{tot}} = N \cdot 0.833$, marked by horizontal the dashed line. (a),(b): Circuit representation of the admittance of an individual component for different y_k. (c): Equilibrium line of an individual component. The orange branch corresponds to (a), blue branches to (b). Vertical dashed lines indicate different ensemble equilibria. (d): Circuit representation of the ensemble admittance at each of the three equilibria from (c).

would not be observable in an experiment or a simulation since they all are inter-group-unstable. However, at a slightly larger y_{tot}, the limit cycle undergoes another bifurcation that stabilizes its intra-group direction. The resulting oscillation is shown in Fig. III.4.2 (bottom) for $N = 20$. Notice that both groups have more than one component, even though the limit cycle originally branched from an intra-group-unstable equilibrium. This is an important observation because by the degeneracy of intra-group eigenvalues it means that there is a corresponding stable limit cycle even for very large N, e.g. with group sizes $16 \cdot 10^{22}$ and $4 \cdot 10^{22}$ for $N = 10^{23}$. Since the Pt microelectrodes are a model system for Pt nanoparticles in fuel cells, this could have significant technical implications, because fuel cells are supposed to yield a constant voltage.

In our continuation, the bifurcation in which the intra-group direction of the limit

cycle is stabilized, is a transcritical bifurcation of limit cycles in which the limit cycle collides with another limit-cycle that is not depicted in Fig III.4.3. More details on this are given in the next chapter, where we take a deeper look at the cluster (i.e. group) dynamics of the model that we have just introduced.

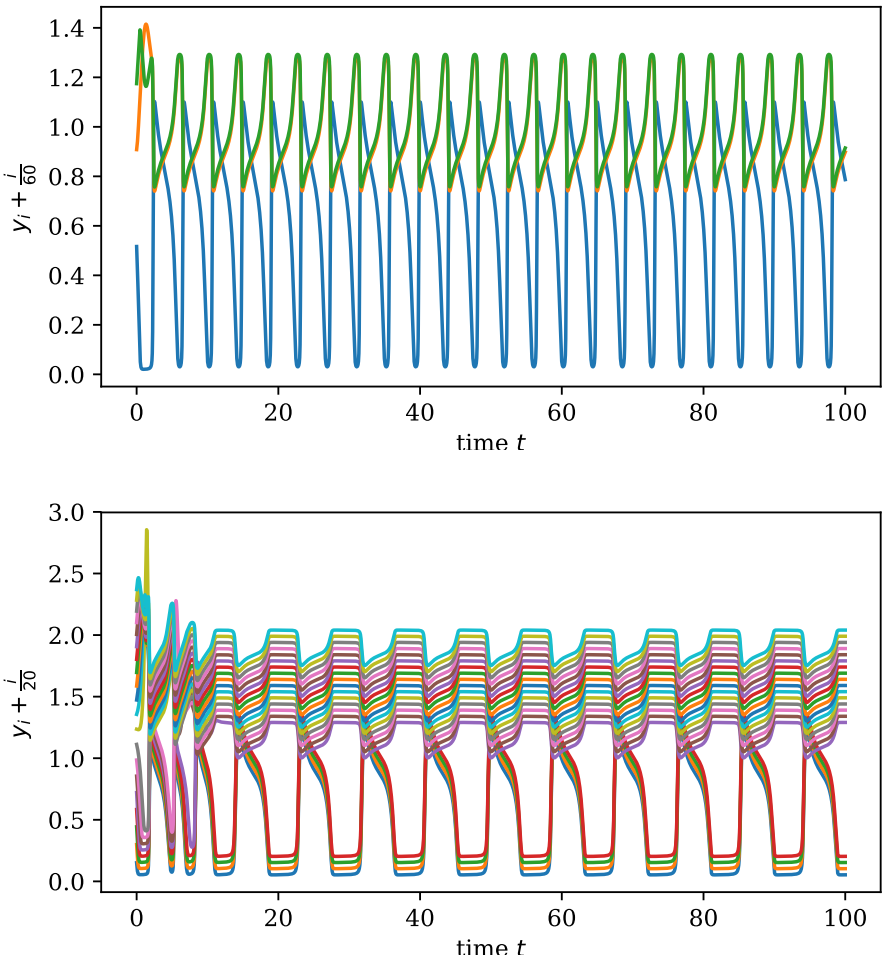

Figure III.4.2: y_i time-series with small offsets, produced by Eq. (III.4.14), (III.4.15) for $N = 3$ (upper plot), $N = 20$ (lower plot), and $a = 0.05$, $b = 0.01$, $y_{\text{tot}} = N \cdot 0.833$ (both plots). The limit cycle that is approached for $N = 3$ has the same intra-group stability as the related equilibrium depicted in Fig. III.4.1 at u_3. They collide in a super-critical inter-group Hopf-bifurcation at a slightly smaller y_{tot} . In contrast, the limit cycle at $N = 20$ does not share the intra-group *instability* of its related equilibrium which it meets in a close-by inter-group Hopf-bifurcation, see Fig. III.4.3.

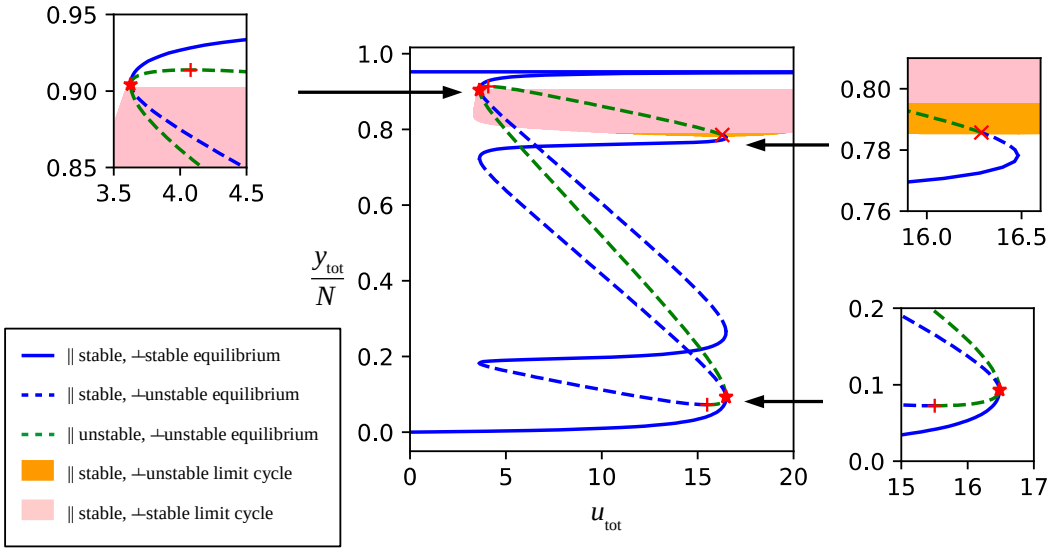

Figure III.4.3: Two-group limit-sets of Eq. (III.4.14), (III.4.15) for $a = 0.05$, $b = 0.01$, for a group-size ratio of 1:4, valid for any number of components N. Solid line: intra-group-stable equilibrium. Dashed line: intra-group-unstable equilibrium. Blue line: inter-group-stable equilibrium. Green line: inter-group-unstable equilibrium. Orange surface: intra-group-unstable, inter-group-stable limit-cycle. Pink surface: stable limit-cycle. "+": saddle-node bifurcation. "x": super-critical Andronov-Hopf bifurcation. "⋆": transcritical bifurcation.

Chapter III.5

Non-linear cluster dynamics of the model

In Chap. III.3, we did a general linear analysis that applies to an entire class of systems. In this chapter, we investigate the nonlinear properties of an examplary model that we defined in Chap. III.4. In particular, we investigate its cluster dynamics. For this purpose, let us slightly rewrite the model equations (III.4.14), (III.4.15):

$$\frac{\mathrm{d}}{\mathrm{d}t}x_k(t) = \frac{1-(1+ab)x_k(t)}{1+a-x_k(t)} - u(t)[1-x_k(t)]x_k(t) \tag{III.5.1}$$

$$y = \frac{1}{N}\sum_{l=1}^{N} u(t)[1-x_l(t)]x_l(t) \tag{III.5.2}$$

This can be rearranged to an explicit form:

$$\frac{\mathrm{d}}{\mathrm{d}t}x_k(t) = \frac{1-(1+ab)x_k(t)}{1+a-x_k(t)} - \frac{[1-x_k(t)]x_k(t)}{\frac{1}{N}\sum_{l=1}^{N}[1-x_l(t)]x_l(t)}y \tag{III.5.3}$$

$$u(t) = \frac{y}{\frac{1}{N}\sum_{l=1}^{N}[1-x_l(t)]x_l(t)} \tag{III.5.4}$$

In the following, we restrict ourselves to $a = 0.05$, $b = 0.01$ and use these abbreviations:

$$f(x) = \frac{1-(1+ab)x}{1+a-x} \tag{III.5.5}$$

$$g(x) = (1-x)x \tag{III.5.6}$$

Thus, our system has the form

$$\frac{\mathrm{d}}{\mathrm{d}t}x_k(t) = f(x_k(t)) - \frac{g(x_k(t))}{\frac{1}{N}\sum_{l=1}^{N} g(x_l(t))}y \tag{III.5.7}$$

$$u(t) = \frac{y}{\frac{1}{N}\sum_{l=1}^{N} g(x_l(t))}. \tag{III.5.8}$$

III.5.1 Cluster subspaces

Cluster subspaces are invariant subsets of the state space. Considering only the dynamics on these subsets significantly reduces the complexity but still allows us to draw conclusions about the full system. Let $A \subset \{1, \ldots, N\}$. Then the cluster subspace

$$C_A = \{(x_1, \ldots, x_N) \mid x_j = x_k \text{ if } k, j \in A\}$$

is dynamically invariant. Let $\mathcal{A} = \{A_1, A_2, \ldots, A_M\}$ be a partition of $\{1, \ldots, N\}$, i.e. $\forall j \neq k : A_j \cap A_k = \emptyset$ and $\bigcup_{A \in \mathcal{A}} A = \{1, \ldots, N\}$. We define $C_{\mathcal{A}}$ as

$$C_{\mathcal{A}} = \bigcap_{A \in \mathcal{A}} C_A, \tag{III.5.9}$$

and call it an M-cluster subspace. Throughout this thesis, we use the terms 'cluster' and 'group' synonymously. Let $a_j = |A_j|$ denote the number of components in the j-th cluster. On $C_{\mathcal{A}}$ the dynamics of the system are M dimensional and given by

$$\frac{\mathrm{d}}{\mathrm{d}t} x_k(t) = f(x_k) - \frac{g(x_k(t))}{\sum_{j=1}^{M} \frac{a_j}{N} g(x_j(t))} y \tag{III.5.10}$$

$$u(t) = \frac{y}{\sum_{j=1}^{M} \frac{a_j}{N} g(x_j(t))} \tag{III.5.11}$$

where the summation now goes over the clusters. If we set $n_l = \frac{a_l}{N}$ and form the limit $N \to \infty$, we can see n_l as a continuous parameters.

III.5.2 Fully synchronized dynamics

On $C_{\{\{1,\ldots,N\}\}} \equiv C_{\{1,\ldots,N\}}$ where all N units have the same value for $x_k(t)$, the system reduces to the following:

$$\frac{\mathrm{d}}{\mathrm{d}t} x_k(t) = \frac{1 - (1 + ab) x_k(t)}{1 + a - x_k(t)} - y \tag{III.5.12}$$

$$u(t) = \frac{y}{[1 - x_k(t)] x_k(t)} \tag{III.5.13}$$

Eq. (III.5.12) has only one single equilibrium point for any valid y, which is described by Eq. (III.5.14), (III.5.15) and is plotted in Fig. III.5.1.

$$x_k = \frac{1 - y - ay}{1 + ab - y} \tag{III.5.14}$$

$$u = \frac{(1 + ab - y)^2 y}{a(b + y)(1 - y - ay)} \tag{III.5.15}$$

We see that the system is monostable everywhere, i.e. for each y there is exactly one single equilibrium. However, there are multiple equilibria for some u.

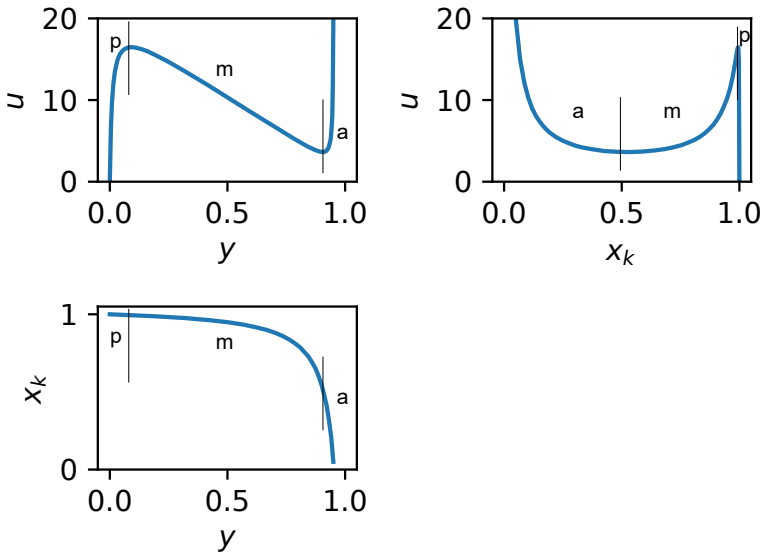

Figure III.5.1: Equilibrium curve in the synchronized subspace $C_{\{\{1,\dots,N\}\}}$. The letters "a", "m", "p" indicate the active, middle, and passive equilibrium branch, respectively, in the sense of y representing a reaction current.

III.5.3 Two-cluster dynamics and bifurcations

Now, we consider a two-cluster subspace $C_{\{A_1,A_2\}}$. The clusters are of relative sizes n_1 and n_2 (with $n_1 + n_2 = 1$) and the dynamics are effectively two dimensional, given by

$$\frac{\mathrm{d}}{\mathrm{d}t}x_1(t) = f(x_1(t)) - \frac{g(x_1(t))}{n_1 g(x_1(t)) + n_2 g(x_2(t))}y \tag{III.5.16a}$$

$$\frac{\mathrm{d}}{\mathrm{d}t}x_2(t) = f(x_2(t)) - \frac{g(x_2(t))}{n_1 g(x_1(t)) + n_2 g(x_2(t))}y \tag{III.5.16b}$$

$$u(t) = \frac{y}{n_1 g(x_1(t)) + n_2 g(x_2(t))}. \tag{III.5.16c}$$

The intersection of all possible two-cluster subspaces contain the fully synchronized subspace $C_{\{\{1,\dots,N\}\}}$, on which $x_1(t) = x_2(t)$. Unlike in the equilibrium in the fully synchronized subspace, the other equilibria in the two-cluster subspace $C_{\{A_1,A_2\}}$ can undergo various bifurcations as y is varied, depending on the choice of n_1, n_2. This is exemplarily illustrated in Fig. III.5.2 for $n_1 = 0.8$, $n_2 = 0.2$. Comparing this to Fig. III.5.1, we see that the fully synchronized equilibria are still in place. They interact with the two-cluster equilibria in two transcritical bifurcations (yellow

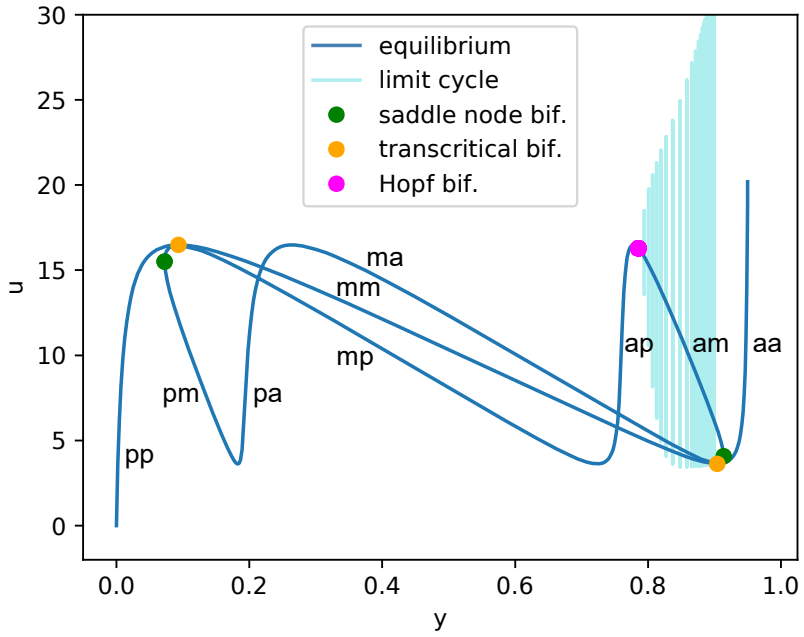

Figure III.5.2: Equilibrium curve on a two-cluster subspace $C_{\{A_1,A_2\}}$ with $n_1 = 0.8$, $n_2 = 0.2$, for $a = 0.05$, $b = 0.01$. Like in Fig. III.5.1, the letters "a", "m", "p" indicate the active, middle, and passive equilibrium branch, respectively. The first of two letters represents x_1, the second x_2.

dots). Furthermore, the two-cluster equilibria undergo saddle-node bifurcations (green dots) and a Hopf bifurcation (purple dot), in which a two-cluster limit-cycle is born (light blue). Consider the transcritical bifurcations. In these bifurcations, the fully synchronous subspace is penetrated by an equilibrium point that lies in the two-cluster subspace $C_{\{A_1,A_2\}}$. So from the four equilibria that branch from the transcritical bifurcations (yellow dots), two lie in the fully synchronous subspace and two do not. Furthermore, for some n_1, one of the transcritical bifurcation points (the one at larger current y) participates in a homoclinic bifurcation, together with the limit cycle (light blue) that originates at the Hopf bifurcation (purple dot). This is illustrated in Fig. III.5.3. At $y = 0.82$, we have three equilibria, a saddle that lies in the fully synchronized subspace $C_{\{\{1,\ldots,N\}\}}$, an unstable two-cluster focus, and a stable two-cluster node. There is also a two-cluster limit cycle around the focus that was just born at a slightly smaller y. At $y = 0.86$, we see that the limit cycle has significantly increased in size and the two rightmost equilibria have moved closer together. At $y \approx 0.904$, there is a homoclinic bifurcation between the limit cycle and the

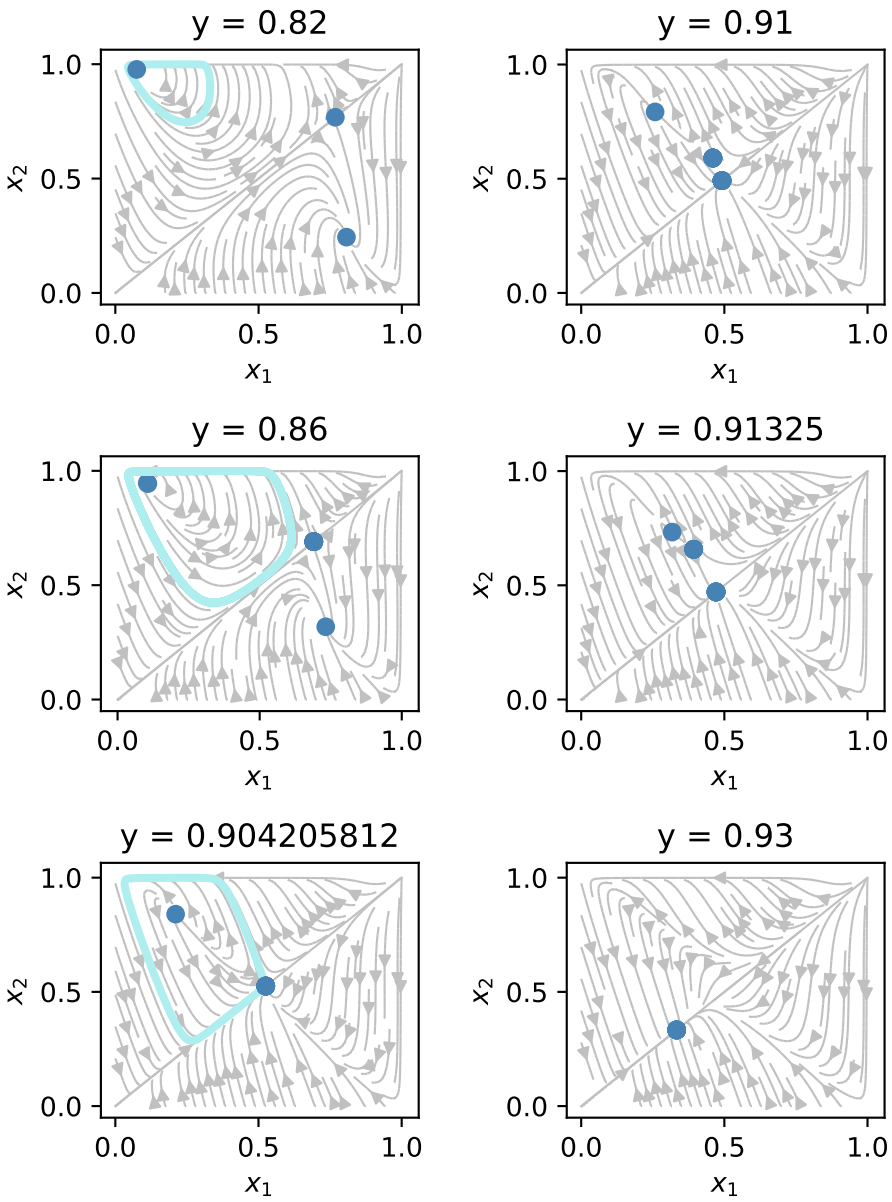

Figure III.5.3: Phase portraits in an invariant two-cluster subspace $C_{\{A_1,A_2\}}$ with $n_1 = 0.8$, $n_2 = 0.2$, for $a = 0.05$, $b = 0.01$.

fully synchronized equilibrium. Simultaneously, the fully synchronized equilibrium undergoes a transcritical bifurcation with one of the two-cluster equilibria. Notice the paradoxical situation: At te homoclinic bifurcation, the lower part of the stable manifold of the fully synchronized equilibrium is formed by the homoclinic loop that is attracting; but at the same time, the invariant, fully synchronized subspace is also its stable manifold. This seems to be resolved somehow by the simultaneous occurrence of the transcritical bifurcation. At $y = 0.91$, the limit cycle is gone and the formerly stable two-cluster node has pierced through the fully synchronized subspace and is has now been turned into a saddle, while the formerly unstable direction of the fully synchronized equilibrium has been stabilized. At $y = 0.91325$, the two two-cluster equilibria have moved very close to each other and at $y = 0.93$ they have annihilated each other in a saddle node bifurcation, such that leaving the fully synchronized equilibrium remains as the only limit set.

For values other than $n_1 = 0.8, n_2 = 0.2$, the bifurcations lie as shown in the two-parameter bifurcation diagram in Fig. III.5.4. Notice that Fig. III.5.4 reflects the symmetry of Eq. III.5.16a, III.5.16b, III.5.16c in n_1. The saddle node bifurcations (green lines) merge with the transcritical bifurcations (yellow lines) at $n_1 = n_2 = 0.5$, where we have a pitchfork bifurcation that is equivariant with respect to index permutation. The Hopf bifurcations (pink lines) merge with a saddle node bifurcation at $n_i = 0$ and at $n_i \approx 0.35$. It is likely that these codimension-two points are likely Takens-Bogdanov bifurcations, indicating that the full bifurcation diagram might be a bit more complicated. Notice that the transcritical bifurcations occur for all n_1, n_2 at the same y. For the full system $C_{\{\{1\},\ldots,\{N\}\}}$ this means that such a transcritical bifurcation occurs in each possible two-cluster subspace $C_{\{A_1,A_2\}}$ simultaneously. This means that there are two branches in the fully synchronized subspace $C_{\{\{1,\ldots,N\}\}}$ and two in each possible two cluster subspace $C_{\{A_1,A_2\}}$, of which there are $(2^N - 2)/2$. If you do not distinguish the components, there are only $N - 1$ distinct two-cluster subspaces. Thus, in the full system $C_{\{\{1\},\ldots,\{N\}\}}$, this transcritical bifurcation point corresponds to a multi-branch bifurcation point that is equivariant with respect to index permutation. For $N = 2$, this is just the pitchfork bifurcation we see in Fig. III.5.4 at $n_1 = 0.5$.

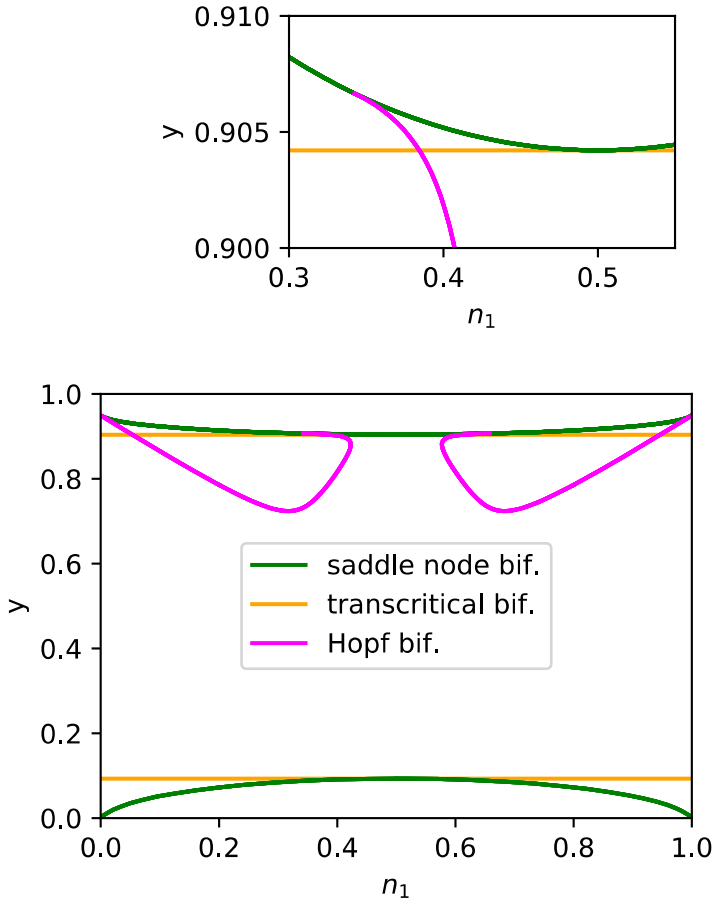

Figure III.5.4: Local bifurcations in a two-cluster subspace $C_{\{A_1,A_2\}}$ with $n_2 = 1 - n_1$, for $a = 0.05$, $b = 0.01$.

III.5.4 Three-cluster dynamics and bifurcations

Now suppose that we have a three-cluster subspace $C_{\{A_1,A_2,A_3\}}$ with three clusters of relative sizes $n_1 + n_2 + n_3 = 1$. On $C_{\{A_1,A_2,A_3\}}$, the dynamics are given by

$$\frac{\mathrm{d}}{\mathrm{d}t}x_1(t) = f(x_1(t)) - \frac{g(x_1(t))}{n_1 g(x_l(t)) + n_2 g(x_2(t)) + n_3 g(x_3(t))} y \tag{III.5.17a}$$

$$\frac{\mathrm{d}}{\mathrm{d}t}x_2(t) = f(x_2(t)) - \frac{g(x_2(t))}{n_1 g(x_l(t)) + n_2 g(x_2(t)) + n_3 g(x_3(t))} y \tag{III.5.17b}$$

$$\frac{\mathrm{d}}{\mathrm{d}t}x_3(t) = f(x_3(t)) - \frac{g(x_3(t))}{n_1 g(x_l(t)) + n_2 g(x_2(t)) + n_3 g(x_3(t))} y \tag{III.5.17c}$$

$$u(t) = \frac{y}{n_1 g(x_1(t)) + n_2 g(x_2(t)) + n_3 g(x_3(t))} \tag{III.5.17d}$$

The invariant three-cluster space $C_{\{A_1,A_2,A_3\}}$ contains the invariant two-cluster spaces $C_{\{A_1\cup A_2,A_3\}}$, $C_{\{A_1,A_2\cup A_3\}}$ and $C_{\{A_1\cup A_3,A_2\}}$, on which the dynamics are given by (III.5.16). Three-cluster subspaces are particularly interesting because all equilibria of the full system (III.5.1) each lie in one of them. To see this, let us set $\mathrm{d}x_k/\mathrm{d}t$ to zero, choose any constant value for u, and multiply Eq. (III.5.1) by $(1 + a - x_k)$. We end up with a third order polynomial in x_k, which has three real roots or fewer:

$$0 = 1 - (1 + ab)x_k - u[1 - x_k]x_k(1 + a - x_k) \tag{III.5.18}$$

$$= -u\,x_k^3 + (2u + au)\,x_k^2 - (1 + ab + u + au)\,x_k + 1 \tag{III.5.19}$$

This property allows us to investigate all local bifurcations of the full system looking only at three-cluster subspaces $C_{\{A_1,A_2,A_3\}}$ with different (n_1, n_2, n_3). An exemplary equilibrium curve is shown in Fig. III.5.5 for a three-cluster subspace $C_{\{A_1,A_2,A_3\}}$ with $n_1 = 0.8$, $n_2 = 0.16$, $n_3 = 0.04$. For every u and for fixed n_i, there are now up to $3^3 = 27$ equilibria, because each x_i can take one of three values while $\mathrm{d}x_i/\mathrm{d}t = 0$, $\mathrm{d}u/\mathrm{d}t = 0$, see Fig. III.5.5. Comparing Fig. III.5.5 to the two-cluster equilibria in Fig. III.5.2, we realize that these two-cluster equilibria are still there in the form of $C_{\{A_1,A_2\cup A_3\}}$.

III.5.4.1 Equivariant bifurcation of equilibria

Compared to the two-cluster subspace (Fig. III.5.2), in the three-cluster subspace (Fig. III.5.5), there are six more transcritical bifurcations (yellow dots), that is eight in total. In these transcritical bifurcations, the two-cluster equilibria interact with three-cluster equilibria, just like it is the case in Fig. III.5.2 between the fully synchronized equilibrium and the two-cluster equilibria. The transcritical bifurcations occur at the values of u at which the equilibrium equation (Eq. (III.5.19)) has a double

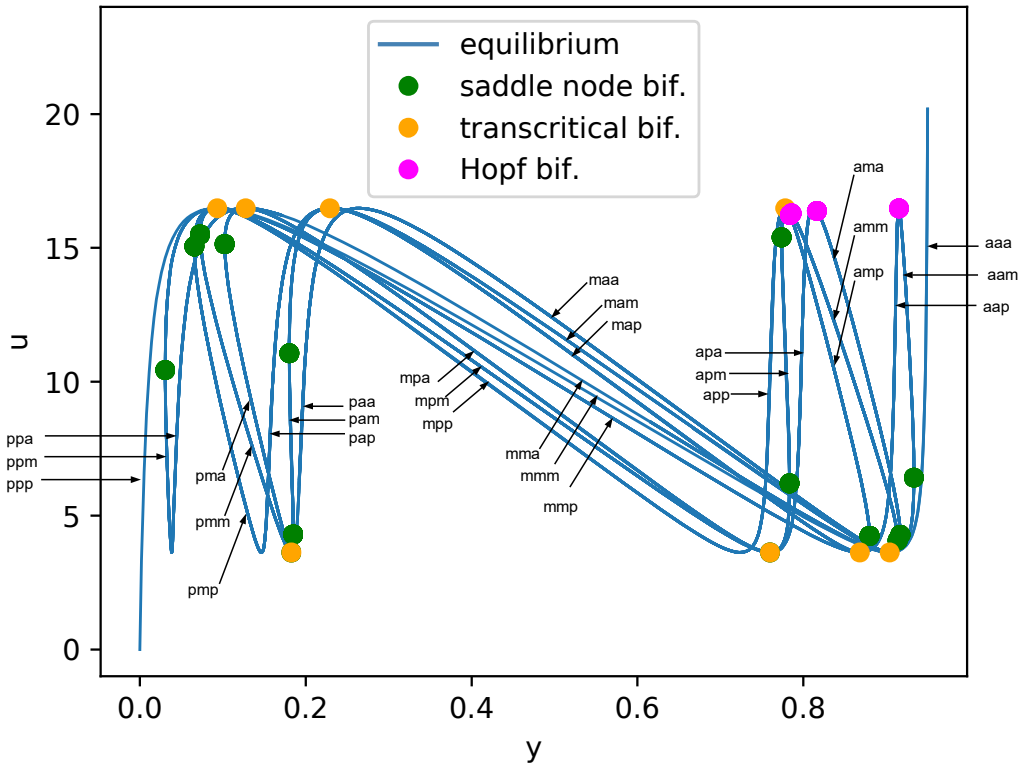

Figure III.5.5: Equilibrium curve in a three-cluster subspace on $C_{\{A_1,A_2,A_3\}}$ with $n_1 = 0.8$, $n_2 = 0.16$, $n_3 = 0.04$, for $a = 0.05$, $b = 0.01$. Like in Fig. III.5.1, the letters "a", "m", "p" indicate the active, middle, and passive equilibrium branch, respectively. The first of three letters represents x_1, the second x_2, the third x_3.

root, i.e. at the turning points of the fully synchronized equilibrium line. The bifurcation scenario of these additional transcritical bifurcations is similar to what we saw before, when a two-cluster equilibrium pierced the fully synchronized subspace. However, in this case a three-cluster equilibrium pierces a two-cluster subspace, because one extra cluster is present "as a bystander" during the bifurcation. Each of the three two-cluster subspaces that Eq. (III.5.17a) - (III.5.17d) can represent (i.e. $C_{\{A_1\cup A_2,A_3\}}$, $C_{\{A_1,A_2\cup A_3\}}$, $C_{\{A_1\cup A_3,A_2\}}$, i.e. $x_1 = x_2$, $x_2 = x_3$, $x_1 = x_3$) contains one such transcritical bifurcation for each double root of the equilibrium equation (III.5.19), of which there are two. So by $3 \cdot 2 = 6$, this gives us six more transcritical bifurcations in addition to the two we saw in Fig. III.5.2.

Unlike with the transcritical bifurcations that lie in the fully synchronized sub-

space (Fig. III.5.2), the positions of the other transcritical bifurcaions in two-cluster subspaces depend on the cluster sizes n_1, n_2, n_3. To investigate this, let u^* denote a value of u at which Eq. (III.5.19) has one real double root x_d and one real single root x_s. Without loss of generality, we consider $x_1 = x_\mathrm{s}$, $x_2 = x_3 = x_\mathrm{d}$, i.e. $C_{\{A_1, A_2 \cup A_3\}}$. Then, the associated value of y at which the bifurcation occurs is

$$\begin{aligned} y &= n_1 u^* g(x_1) + n_2 u^* g(x_2) + n_3 u^* g(x_3) && \text{(III.5.20)} \\ &= n_1 u^* g(x_\mathrm{s}) + (n_2 + n_3) u^* g(x_\mathrm{d}) && \text{(III.5.21)} \\ &= n_1 u^* g(x_\mathrm{s}) + (1 - n_1) u^* g(x_\mathrm{d}) && \text{(III.5.22)} \\ &= u^* [g(x_\mathrm{s}) - g(x_\mathrm{d})] n_1 + u^* g(x_\mathrm{d}), && \text{(III.5.23)} \end{aligned}$$

which is linear in n_1. Analogously, in the other two two-cluster subspaces (i.e. $C_{\{A_1 \cup A_3, A_2\}}$ and $(C_{\{A_1 \cup A_2, A_3\}})$, the value of y at which the transcritical bifurcation occurs depends linearly on n_2, n_3, respectively. Thus the transcritical bifurcations lie as shown in Fig. III.5.6. In this figure, we see that the eight transcritical bifurcations exist for every n_1. The value $n_1 = 0.8$ corresponds to Fig. III.5.5. We see the two transcritical bifurcations in $C_{\{A_1, A_2 \cup A_3\}}$ following Eq. (III.5.22). Furthermore, n_2 and n_3 are chosen to be linearly dependent on n_1 (see caption Fig. III.5.6), so the corresponding bifurcations lie on straight lines, too.

For the full system with N identical components this means that for each $\ell \in \{2, \ldots, N\}$ (i.e. combined size of cluster 2 and 3) there are $\binom{N}{\ell} \sum_{k=1}^{\ell-1} \binom{\ell}{k}$ transcritical bifurcations at $y = u^* [g(x_\mathrm{s}) - g(x_\mathrm{d})] \, \ell / N + u^* g(x_\mathrm{d})$. These bifurcations lie in $\binom{N}{\ell}$ different subspaces, depending on which x_k are at x_s and x_d. If you consider bifurcations as identical when they can be switched between by index perturbation, then there is only one such bifurcation for each combination of $\ell \in \{2, \ldots, N\}$ (i.e. combined size of cluster 2 and 3) and $k \in \{1, \ldots, \ell - 1\}$ (i.e. size of cluster 2). Furthermore, many of these transcritical bifurcations lie on the same points in parameter space and in phase space such that in total there are actually just $N - 1$ multi-branch bifurcation-points at every u^*, i.e. one for each possible size of cluster 1 (the cluster at x_s), i.e. one for each $\ell \in \{2, \ldots, N\}$. These bifurcations are invariant under intra-cluster index-permutations and are very similar to the equivariant bifurcations we saw in lower dimensions. Here, however, they can occur at various different values of y.

At certain parameters, the described transcritical bifurcations in three-cluster subspaces have another interesting property that we have similarly seen in two-cluster subspaces, like in Fig. III.5.3: The bifurcation point, which lies in a two-cluster subspace, participates in a homoclinic bifurcation with a limit cycle, which lies in a three cluster subspace and branches from a nearby Hopf bifurcation. This is again analog to what we have seen in the lower dimensional case.

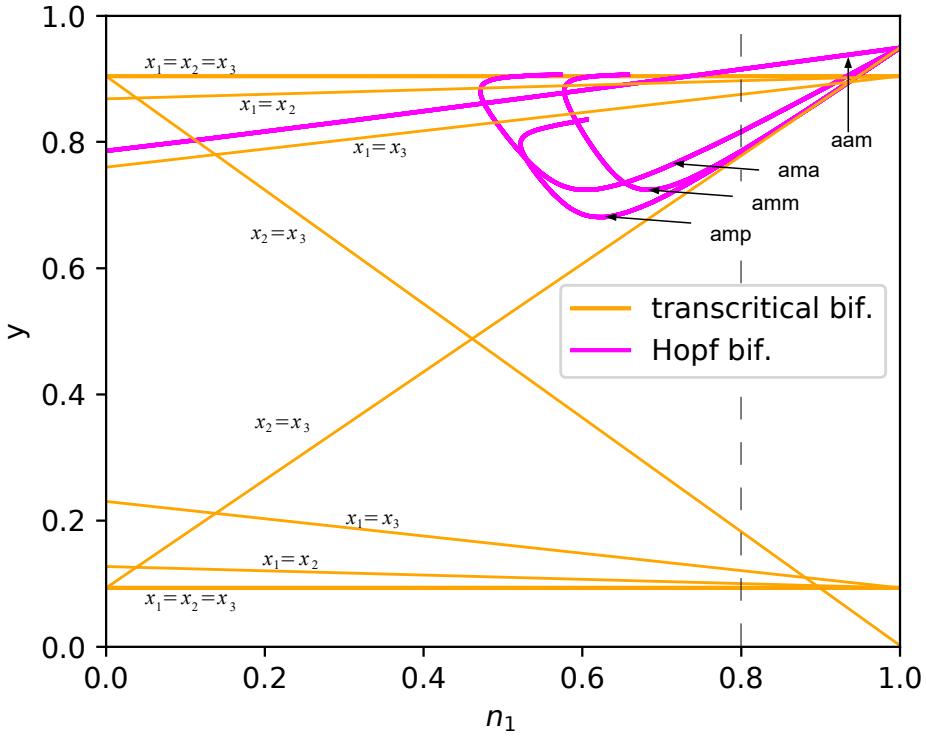

Figure III.5.6: Transcritical bifurcations (Eq. (III.5.22)) and some of the Hopf bifurcations (numerically continued with AUTO-07P [79]) occurring in three-cluster subspaces in which $n_2 = 0.8 \cdot (1 - n_1)$, $n_3 = 0.2 \cdot (1 - n_1)$, $a = 0.05$, $b = 0.01$. The letters "a", "m", "p" indicate the branches on which each of the three clusters sit during the plotted Hopf bifurcations (purple line), see Fig. III.5.1.

III.5.4.2 Equivariant bifurcation of limit cycles

Before, we saw equilibria in three-cluster subspaces that pierced invariant two-cluster subspaces in a transcritical bifurcation as y is varied. For the full system with N identical components this implied the presence of various equivariant bifurcations. Here, we present a similar scenario with limit cycles instead of equilibria. A limit cycle that lies in a three cluster subspace pierces an invariant two cluster subspace (wlog $x_2 = x_3$) in a transcritical bifurcation of limit cycles. This is illustrated in Fig. III.5.7 for $n_1 = 0.8$, $n_2 = 0.16$, $n_3 = 0.04$. At $y = 0.78625$ there is a three-cluster limit cycle and a three-cluster equilibrium, which became unstable in a three-cluster Hopf bifurcation at a slightly smaller y. There is also a two-cluster limit cycle and a two-cluster equilibrium, which branched from a two-cluster Hopf bifurcation at a slightly smaller y. These two-cluster limit sets lie in the invariant $C_{\{A_1,A_2\cup A_3\}}$ subspace, i.e $x_2 = x_3$. As y is increased to $y = 0.79$, we see that the limit cycles have increased in size and have moved closer together. At $y = 0.79625$ there is a transcritical bifurcation of the limit cycles, i.e. they fall together on $C_{\{A_1,A_2\cup A_3\}}$. Then, at $y = 0.8$, the three-cluster limit cycle is on the other side of the $C_{\{A_1,A_2\cup A_3\}}$ plane.

Because of continuity, the transcritical bifurcation of limit cycles has to exists for other values of n_2, n_3 (with $n_2 + n_3 = 1 - n_1$) as well, as long as we do not go too far away in (n_2,n_3) space. At the bifurcation, however, we have $x_2 = x_3$ for any choice of n_2, n_3 (with $n_2 + n_3 = 1 - n_1$), so the two-cluster limit cycle stays in place. For the full system with N identical components and large enough N this means that at this value of y multiple limit cycles from different three-cluster subspaces meet in the same two cluster limit cycle, each changing the sign of a different Lyapunov exponent of the two-cluster limit cycle. Remember that the Jacobian eigenvalues corresponding to directions transversal to a certain cluster subspace are degenerate (see linear analysis). This degeneracy is inherited by the Lyapunov of limit cycles that lie inside the cluster subspace. This means that at this values of y we have an equivariant bifurcation of limit cycles that changes the signs of all the Lyapunov exponents of the two cluster limit cycle simultaneously. However, it is not for sure, that in the three-cluster representation (Eq. III.5.17a - III.5.17d) the transcritical bifurcation of limit cycles persists for all n_2,n_3 (with $n_2 + n_3 = 1 - n_1$) or whether it turns into another mechanism of stabilizing the respective transversal (i.e. intra-cluster) Lyapunov exponents. Unfortunately, there is no straight forward method/tool to continue the transcritical bifurcation of limit cycles in parameter space. Developing such a method would be an interesting topic for further investigation.

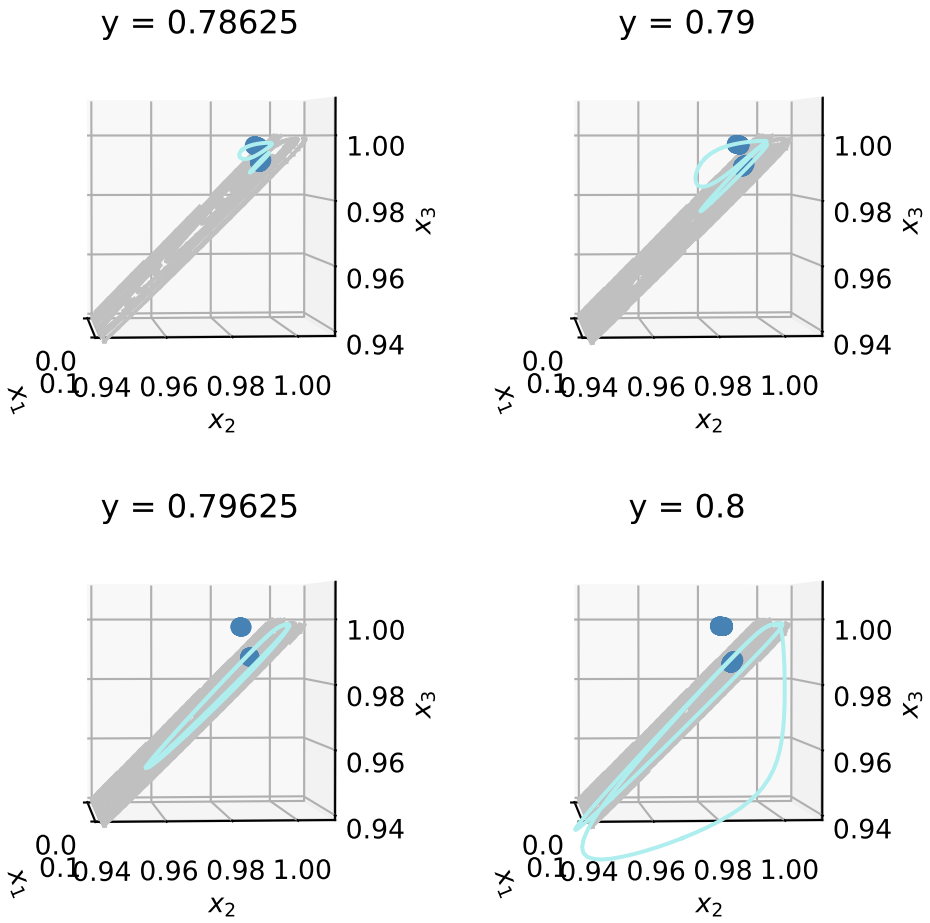

Figure III.5.7: Phase portraits showing a transcritical bifurcation of limit cycles (continued with AUTO-07P [79]) for $x_1 = 0.8$, $x_2 = 0.16$, $x_3 = 0.04$, $a = 0.05$, $b = 0.01$

Chapter III.6

Summary and Outlook

We have investigated the dynamics of an array (or ensemble) of parallelly connected Pt microelectrodes in a CO containing solution. This array can be seen as a model-system for the catalyzing Pt nanoparticles in hydrogen fuel cells and is therefore of technical interest. Besides that, we claimed that the Pt-CO system is also well suited for the general study of phase transitions in globally coupled systems of bistable components, because there is a well established mathematical model for it. To this end, we pointed out the analogy between a bistable open system like the array of Pt microelectrodes, and a common first order phase transition, like evaporation. We noticed that the main difference between the two lies in the coupling, which is local (e.g. diffusion) and global (e.g. common temperature) in the case of a common first order phase transition and solely global for the array of microelectrodes (common voltage). We then explained the observation that the microelectrodes switch on individually when the total current is ramped, and that the electric potential and the individual currents oscillate when the total current is fixed. For this, we did a linear stability analysis of the system. Since we made just very few assumptions on the exact dynamics, the results are applicable to a wide class of systems in which bistable components are globally coupled. We saw, for example, that the eigenvalues of the Jacobian with respect to intra-cluster perturbations are degenerate within each cluster. After the general linear analysis, we did a numerical nonlinear study of a concrete model of the Pt-CO system, which we derived by simplifying a well established Pt-CO model. We reduced the dynamics of the N electrode model to one, two, and three dimensional cluster subspaces and discussed the occurring local bifurcations. Among these local bifurcations we found Hopf bifurcations that induced oscillations, as observed in galvanostatic measurements. The oscillations that branched from Hopf bifurcations always had an unstable cluster or a cluster with just a single electrode in it, so we concluded that they would not be measurable in a real fuel cell with very large numbers of Pt nanoparticles. However, we also found a transcritical bifurcation of limit cycles that stabilized unstable clusters, yielding a stable limit-cycle oscillation with two clusters. We concluded that such a limit cycle would 'scale' up to large N, i.e. it would persist and remain stable if

the number of electrodes in the clusters and the total current are multiplied by any natural number.

There are several promising directions in which one could go from here. There is room for improvement of the linear analysis that we did. One could loosen the assumptions that we made for the individual components even further, e.g. by allowing multi-stability not only in u, but also in y. However, the most promising follow-up projects would rather build on the chapter about nonlinear cluster dynamics. It would be very interesting to find a way to numerically continue the transcritical bifurcation of limit cycles in the three-cluster subspace to other cluster sizes n_1, n_2, n_3 to get a more complete picture of the bifurcation scenario in the full N electrode system. There are also probably some homoclinic bifurcations in the system that one could look for. Even more interesting would be the question whether the transcritical bifurcation of limit cycles can also be found in the original, well established Pt-CO model. If so, it would be very likely that the corresponding 'scalable' oscillations (where all clusters have at least two electrodes in them) could also be measured with an array of microelectrodes. In this case, such oscillations would probably also occur in fuel cells. Apart from Pt catalysts for fuel cells, it would be interesting to look at other bistable systems. With the LC-circuit analogy that we presented, and with the associated necessary criterion, it is straight forward to filter for potential candidate systems by measuring their impedance along the equilibrium curve.

Part IV

Conclusion

We have considered two electrochemical systems, the electrodissolution of silicon in hydrofluoric acid and the electrooxidation of CO on platinum. Together, these two systems showcase the wide spectrum of modeling of complex systems. Both are of supreme technical relevance and both show complex selforganization.

Silicon is the main working material in integrated circuits and hydrofluoric acid can be used to clean, polish, and etch it, depending on the applied voltage and the pH value. Besides that, Si in HF acid is a prototypical example for a system that yields Chimera states, which have gained considerable attention in the non-linear dynamics community. Due to its technical relevance, Si in HF has been very much investigated, but still, the physical processes that lead to the complex selforganization are far from being clear. This mainly concerns the resonant voltage regime, in which Chimera states and other oscillatory phenomena can arise, depending on doping, illumination and external resistance. The most common approach here is to assume that the electrode consists of microscopic domains that are self-oscillating. The proposed oscillation mechanism differs between different models. Even though such models can explain some phenomena, they leave a lot of questions open, concerning quantitative explanations of the oscillation mechanisms and the embedding of the models into the well established frame of synchronization phenomena in a dynamical systems sense.

Besides the resonant regime, also the regime of negative differential resistance requires some modeling efforts. This is what we contributed in Part II. With a relatively simple model, we were able to reproduce the current-voltage curve, the impedance, the qualitative oxide layer thickness, and the dissolution valence. What we were not able to reproduce is the strange resonance that occurs as the resonant plateau begins. However, while for our explanations we separated the current-voltage curve into different voltage regimes, they are not really that clearly separated in reality. For example, we discussed that a limited illumination of n-type silicon might shear the current voltage curve such that the system becomes bistable between different states that would otherwise correspond to different voltage ranges. Our work forms the basis for further modeling and ultimately reproducing and explaining the Chimera states and other phenomena that this system exhibits. In this, the model will have to stay appropriately simple and consistent with all the measurements.

A powerful model for the Si-HF system would be able to reproduce the complex dynamical behavior, such that one could do a numerical bifurcation study. However, with regard to the lack of such a model, the problem should be tackled not only from the bottom, as we did here, but also from the top. This means modeling the dynamical features with purely mathematical model to determine the necessary ingredients. By this, one could reduce the search space for a physical model. Considerable progress in this regard has been made with the help of a modified version of the complex Ginzburg-Laundau equation, and there are still efforts worth taking in that direction. The gap between the top-down and the bottom-up approaches

will eventually have to be closed by taking a working bottom-up physical model with predictive power and showing that it fulfills the minimal requirements by the top-down considerations.

Apart from contributing to the understanding of the silicon system, the model that we presented also represents a new mechanism for the occurrence of a negative differential resistance in the current-voltage curve. Due to its simplicity, this mechanism is very likely to be also found in other electrochemical scenarios where there is a patina that is grown electrochemically and dissolved purely chemically.

In contrast to the silicon system, the electrooxidation of CO on platinum were already very well understood from a physicochemical point of view. The sequential activation and the oscillations could be well reproduced by established models. The remaining task here was to explain why these behaviors, mainly the oscillations, occur and how this generalizes to other systems of globally coupled bistable components. Unlike with the silicon the preexistence of a reliable model allowed for a throughout analytical study of the observed phenomena. We applied different degrees of abstraction. Firstly, we considered a general class of bistable systems under global coupling. With this, we explained the sequential activation in the dynamical-systems framework and derived a necessary condition for an oscillations to arise. For this criterion, we provided an intuitive LC-circuit analogy. Secondly, we considered a simplified version of a preexisting model. With this we illustrated the general analysis. Moreover, we performed a detailed bifurcation study on it and found an interesting limit cycle that would translate sustained oscillations for an arbitrarily large number of bistable components. Thus, it could for example be seen in real fuel cells with large numbers of catalyzing Pt nanoparticles. However, the implications might be even more far-reaching. Without the awareness that collective oscillations can be provoked in this way, the natural interpretation would be that observed oscillations emerge due to synchronization of individual oscillators. In view of our results, it might turn out that some observations of collective oscillations have to be reinterpreted. All in all, we recognize that even decades after its initiation, the field of non-equilibrium thermodynamics keeps baring new, fascinating findings.

Bibliography

[1] Alan Mathison Turing. »The chemical basis of morphogenesis«. In: *Bulletin of mathematical biology* 52.1-2 (1990), pp. 153–197. DOI: 10.1007/BF02459572.

[2] Munir M Salman et al. »Electro-oxidation of p-silicon in fluoride-containing electrolyte: A physical model for the regime of negative differential resistance«. In: *The European Physical Journal Special Topics* 227.18 (2019), pp. 2641–2658. DOI: 10.1140/epjst/e2019-800118-x.

[3] J-N Chazalviel. »Ionic processes through the interfacial oxide in the anodic dissolution of silicon«. In: *Electrochimica Acta* 37.5 (1992), pp. 865–875. DOI: 10.1016/0013-4686(92)85038-M.

[4] HJ Lewerenz and M Aggour. »On the origin of photocurrent oscillation at Si electrodes«. In: *Journal of Electroanalytical Chemistry* 351.1-2 (1993), pp. 159–168. DOI: 10.1016/0022-0728(93)80231-6.

[5] V Lehmann. »On the origin of electrochemical oscillations at silicon electrodes«. In: *Journal of The Electrochemical Society* 143.4 (1996), pp. 1313–1318. DOI: 10.1149/1.1836636.

[6] H Föll et al. »Self-organization phenomena at semiconductor electrodes«. In: *Electrochimica Acta* 55.2 (2009), pp. 327–339. DOI: 10.1016/j.electacta.2009.03.076.

[7] Konrad Schönleber and Katharina Krischer. »High-Amplitude versus Low-Amplitude Current Oscillations during the Anodic Oxidation of p-Type Silicon in Fluoride Containing Electrolytes«. In: *ChemPhysChem* 13.12 (2012), pp. 2989–2996. DOI: 10.1002/cphc.201200230.

[8] Iljana Miethe, Vladimir Garcia-Morales and Katharina Krischer. »Irregular subharmonic cluster patterns in an autonomous photoelectrochemical oscillator«. In: *Physical review letters* 102.19 (2009), p. 194101. DOI: 10.1103/PhysRevLett.102.194101.

[9] Iljana Miethe and Katharina Krischer. »Ellipsomicroscopic studies of the anodic oxidation of p-type silicon in fluoride containing electrolytes during current oscillations«. In: *Journal of Electroanalytical Chemistry* 666 (2012), pp. 1–10. DOI: 10.1016/j.jelechem.2011.11.027.

[10] Joris Proost et al. »On the origin of damped electrochemical oscillations at silicon anodes (revisited)«. In: *ChemPhysChem* 15.14 (2014), pp. 3116–3124. DOI: 10.1002/cphc.201402207.

[11] Xiaoge Gregory Zhang. *Electrochemistry of Silicon and its Oxide*. Springer, 2001. DOI: 10.1007/b100331.

[12] Daniel M Abrams and Steven H Strogatz. »Chimera states for coupled oscillators«. In: *Physical review letters* 93.17 (2004), p. 174102. DOI: 10.1103/PhysRevLett.93.174102.

[13] Lennart Schmidt et al. »Coexistence of synchrony and incoherence in oscillatory media under nonlinear global coupling«. In: *Chaos: An Interdisciplinary Journal of Nonlinear Science* 24.1 (2014), p. 013102. DOI: 10.1063/1.4858996.

[14] Konrad Schönleber et al. »Pattern formation during the oscillatory photoelectrodissolution of n-type silicon: turbulence, clusters and chimeras«. In: *New Journal of Physics* 16.6 (2014), p. 063024. DOI: 10.1088/1367-2630/16/6/063024.

[15] Lennart Schmidt and Katharina Krischer. »Chimeras in globally coupled oscillatory systems: From ensembles of oscillators to spatially continuous media«. In: *Chaos: An Interdisciplinary Journal of Nonlinear Science* 25.6 (2015), p. 064401. DOI: 10.1063/1.4921727.

[16] Konrad Schönleber, Maximilian Patzauer and Katharina Krischer. »A comparison of modeling frameworks for the oscillatory silicon electrodissolution«. In: *Electrochimica Acta* 210 (2016), pp. 346–351. DOI: 10.1016/j.electacta.2016.05.144.

[17] Carla Zensen et al. »A Capacitance Mediated Positive Differential Resistance Oscillator Model for Electrochemical Systems Involving a Surface Layer«. In: *The Journal of Physical Chemistry C* 118.42 (2014), pp. 24407–24414. DOI: 10.1021/jp505418x.

[18] J-N Chazalviel and F Ozanam. »A Theory for the Resonant Response of an Electrochemical System: Self-Oscillating Domains, Hidden Oscillation, and Synchronization Impedance«. In: *Journal of The Electrochemical Society* 139.9 (1992), pp. 2501–2508. DOI: 10.1149/1.2221253.

[19] A Uhlir. »Electrolytic shaping of germanium and silicon«. In: *Bell Labs Technical Journal* 35.2 (1956), pp. 333–347. DOI: 10.1002/j.1538-7305.1956.tb02385.x.

[20] K Osseo-Asare, Dawei Wei and Kamal K Mishra. »Dissolution windows for wet chemical processing of silicon and silicon dioxide: Potential-pH diagrams for the Si-F-H_2O system«. In: *Journal of The Electrochemical Society* 143.2 (1996), pp. 749–751. URL: http://citeseerx.ist.psu.edu/viewdoc/download?doi=10.1.1.946.4112&rep=rep1&type=pdf.

[21] J-N Chazalviel, M Etman and F Ozanam. »A voltammetric study of the anodic dissolution of p-Si in fluoride electrolytes«. In: *Journal of electroanalytical chemistry and interfacial electrochemistry* 297.2 (1991), pp. 533–540. DOI: 10.1016/0022-0728(91)80049-V.

[22] MJ Eddowes. »Anodic dissolution of p-and n-type silicon: Kinetic study of the chemical mechanism«. In: *Journal of electroanalytical chemistry and interfacial electrochemistry* 280.2 (1990), pp. 297–311. DOI: 10.1016/0022-0728(90)87005-5.

[23] DJ Blackwood et al. »Electrochemical and optical studies of silicon dissolution in ammonium fluoride solutions«. In: *Electrochimica acta* 37.5 (1992), pp. 889–896. DOI: 10.1016/0013-4686(92)85040-R.

[24] F Ozanam et al. »Resonant and nonresonant behavior of the anodic dissolution of silicon in fluoride media: An impedance study«. In: *Journal of The Electrochemical Society* 139.9 (1992), pp. 2491–2501. DOI: 10.1149/1.2221252.

[25] R Cheggou et al. »Theoretical modelling of the I–V characteristics of p-type silicon in fluoride electrolyte in the first electropolishing plateau«. In: *Electrochimica Acta* 54.11 (2009), pp. 3053–3058. DOI: 10.1016/j.electacta.2008.12.006.

[26] R Memming and G Schwandt. »Anodic dissolution of silicon in hydrofluoric acid solutions«. In: *Surface science* 4.2 (1966), pp. 109–124. DOI: 10.1016/0039-6028(66)90071-9.

[27] S Cattarin et al. »Electrodissolution of p-Si in Acidic Fluoride Media Modeling of the Steady State«. In: *Journal of the Electrochemical Society* 147.9 (2000), pp. 3277–3282. DOI: 10.1149/1.1393895.

[28] Volker Lehmann. *Electrochemistry of silicon*. Vol. 16. Wiley-VCH Verlag GmbH Weinheim, Germany, 2002. DOI: 10.1002/3527600272.

[29] *Engineering ToolBox (2017). Standard state and enthalpy of formation, Gibbs free energy of formation, entropy and heat capacity. [online]*. https://www.engineeringtoolbox.com/standard-state-enthalpy-formation-definition-value-Gibbs-free-energy-entropy-molar-heat-capacity-d_1978.html. Accessed: 2020-04-06.

[30] V Lehmann. »The Physics of Macropore Formation in Low Doped n-Type Silicon«. In: *Journal of the Electrochemical Society* 140.10 (1993), pp. 2836–2843. DOI: 10.1149/1.2220919.

[31] WD Mackintosh and HH Plattner. »The identification of the mobile ion during the anodic oxidation of silicon«. In: *Journal of The Electrochemical Society* 124.3 (1977), pp. 396–400. DOI: 10.1149/1.2133311.

[32] Hideki Hasegawa et al. »Anodic oxidation of hydrogenated amorphous silicon and properties of oxide«. In: *Journal of The Electrochemical Society* 135.2 (1988), pp. 424–431. DOI: 10.1149/1.2095631.

[33] Dennis R Turner. »Electropolishing silicon in hydrofluoric acid solutions«. In: *Journal of the electrochemical Society* 105.7 (1958), pp. 402–408. DOI: 10.1149/1.2428873.

[34] Anton Tosolini, Maximilian Patzauer and Katharina Krischer. »Bichaoticity induced by inherent birhythmicity during the oscillatory electrodissolution of silicon«. In: *Chaos: An Interdisciplinary Journal of Nonlinear Science* 29.4 (2019), p. 043127.

[35] Lennart Schmidt et al. »Unusual synchronization phenomena during electrodissolution of silicon: The role of nonlinear global coupling«. In: *Engineering of Chemical Complexity II* 12 (2014), p. 239. DOI: 10.1142/9789814616133_0014.

[36] M Seo et al. »Electroluminescence from p-type silicon during anodic oxidation in ethylene glycol solution«. In: *Journal of Electroanalytical Chemistry* 368.1 (1994), pp. 257–264. DOI: 10.1016/0022-0728(93)03105-X.

[37] Guixi Zhou, Yoichiro Nakanishi and Yoshinori Hatanaka. »Light emission effect in anodic oxidation of Si«. In: *Journal of The Electrochemical Society* 140.5 (1993), pp. 1468–1471. DOI: 10.1149/1.2221581.

[38] Andrzej Lasia. *Electrochemical impedance spectroscopy and its applications*. Vol. 7. Springer, 2014. DOI: 10.1007/0-306-46916-2_2.

[39] J. Guckenheimer and Y. A. Kuznetsov. »Bogdanov-Takens bifurcation«. In: *Scholarpedia* 2.1 (2007). revision #183057, p. 1854. DOI: 10.4249/scholarpedia.1854.

[40] J. Guckenheimer and Y. A. Kuznetsov. »Fold-Hopf bifurcation«. In: *Scholarpedia* 2.10 (2007). revision #91277, p. 1855. DOI: 10.4249/scholarpedia.1855.

[41] J Carstensen et al. »A model for current oscillations in the Si-HF system based on a quantitative analysis of current transients«. In: *Applied Physics A: Materials Science & Processing* 67.4 (1998), pp. 459–467. DOI: 10.1007/s003390050804.

[42] J Carstensen, R Prange and H Föll. »A Model for Current-Voltage Oscillations at the Silicon Electrode and Comparison with Experimental Results«. In: *Journal of the Electrochemical Society* 146.3 (1999), pp. 1134–1140. DOI: 10.1149/1.1391734.

[43] E Foca, J Carstensen and H Föll. »Modelling electrochemical current and potential oscillations at the Si electrode«. In: *Journal of Electroanalytical Chemistry* 603.2 (2007), pp. 175–202. DOI: 10.1016/j.jelechem.2007.01.019.

[44] J Grzanna, H Jungblut and HJ Lewerenz. »A model for electrochemical oscillations at the Si | electrolyte contact: Part I. Theoretical development«. In: *Journal of Electroanalytical Chemistry* 486.2 (2000), pp. 181–189. DOI: 10.1016/j.jelechem.2007.01.019.

[45] J Grzanna, H Jungblut and HJ Lewerenz. »A model for electrochemical oscillations at the Si | electrolyte contact: Part II. Simulations and experimental results«. In: *Journal of Electroanalytical Chemistry* 486.2 (2000), pp. 190–203. DOI: 10.1016/S0022-0728(00)00142-X.

[46] V Lehmann and H Föll. »Minority Carrier Diffusion Length Mapping in Silicon Wafers Using a Si-Electrolyte-Contact«. In: *Journal of The Electrochemical Society* 135.11 (1988), pp. 2831–2835. DOI: 10.1149/1.2095442.

[47] Vladimir Garcia-Morales and Katharina Krischer. »The complex Ginzburg–Landau equation: an introduction«. In: *Contemporary Physics* 53.2 (2012), pp. 79–95. DOI: 10.1080/00107514.2011.642554.

[48] V Lehmann and S Ronnebeck. »The Physics of Macropore Formation in Low-Doped p-Type Silicon«. In: *Journal of The Electrochemical Society* 146.8 (1999), pp. 2968–2975. DOI: 10.1149/1.2220919.

[49] J Erlebacher, K Sieradzki and PC Searson. »Computer simulations of pore growth in silicon«. In: *Journal of applied physics* 76.1 (1994), pp. 182–187. DOI: 10.1063/1.357125.

[50] Yen-Po Lin and Jenn-Gwo Hwu. »Suboxide characteristics in ultrathin oxides grown under novel oxidation processes«. In: *Journal of Vacuum Science & Technology A: Vacuum, Surfaces, and Films* 22.6 (2004), pp. 2265–2272. DOI: 10.1116/1.1795824.

[51] Simon M Sze and Kwok K Ng. *Physics of semiconductor devices*. John wiley & sons, 2006. ISBN: 978-0-470-06830-4.

[52] AB Comsol. »COMSOL Reference Manual (version 5.2 a)«. In: *Version Sept* (2016), pp. 1–1378.

[53] MATLAB. *version 9.3.0 (R2017b)*. Natick, Massachusetts: The MathWorks Inc., 2017. URL: https://www.mathworks.com/products/matlab.html.

[54] Dominique Koster et al. »Dynamic impedance spectroscopy using dynamic multi-frequency analysis: A theoretical and experimental investigation«. In: *Electrochimica Acta* 246 (2017), pp. 553–563. DOI: 10.1016/j.electacta.2017.06.060.

[55] Marcus Theodorus Maria Koper. *Far-from-equilibrium Phenomena in Electrochemical Systems: Instabilities, Oscillations and Chaos*. Universiteit Utrecht, Faculteit Scheikunde, 1994.

[56] Arkady Pikovsky et al. *Synchronization: A universal concept in nonlinear sciences*. Vol. 12. Cambridge University Press, 2003.

[57] Susanna C Manrubia, Alexander S Mikhailov et al. *Emergence of dynamical order: synchronization phenomena in complex systems*. World Scientific, 2004. DOI: 10.1142/9789812562463_0001.

[58] Joseph D Hart et al. »Experimental observation of chimera and cluster states in a minimal globally coupled network«. In: *Chaos: An Interdisciplinary Journal of Nonlinear Science* 26.9 (2016), p. 094801.

[59] Karen A Blaha et al. »Cluster Synchronization in Multilayer Networks: A Fully Analog Experiment with L C Oscillators with Physically Dissimilar Coupling«. In: *Physical review letters* 122.1 (2019), p. 014101.

[60] Hiroshi Kori et al. »Partial synchronization of relaxation oscillators with repulsive coupling in autocatalytic integrate-and-fire model and electrochemical experiments«. In: *Chaos: An Interdisciplinary Journal of Nonlinear Science* 28.4 (2018), p. 045111.

[61] D Golomb et al. »Clustering in globally coupled phase oscillators«. In: *Physical Review A* 45.6 (1992), p. 3516. DOI: 10.1103/PhysRevA.45.3516.

[62] Hamilton Varela et al. »A hierarchy of global coupling induced cluster patterns during the oscillatory H 2-electrooxidation reaction on a Pt ring-electrode«. In: *Physical Chemistry Chemical Physics* 7.12 (2005), pp. 2429–2439.

[63] Wen Wang, István Z Kiss and JL Hudson. »Experiments on arrays of globally coupled chaotic electrochemical oscillators: Synchronization and clustering«. In: *Chaos: An Interdisciplinary Journal of Nonlinear Science* 10.1 (2000), pp. 248–256.

[64] Nikos E Kouvaris et al. »Self-Organized Stationary Patterns in Networks of Bistable Chemical Reactions«. In: *Angewandte Chemie* 128.42 (2016), pp. 13461–13464.

[65] Ronald Imbihl and Gerhard Ertl. »Oscillatory kinetics in heterogeneous catalysis«. In: *Chemical Reviews* 95.3 (1995), pp. 697–733. DOI: 10.1021/cr00035a012.

[66] D Alfonso Crespo-Yapur et al. »Cooperative behaviour of Pt microelectrodes during CO bulk electrooxidation«. In: *ChemPhysChem* 14.6 (2013), pp. 1117–1121. DOI: 10.1002/cphc.201300105.

[67] D Alfonso Crespo-Yapur et al. »Sequential activation and oscillations of globally coupled microelectrodes during a bistable reaction«. In: *ChemElectroChem* 1.6 (2014), pp. 1046–1056. DOI: 10.1002/celc.201402029.

[68] Wolfgang Dreyer et al. »The thermodynamic origin of hysteresis in insertion batteries«. In: *Nature materials* 9.5 (2010), p. 448. DOI: 10.1038/nmat2730.

[69] Wolfgang Dreyer, Clemens Guhlke and Robert Huth. »The behavior of a many-particle electrode in a lithium-ion battery«. In: *Physica D: Nonlinear Phenomena* 240.12 (2011), pp. 1008–1019. DOI: 10.1016/j.physd.2011.02.011.

[70] Bernardo Orvananos et al. »Particle-level modeling of the charge-discharge behavior of nanoparticulate phase-separating Li-ion battery electrodes«. In: *Journal of The Electrochemical Society* 161.4 (2014), A535–A546. DOI: 10.1149/2.024404jes.

[71] Yang Sun et al. »Electrochemical oscillation in li-ion batteries«. In: *Joule* 2.7 (2018), pp. 1265–1277.

[72] W Dreyer, I Müller and P Strehlow. »A study of equilibria of interconnected balloons«. In: *The Quarterly Journal of Mechanics and Applied Mathematics* 35.3 (1982), pp. 419–440. DOI: 10.1093/qjmam/35.3.419.

[73] Wolfgang Dreyer, Clemens Guhlke and Michael Herrmann. »Hysteresis and phase transition in many-particle storage systems«. In: *Continuum Mechanics and Thermodynamics* 23.3 (2011), pp. 211–231. DOI: 10.1007/s00161-010-0178-1.

[74] S Bozdech et al. »Oscillations in an array of bistable microelectrodes coupled through a globally conserved quantity«. In: *Chaos: An Interdisciplinary Journal of Nonlinear Science* 28.4 (2018), p. 045113. DOI: 10.1063/1.5022475.

[75] Todd R Ferguson and Martin Z Bazant. »Nonequilibrium thermodynamics of porous electrodes«. In: *Journal of The Electrochemical Society* 159.12 (2012), A1967–A1985. DOI: 10.1149/2.048212jes.

[76] Samuel M Allen and John W Cahn. »A microscopic theory for antiphase boundary motion and its application to antiphase domain coarsening«. In: *Acta metallurgica* 27.6 (1979), pp. 1085–1095. DOI: 10.1016/0001-6160(79)90196-2.

[77] Y. A. Kuznetsov. »Saddle-node bifurcation«. In: *Scholarpedia* 1.10 (2006). revision #151865, p. 1859. DOI: 10.4249/scholarpedia.1859.

[78] Y. A. Kuznetsov. »Andronov-Hopf bifurcation«. In: *Scholarpedia* 1.10 (2006). revision #90964, p. 1858. DOI: 10.4249/scholarpedia.1858.

[79] Eusebius J Doedel et al. »AUTO-07P: Continuation and bifurcation software for ordinary differential equations«. In: (2007).